FERROELECTRIC PVDF-BASED POLYMER THIN FILMS AND NANOSTRUCTURES

LI XUE

(B. Eng.) Tsinghua University

A THESIS SUBMITTED

FOR THE DEGREE OF DOCTOR OF PHILOSOPHY

DEPARTMENT OF MECHANICAL ENGINEERING

NATIONAL UNIVERSITY OF SINGAPORE

2012

DECLARATION

I hereby declare that this thesis is my original work and it has been written by me in its entirety. I have duly acknowledged all the sources of information which have been used in the thesis.

This thesis has also not been submitted for any degree in any university previously.

Li Xue
_____

Li Xue

25 September 2012

Acknowledgements

TABLE OF CONTENTS

Summary

The ferroelectric poly(vinylidene fluoride) (PVDF)-based materials are one of the most technically important and extensively studied ferroelectric polymers because of their relatively high remnant polarization, large piezoelectric coefficient, high dielectric constant, and low dielectric loss, making them promising dielectrics for wide device applications including acoustic transducers, piezoelectric sensors, high energy density dielectric capacitors, and electromechanical transducers. Extensive attention has been paid on PVDF-based polymer thin films and nanostructures, such as nanotubes and nanowires, due to their unique properties and potential applications as functional elements in micro- and nano-electromechanical systems. In this work, ferroelectric PVDF-based low-dimensional structures, namely thin films and nanotubes, are investigated. By using modified chemical solution deposition approach and anodic aluminum oxide membrane (AAM) as template, we are able to fabricate ferroelectric polymer thin films and nanostructures with low-cost, scalable and convenient methods.

The PVDF copolymer poly(vinylidene fluoride co trifluoroethylene) (P(VDF-TrFE)) has been widely studied for its convenience to achieve the desirable polar β phase directly from melt or solution. We have designed and fabricated P(VDF-TrFE) nanotube array in AAM template and studied its potential applications for high energy density capacitor. Electroless-plated Ag layers were deposited on both inner and outer sides of the P(VDF-TrFE) nanotubes as electrodes, which greatly enlarged

the contact area between the electrodes and the polymer dielectric. The nanotubes are sealed at one end, which prevents shorting between the two electrodes. According to theoretical calculation, the layer of nanotube array with a layer thickness of 2 μm and a wall thickness of about 50 nm has 33 times larger surface area and 763 times larger capacitance when compared to a P(VDF-TrFE) film with a similar film thickness. Experimentally, a 95 times larger capacitance was demonstrated.

The P(VDF-TrFE) nanotube array is also studied for its potential application in energy harvesting. Theoretical simulations indicate that under constant force condition, the flexible piezoelectric polymer nanotube structure is superior to the nanorod in terms of electrical energy generation by harvesting mechanical energy. For the first time, piezoelectric current has been experimentally demonstrated in P(VDF-TrFE) nanotube array, with a conductive AFM (C-AFM) tip to provide periodic mechanical deformation and also to measure the generated current. The current generation in the polymer nanotubes is correlated to the existence of polar phase in the polymer and the electrical poling conditions, which shows that polarization and piezoeletric effect play the dominant roles. The theoretical analyses and experimental demonstration show that the flexible ferroelectric polymer nanotube array is a very promising candidate for mechanical energy harvesting applications.

Compared to P(VDF-TrFE), PVDF homopolymer possesses many advantages, such as higher intrinsic polarization, higher Curie temperature, higher breakdown strength and significantly lower cost. However, it is always challenging to obtain the highly polar β phase in PVDF homopolymer. In this study, β phase PVDF thin films and nanotube array have been fabricated using various approaches, such as incorporation of hydrated salt, Langmuir-Blodgett (LB) deposition and solution deposition in AAM template. The mechanism of β phase formation in PVDF homopolymer has been studied.

In the first approach to achieve ferroelectric β phase in PVDF thin films, hydrated salts are introduced in PVDF precursor solution before spin-coating process. The retaining and loss of water in PVDF film introduced by hydrated salts are manipulated to promote formation of β phase crystals, and the resulting films show electrical properties comparable to those of P(VDF-TrFE). It is found that the hydrogen bonds between PVDF molecules and water in the hydrated salts promote the crystallization of β phase. This mechanism is further studied in PVDF ultrathin LB film. Hydrogen bonds formed between PVDF molecules and water in LB deposition lead to the direct formation of ferroelectric β phase. The PVDF molecular chains are aligned parallel to the substrates and the dipoles are perpendicular to the substrates.

Furthermore, PVDF homopolymer nanotube array with the desired ferroelectric

β-phase are fabricated by depositing pure PVDF solution on AAM surface. A significantly improved effective piezoelectric coefficient d_{33} of -19.2 pm/V is obtained, over the thin film counterpart with solid substrate. Theoretical analysis indicates that the hydrogen bonds between hydroxyl groups at AAM surface and PVDF molecules at the interface promote the formation of the all-trans β phase.

List of Figures

List of Tables

List of Abbreviations

AAM   Anodic alumina membrane

C-AFM   Conductive atomic force microscopy

DMF   Dimethylformamide

FTIR   Fourier Transform Infrared Analysis

LB   Langmuir-Blodgett

LSV   Laser scanning vibrometer

PFM   Piezoresponse force microscopy

PMN-PT   Lead magnesium niobate-lead titanate

PVDF   Poly(vinylidene fluoride)

P(VDF/TrFE)   Poly(vinylidene fluoride/trifluoroethylene)

PZT   Lead zirconate titanate

SEM   Scanning electron microscopy

TEM   Transmission electron microscopy

TGA   Thermogravimetric Analysis

TGTG'   Trans-Gauche-Trans-Gauche'

XRD   X-ray diffraction

Chapter 1   Introduction

1.1 Ferroelectric materials

1.1.1 Piezoelectricity and ferroelectricity

The crystal structural symmetry determines some physical properties of crystals, such as dielectric, piezoelectric, pyroelectric, ferroelectric, and nonlinear optical properties [1]. The structure of crystals can be divided into 32 crystallographic point groups according to the number of rotational axes and reflection planes they possess. Among the 32 crystallographic point groups, 11 groups possess a center of symmetry and 21 groups do not. Twenty of the twenty-one non-centro-symmetric groups have piezoelectricity, which is the ability of certain crystalline materials to generate a voltage in response to applied mechanical stress. Piezoelectric materials also display the converse effect: mechanical deformation upon application of electrical charge or signal. This convertible behavior was first discovered by Pierre and Jacques Curie in 1880 in certain crystals, such as quartz, zinc blends, tourmaline, and Rochelle salt [2, 3]. Ten of these twenty groups have a unique polar axis and possess spontaneous polarization. All the polar crystals have pyroelectricity, which means that the polarization can be changed by temperature.

Ferroelectricity is a property of certain dielectrics, which exhibit a spontaneous electric polarization that can be reversed in direction by the application of an appropriate electric field. This is due to the separation of the center of positive and

negative electric charge, making one side of the crystal positive and the opposite side negative. Furthermore, the polarization can be reversed in direction by the application of an appropriate electric field [4]. The term ferroelectrics arose by analogy with ferromagnetics, mainly because they have similar characteristics: under electric fields for ferroelectric phenomena and under magnetic fields for ferromagnetic phenomena.
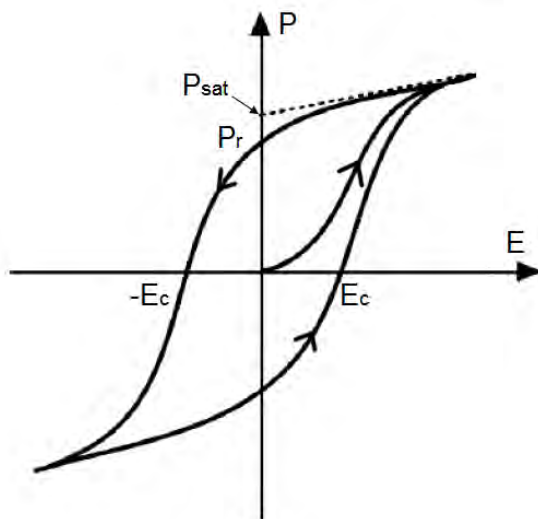
Figure 1.1   A polarization - electric field ferroelectric hysteresis loop.

Figure 1.1 shows a typical polarization - electric field P(E) hysteresis loop of ferroelectric materials [5]. As the applied electric field increases, the increasing polarization indicates that ferroelectric domains are oriented and switched along the applied field. Once all the domains are aligned, the ferroelectric material possesses saturated polarization (P_{sat}). When the applied field is decreased until zero point, some of the domains still remain oriented. The polarization at zero external field is called remnant polarization (P_r). To reach the zero polarization state, reversed

electric field must be applied. The field necessary to bring the polarization to zero is called the coercive field (E_C).

1.1.2 Ferroelectric ceramics and polymers

A wide variety of materials exhibit piezoelectricity and ferroelectricity, including poled polycrystalline ceramics (e.g. lead zirconate titanate, PZT), single-crystal or highly oriented polycrystalline ceramics (e.g. quartz), organic crystals (e.g. ammonium dihydrogen phosphate), and polymers (e.g. poly(vinylidene fluoride), PVDF).

Ferroelectric ceramics, particularly those with the pervoskite structure, are known to have very high piezoelectric constants because of their strong polarization. Perovskite is the name of the mineral calcium titanate ($CaTiO_3$). The general compound in pervoskite-structure family is expressed by the formula ABO_3, where O is oxygen, A represents a cation with a larger ionic radius, and B a cation with a smaller ionic radius [6].
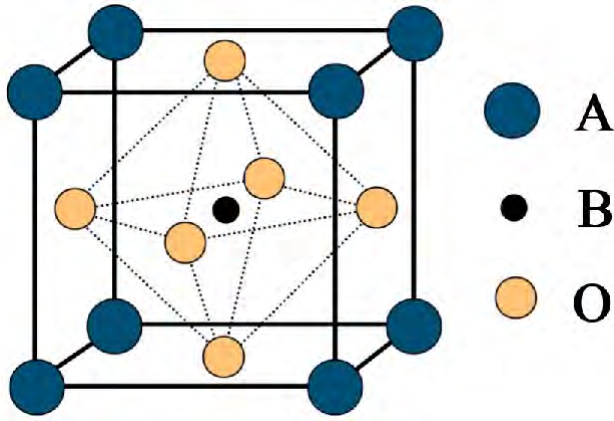
Figure 1.2 Crystal structure for the ABO$_3$ pervoskite.

Figure 1.2 presents the typical crystal structure of ABO$_3$. Above the Curie temperature (T_c) these materials have a centrosymmetric structure and hence do not exhibit any spontaneous polarization, known as paraelectric phase. As the temperature is lowered below the Curie point, phase transformation takes place from paraelectric state to ferroelectric state. The center ion is displaced from its body center position and the cubic unit cell deforms to non-centro-symmetric structure. Many piezoelectric ceramics such as Barium Titanate (BaTiO$_3$), Lead Titanate (PbTiO$_3$), Lead Zirconate Titanate (PZT) and others have the perovskite structure [7-9].

The lead zirconate titanate (PbZr$_{1-x}$Ti$_x$O$_3$, PZT) ferroelectric ceramics have received the most widespread studies and application because of its excellent piezoelectric and dielectric properties [9-11]. The piezoelectric response of PZT is intimately linked to its crystal structure, and best performance is achieved in compositions close to a phase boundary [12]. However, the major disadvantage of the above systems is the volatility of the lead constituents of these materials, which complicates their introduction into

semiconductor fabrication facilities. In addition, there are also environmental issues associated with the toxicity of the lead. Lead-free piezoelectric materials are still being developed, including barium titanate ($BaTiO_3$) (BT) [13, 14], sodium bismuth titanate ($Na_{0.5}Bi_{0.5}TiO_3$) (NBT) [15-17], potassium bismuth titanate ($K_{0.5}Bi_{0.5}TiO_3$) (KBT) [18], sodium potassium niobate ($Na_{0.5}K_{0.5}NbO_3$) (KNN) [19-21] and bismuth ferrite ($BiFeO_3$) (BFO) [22, 23].

Some of the lead-free ceramics show properties comparable to PZT. However, there is no single system that can replace PZT in all application fields. Barium titanate (BT) is one of the most important and well studied lead-free ferroelectric materials. However, its application has shifted away from transducers to an almost exclusive use as high-dielectric constant capacitors. The relatively low Curie temperature (120 ^{o}C) and low electromechanical coupling factor in comparison to PZT (0.35 vs. 0.65) limit its application [9].

Piezoelectricity and ferroelectricity can also been documented in a number of polymers [24]. In the last few decades, polymeric ferroelectrics have received increasing interest as functional materials in various applications. Early in the 1950s, weak shear piezoelectricity was observed by Fukada in some kinds of biopolymers such as wood [25], bone [26] and silk fibers [27]. In 1969, piezoelectric effect of stretched poly (vinylidene fluoride) (PVDF), based on the monomer CH_2-CF_2, was discovered by Kawai H [28]. The structure and properties of PVDF-based polymers

have received extensive studies because of the strong piezoelectric and ferroelectric

effects. It was found that the copolymer of vinylidene fluoride (VDF) and

trifluoroethylene (TrFE) P(VDF-TrFE) directly crystallized to polar β phase without

stretching, which greatly enlarges the range of its applications. Besides the PVDF

family, piezoelectricity and ferroelectricity have also been discovered in a number of

polymers, including odd-numbered nylons [29], poly-L-lactic acid (PLLA) [30],

polyureas [31] and poly (vinyldenecyanide and vinylacetate) [P(VDCM/VAc)] [30].

Among the various ferroelectric polymers, PVDF-based polymer is still the most

popular one in applications because of its unique polarization and piezoelectric

coefficients. Table 1 shows the properties of some piezoelectric materials.

Table 1.1 Properties of some piezoelectric materials.

Material	Piezoelectric constant (pm/V or pC/N)	Reference
Quartz	d_{11}= -2.3	[32]
Lead Zirconate Titanate (PZT)	d_{33}= -189	[9]
Barium Titanate	d_{33}= -190	[14]
Poly(vinylidene fluoride) (PVDF)	d_{33}= -31	[18]
Polyamide (Nylon 11)	d_{31}= 3	[29]
Polyurea	d_{33}= 3.4	[31]

Ferroelectric polymers exhibit properties almost complementary to those of

pervoskite-type oxides, although the largest piezoelectric coefficients of 30~40 pC/N

achieved in uniaxially stretched PVDF are moderate in comparison to piezoelectric

ceramics. The low permittivity of the polymers leads to high values of the

piezoelectric voltage constants ($d/\varepsilon_r\varepsilon_0$). The acoustic impedances of the polymers

are much lower than those of ceramic materials and much closer to those of water and

biological tissue, which commonly removes the need for matching layers.

Furthermore, the polymers can be prepared in very thin, large area sheets and are relatively inexpensive. In addition to being respectable piezoelectrics, they are light, flexible and nontoxic, which is particularly important in the view of the recent interest in new, more efficient, and environmentally friendly materials.

1.2 PVDF and its copolymers

1.2.1 PVDF homopolymer

Poly (vinylidene fluoride) (PVDF) is a semi-crystalline polymer consists of a repeated monomer unit of $-CH_2-CF_2-$. The polymer has been used in many applications since it is very durable, with high mechanical and high impact strength. The atoms are covalently bonded, forming long molecular chains. PVDF is inherently polar because the hydrogen atoms are positively charged and the fluorine atoms are negatively charged with respect to the carbon atoms. However, the net polar moment of the material in its original state is zero due to the random orientation of the individual crystallites. PVDF and its copolymers have attracted much attention for their efficient piezoelectric, ferroelectric and pyroelectric properties [33-35].

1.2.1.1 Crystal structure of PVDF

PVDF has at least four crystalline phases, designated as α, β, γ and δ. The different phases are distinguished by the conformation of the C-C bonds along the chain backbone. β-phase PVDF exhibits the most superior ferroelectric and piezoelectric

properties due to its all-trans planar zigzag structure. Transformations between the phases can be achieved in various conditions.

α phase

When PVDF melt is cooled to room temperature at a normal rate, it forms the non-polar α phase, which is the thermodynamically most stable structure of PVDF. The molecules are in a distorted trans-gauche-trans-gauche' (TGTG') conformation, which is distorted by the steric hindrance between the fluorine atoms. There is a large dipole moment associated with the carbon-fluorine bond which results in a net dipole moment perpendicular to the chain axis. However, the dipole moments of neighboring chains are anti-parallel, thus cancel each other. Therefore the α–phase PVDF is non-polar and does not show ferroelectric and piezoelectric response. The structure and packed chains are shown in Figure 1.3.
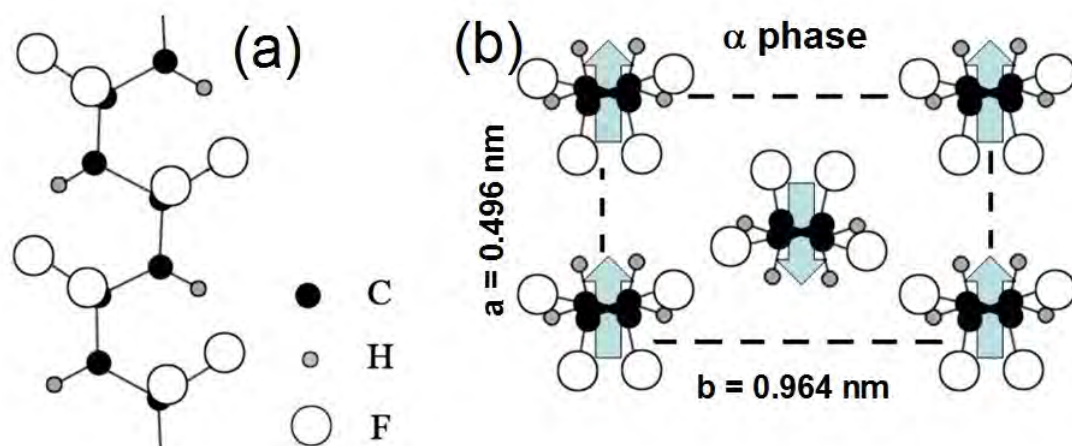
Figure 1.3 Conformation and crystal structure of PVDF α phase: (a) side view of a molecular chain in TGTG' conformation, (b) end view of α phase crystal structure.

β phase

As shown in Figure 4, the polar β-phase PVDF exhibits the most superior ferroelectric and piezoelectric properties. The polymer chains in this phase are in a distorted, planar zigzag, all-trans conformation, which results in a polar unit cell with a large dipole moment. The chains are highly oriented with the –CF$_2$- dipoles pointing along the b-axis, while perpendicular to the chain axis. The planar zigzag conformation is distorted because the fluorine atoms are too large to allow simple all-trans conformation. The polar β-phase has attracted technological interest because of its superior piezoelectric properties.
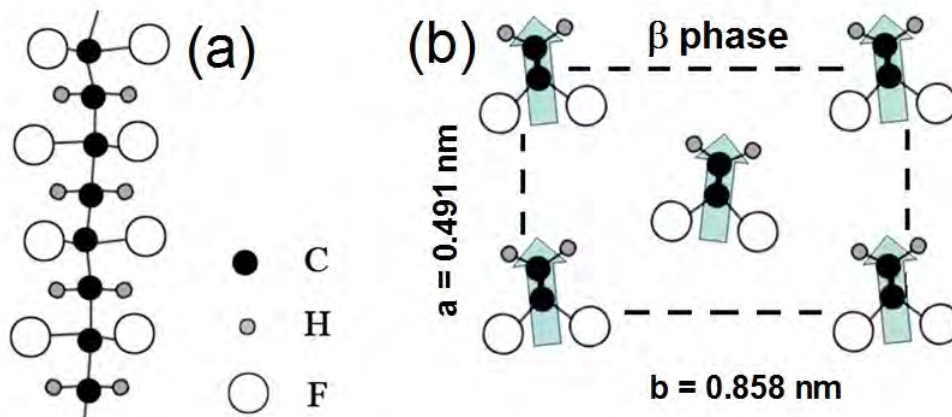
Figure 1.4 Conformation and crystal structure of PVDF β phase: (a) side view of a molecular chain in all-trans conformation, (b) end view of β phase crystal structure.

γ phase and δ phase

In γ-phase crystals, the chain conformations are represented as TTTGTTTG'. The γ-phase crystal has a monoclinic crystal lattice. Both γ phase and δ phase exhibit relatively small net dipole moment compared to β phase. Due to their weak

polarization, there have been only limited research interests in PVDF γ and δ phase

on electrical applications.

1.2.1.2 Phase transformations of PVDF
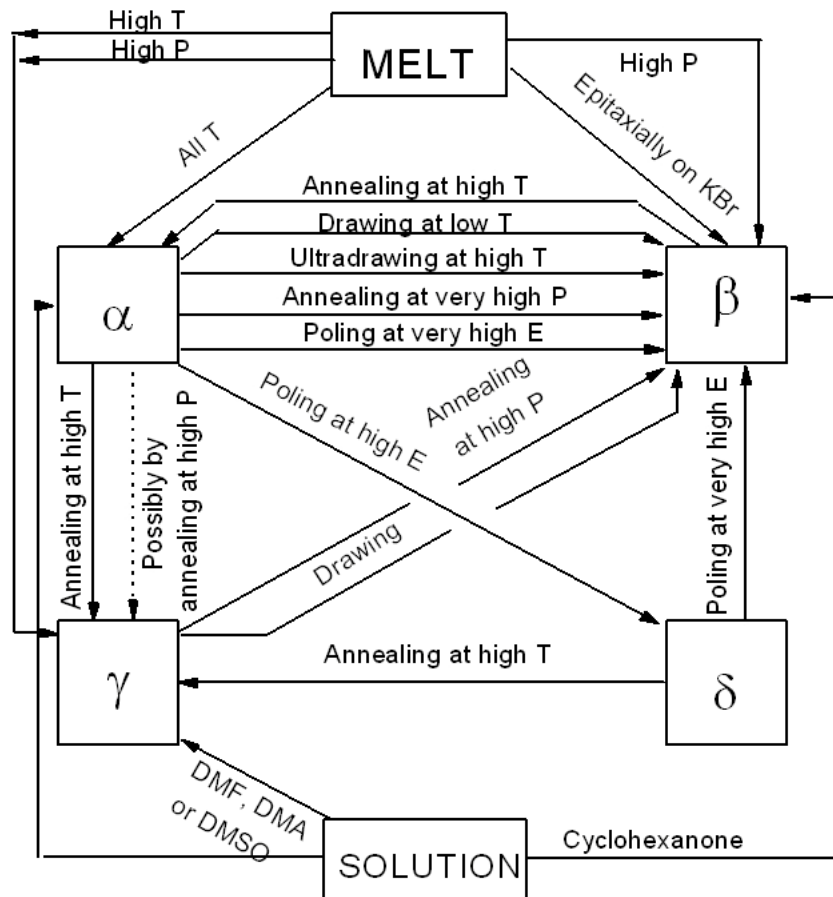
Figure 1.5 Phase transformation between the phase transformations of different crystalline phases of PVDF [36].

Figure 1.5 summaries the phase transitions of different PVDF crystalline phases. The

phases and transformations between the phases can be produced by a variety of means,

such as mechanical stretching, high temperature annealing or application of electric

fields [36].

The polar β phase can be achieved by cooling PVDF melt in extremely rapid quench, while a moderate cooling rate results in non-polar α phase. Stretching α-phase bulk film at a stretch ratio of about 3-5 can induce the formation of β phase. In the stretching process, the lamellae are oriented perpendicular to the draw direction so that the molecules are parallel to the draw direction. Hence β-phase structure is induced. The γ phase forms upon high temperature crystallization or high temperature annealing of α-phase. Crystal defects or the presence of polymeric surfactants can also induce the formation of γ phase. Transition from α phase to δ phase occurs at high electric field (120 MV/m) treatment, and δ phase film can be converted further to β phase at higher field (500 MV/m) [37-40].

The β-phase PVDF has the best ferroelectric and piezoelectric performance among the different crystalline structures. Hence the method to obtain β-phase PVDF is always of great importance for high performance piezoelectric device applications.

As mentioned above, the β-phase film can be obtained through mechanically stretching the α–phase bulk film in a certain temperature range. Furthermore, the β-phase film can also be induced by high-field room-temperature poling of the α-phase thin films [41], melt crystallization at high pressure [42], blending with carbon nanotubes [43] or organically modified nanoclay [44, 45]. The solution cast PVDF thin films tend to crystallize in α phase in solvents with lower dipole moment or γ phase in solvents with a higher dipole moment. And the thin films cannot be

modified using the mechanical stretching method. Hence there are few papers describing methods to produce solution cast PVDF films in β phase. It is reported that PVDF films with un-oriented β phase crystallinity have been derived from polar HMPA (hexamethylphosphoramide) solutions [46]. In recent years, M. Benz first reported that β phase could be promoted in PVDF with the presence of water introduced by hygroscopic/hydrated chemicals in the precursor solutions [47], but the obtained PVDF samples were also very porous without showing any useful ferroelectric or piezoelectric properties. In the previous studies, dense β-phase dominant PVDF films on silicon substrate were obtained by introducing magnesium nitrate hexahydrate $(Mg(NO_3)_2 \cdot 6H_2O)$ in the PVDF precursor solution and demonstrated useful ferroelectric and piezoelectric properties [48,49]. These β phase promoting methods in solution cast PVDF films will be further discussed in Chapter 5.

1.2.2 PVDF blends and copolymers

After the discovery of piezoelectricity in PVDF homopolymer, researchers have tried to produce materials with higher performance for practical applications by changing the chemical and physical structure of the polymer. It has been reported that PVDF can be blended with a number of polymers that exhibit a strong molecular electrical moment. Table 2 presents the repeat unit of several polymers that are miscible with PVDF, including poly(methyl methacrylate)   (PMMA), poly(ethyl methacrylate) (PEMA), poly(methyl acrylate) (PMA), poly(ethyl acrylate) (PEA),   poly(vinyl

methyl ketone) (PVMK), poly(tetramethylene adipate) (PTMA) and polyvinyl

acetate (PVAc). All of the polymers have carbonyl group. Hydrogen bond is formed

between the double-bounded oxygen in the carbon group and the hydrogen in PVDF

polymer chain.

Table 1.2   Polymers which are miscible with PVDF

Polymer	Abbreviation	Repeat unit
Poly(methyl methacrylate)	PMMA	$\begin{array}{c} CH_3 \\ | \\ +CH_2-C\}_x \\ | \\ O=C-O-CH_3 \end{array}$
Poly(ethyl methacrylate)	PEMA	$\begin{array}{c} CH_3 \\ | \\ +CH_2-C\}_x \\ | \\ O=C-O-CH_2CH_3 \end{array}$
Poly(methyl acrylate)	PMA	$\begin{array}{c} +CH_2-CH\}_x \\ | \\ O=C-O-CH_3 \end{array}$
Poly(ethyl acrylate)	PEA	$\begin{array}{c} +CH_2-CH\}_x \\ | \\ O=C-O-CH_2CH_3 \end{array}$
Poly(vinyl methyl ketone)	PVMK	$\begin{array}{c} +CH_2-CH\}_x \\ | \\ O=C-CH_3 \end{array}$
Poly(tetramethylene adipate)	PTMA	$+O-(CH_2)_4-O-\overset{O}{\overset{\|}{C}}-(CH_2)_4-\overset{O}{\overset{\|}{C}}\}_x$
Polyvinyl acetate	PVAc	$\begin{array}{c} +CH_2-CH\}_x \\ | \\ O=C-O-CH_3 \end{array}$

The physical properties of PVDF, such as Curie temperature, elastic modulus, degree

of crystallinity and electrical properties can also be significantly improved by introducing an appropriate co-monomer into polymer chain during the copolymerization process. The structures of several commonly used monomer units that have been introduced into PVDF polymer chain are shown in Table 1.3, resulting in PVDF copolymers as well as trepolymers including:

poly(vinylidene fluoride/trifluoroethylene) (P(VDF/TrFE)),

poly(vinylidene fluoride-hexafluoropropylene) (P(VDF/HFP)),

poly(vinylidene fluoride/chlorofluoroethylene) (P(VDF/CFE))

poly(vinylidene fluoride/ chlorotrifluoroethylene) (P(VDF/CTFE)),
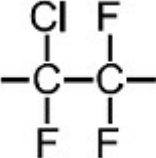
poly(vinylidene fluoride/trifluoroethylene/ chlorofluoroethylene) (P(VDF/TrFE/CFE)),

and poly(vinylidene fluoride/trifluoroethylene/chlorotrifluoroethylene)

(P(VDF/TrFE/CTFE)).

Table 1.3   Commonly used Monomer units in PVDF copolymers

Polymer	Abbreviation	Repeat unit
Trifluoroethylene	TrFE	
Hexafluoropropylene	HFP	
Chlorofluoroethylene	CFE	

Chlorotrifluoroethylene	CTFE	$\begin{array}{cc} Cl & F \\ | & | \\ -C-C- \\ | & | \\ F & F \end{array}$

P(VDF-TrFE) is one of the most commonly-used copolymers, which is usually available in ratios of about 50:50 wt% and 65:35 wt% (equivalent to about 56:44 mol% and 70:30 mol%).

Copolymerization of TrFE with VDF introduces more fluorine atoms into the polymer chain to produce steric and electrostatic hindrance and prevent the molecular chains from forming conformation of α phase (TGTG'). Hence β phase becomes the most thermodynamically preferred in the copolymer. The ferroelectric β phase can be directly achieved in P(VDF-TrFE) from melt or solution without additional treatment, such as mechanical stretching in PVDF film. Hence, the processing of this copolymer is more convenient than PVDF. While the copolymers' unit structures are less polar than that of pure PVDF, the copolymer improves the crystallinity of the material, which results in a larger piezoelectric response. The d_{33} values for P(VDF-TrFE) have been recorded to be as high as -38 pC/N [50] versus -33 pC/N in PVDF homopolymer.

Various applications based on P(VDF-TrFE) have been developed due to its excellent ferroelectric and piezoelectric properties. However, the utility of P(VDF/TrFE) at high temperature is limited due to its low Curie temperature. In

addition, the very high cost and poor commercial availability also restrict the practical applications of P(VDF/TrFE).

1.2.3 Application of PVDF-based thin films

PVDF and its copolymers are used in a large number of applications. Generally, PVDF is used in applications requiring the highest purity, strength, and resistance to solvents, acids, bases and heat and low smoke generation during a fire event. Since the first discovering of piezoelectricity effect in PVDF by Kawai in 1969, PVDF and its copolymers have been used in a large number of electrical device applications.

The major applications of piezoelectric PVDF include microphones and loudspeakers, transducers, actuators, medical ultrasound and hydrophones [51]. Other possible application areas include tactile devices [52], energy conversion [53], pyroelectric infrared sensors [54] and shock sensors[55].

1.3 One-dimensional ferroelectric nanomaterials

1.3.1 Recent progress of one-dimensional ferroelectric nanomaterials

In the past two decades, there have been great research interests on the fabrication and characterization of low-dimensional nanostructures, such as ultrathin films, nanoparticles, nanotubes and nanowires. Nanosized materials usually exhibit electronic and optical properties somewhat different from the same bulk materials

because of their quantum tunable electronic properties, which emerge as a function of size (the so-called quantum size effect). The low-dimensional nanostructures are expected to become functional elements in electronic, electrochemical, and electromechanical devices at a much smaller scale. Hence nanomaterials have large potential applications in various fields including electronics, photonics, sensors and energy harvesting and information storage.

Ferroelectric and piezoelectric nanostructures have received much attention because of the unique properties and novel applications in optical and electronic devices [56, 57]. One-dimensional nanostructures, such as nanobelts, nanotubes and nanowires have been fabricated. Nanohelixes, nanosprings, and nanorings based on Zinc oxide (ZnO) nanobelts have been reported by X. Y. Kong and Z. L. Wang [58]; piezoelectricity and polarization-induced ferroelectricity at nanoscale have been observed in these nanostructures. PZT nanotubes and nanorods have been reported to be obtained from sol-gel deposition in AAM template, hydrothermal synthesis and electro spinning process. Besides the wide researches on ZnO and PZT, nanostructures based on various piezoelectric and ferroelectric materials have been demonstrated, such as the perovskites $KNbO_3$ nanorods [59], $BaTiO_3$ [60], $BiFeO_3$ [61] and $(K_{0.5}Na_{0.5})NbO_3$ nanotubes [62].

The piezoelectric effect of ferroelectric materials makes it useful in sensors, actuators and energy harvesting devices. It has been reported that Wang et al. used a

conducting atomic force microscope (AFM) tip to probe the piezoelectric voltage response of ZnO nanowires under mechanical deformation by the AFM tip, followed by several demonstrations of packaged ZnO-based nanogenerator devices converting nano-scale mechanical energy into electric energy; efficiency of about 17-30% was achieved [63]. Nanogenerators based on other piezoelectric materials that have also been reported, such as CdS [64], GaN [65], $BaTiO_3$ [66], $LiNbO_3$ and PMN-PT [67]. Besides the obvious advantage of being nanoscale in size, nanowires can more effectively confine strain in the axial direction, hence they are desirable structures for piezoelectric generator applications. Furthermore, the switchable spontaneous electric polarization in ferroelectrics can present the 1 or 0 situation in data storage applications [68, 69]. Other devices such as capacitors, acoustic resonators, field-effect transistor and piezoelectric-gated diode have also been demonstrated [70].

While much research efforts on one-dimensional nanostructures have focused on the fabrication and device applications of ferroelectric and piezoelectric ceramics, there have also been some approaches based on ferroelectric polymers. Ferroelectric polymers have attracted considerable research interests due to their light-weight, flexible and non-toxic properties, making them appealing in comparison to inorganic ferroelectrics. They are suitable for many applications including non-volatile memories, piezoelectric sensors and dielectric capacitors. Cheng Liang Sun has prepared Ni/P(VDF-TrFE) nanoscaled coaxial cables with Ni nanowires as the cores

and P(VDF-TrFE) nanotubes as the shells by a two-step process [71]. The polymer nanotubes are released and become separate when the template is etched. R. K. Zheng and his group have first prepared nanowires and nanotubes using the ferroelectric copolymer P(VDF-TrFE) [72, 73]. The nanowire and nanotube array are formed on a bulk polymer film. High-density arrays of P(VDF-TrFE) nanopillars that could act as non-volatile low-voltage memories have also been reported [74]. Cha et al. have demonstrated nanogenerators based on porous PVDF that could produce rectified power density of 0.17 mW/cm^3 [75].

Despite the progress that has been made, there're still some deficiencies with the above mentioned approaches. The previous reported nanotube structures are open at both ends [71, 72], which is unsuitable for capacitor application since the inner and outer electrodes may short at the open ends. Hence nanotubes with sealed ends may be more desirable for such applications. In the area of energy harvesting, there is also much potential for improvement. For instance, the more deformable hollow nanotubes may have superior performance to the reported nanoporous structure [75] for energy harvesting. However, no such work has been reported.

1.3.2 Synthesis of one-dimensional nanomaterials

A variety of preparation methods, including electrodeposition, laser ablation, vapour phase transport [76], chemical vapour deposition (CVD) [77], sol–gel [78], arc-discharge, catalytic growth via vapour–liquid–solid mechanism [79],

solution-phase reactions, sonochemical, solvothermal and hydrothermal synthesis, have been developed to fabricate nanostructures of a broad range of materials, such as metals and metal alloys, carbon, semiconductors, oxide ceramics and electronically conductive polymers .

Among those fabrication methods, the template approach has been extensively investigated. This method entails synthesizing the desired material within the pores of a nanoporous membrane, which has cylindrical pores of uniform diameter. The method is most commonly and widely used to prepare freestanding, non-oriented and oriented nanowires or nanotubes. The template-based method can be used in preparing nanostructure of quite a lot different kind of materials, such as polymers, metals, semiconductors, carbon, and other materials. The mono-dispersed, highly oriented and ordered one-dimensional nanostructures can be obtained in membranes. Moreover, the template can be easily removed via chemical etching or plasma etching so as to free the nanowires or nanotubes synthesized. Anodized alumina membrane (AAM) and radiation track-etched polycarbonate (PC) membranes are two major classes of the most commonly used and commercially available templates. Martin and his group have used track-etch PC or polyester membranes and AAM to synthesize conductive polymer nanotubes [80]. Other solid porous materials, such as zeolites, silica-based mesoporous molecular sieves, oxides, graphite composites, polyoxometallate, and previously synthesized nanostructure can also be used as hard template in synthesis of nanostructures. Bio-templates are also explored for the

growth of nanowires and nanotubes, such as Cu , Ni , Co, and Au nanowires [81].

The anodic alumina membrane (AAM), which is also known as porous alumina membrane (PAM) or anodic aluminum oxide (AAO), is a typical self-ordered porous material which exhibits hexagonally arranged cells with cylindrical pores in the center, has been extensively studied for several decades. Usually, the AAM templates have been fabricated by anodizing aluminum foils. The oxide has a cellular structure with a central pore in each hexagonal cell.

AAM is widely used in the synthesis of nanotube/nanowire structures due to its remarkable hardness, uniform pore size, high pore density together with potentially low cost and relative ease of their preparation. The fabrication methods of nanostructure with inorganic materials that use AAM as template include hydrothermal solution synthesis, chemical vapor deposition, thermal evaporation, electrodeposition [82, 83], layer-by-layer deposition [84], and methods using commercially available metal-plating solutions. Polymer nanotubes or nanorods can be synthesized by the template-directed polymerization of corresponding monomers [85], or by wetting the template with polymer melts or solutions [86,87]. AAM is especially useful in the template wetting synthesis of polymer nanofibers because of its relatively high surface free energy, which enhances the wetting of polymer solution or melt, so as to enable the formation of polymer nanofibers. In my research work, nanotube array of PVDF and P(VDF-TrFE) has been demonstrated in AAM

template, and the investigation of these nanostructures will be discussed in following chapters.

1.4 Motivation and Objectives

As stated above, the ferroelectric polymer PVDF and its copolymers have been extensively studied due to their remarkable properties. While most studies have focused on bulk materials, recently polymer-based thin films and nanostructures have attracted much attention. These low dimensional structures possess unique properties such as enhanced sensitivity and large surface area, thus having great potential in device applications including sensors, supercapacitors, non-volatile memory and nanogenerators. A main objective of this work is to fabricate PVDF-based thin films and nanostructures with excellent performance using low-cost, scalable and convenient methods, and study their potential applications in energy storage and energy harvesting. In particular, PVDF-based nanotube array in which the nanotubes are sealed in one end and connected in the other open end, are designed, produced and investigated. Electrode coatings have been deposited on both sides of the nanotubes to enlarge the contact area.

Compared to the copolymer P(VDF/TrFE), PVDF homopolymer possesses many advantages, such as larger intrinsic polarization, higher Curie temperature, higher breakdown strength, significantly lower cost and ready availability. However, it is

always challenging to directly obtain the highly polar β phase in PVDF homopolymer. In this study, we aim to achieve ferroelectric β phase in PVDF homopolymer thin films and nanostructures and investigate the mechanism of β phase formation. Various approaches have been studied, including incorporation of hydrated salt, Langmuir-Blodgett (LB) deposition and solution deposittion in AAM template.

1.5 Organization of the thesis

This thesis contains 8 chapters, including this introduction as Chapter 1.

Chapter 2 introduces the facilities and methods involved in preparation and characterization of PVDF and P(VDF-TrFE) thin films and nanostructures in AAM template. The preparation condition of self-ordered AAM with desired pore size and length is also described.

Chapter 3 presents the structure and characterization of P(VDF-TrFE) nanotube array fabricated in AAM template. Electroless-plated Ag layers were deposited on both inner and outer sides of the nanotubes as electrodes, which greatly enlarged the contact area between the electrodes and the polymer dielectric. Hence, enhanced capacitance is expected in this nanostructure. The capacitance is theoretically calculated and experimentally measured.

Chapter 4 presents the structure and piezoelectric response of P(VDF-TrFE) copolymer nanotube array. Mechanical energy harvesting has been experimentally demonstrated for the first time with piezoelectric P(VDF-TrFE) nanotube array, using a conducting AFM tip to provide periodic mechanical deformation and also to measure the generated current.

Chapter 5 presents a systematic study on solution-derived ferroelectric PVDF homopolymer thin films on substrates. Hydrate salts are introduced in PVDF precursor solution and PVDF thin film is fabricated by spin coating method. The retaining and loss of water in PVDF film introduced by hydrated salts are manipulated to promote formation of β phase crystals, and the resulting films show electrical properties comparable to those of P(VDF-TrFE). Further more, the structure and properties of PVDF ultra-thin films (thickness in 50 nm or below) prepared by LB deposition are studied. The observation of formation of β-phase structure in PVDF LB films is presented and the mechanism of the β-phase promotion is discussed.

Chapter 6 presents an investigation of the β phase promotion mechanism in PVDF nanotubes fabricated in AAM template. The mechanism of β phase formation by the hydrogen bonding interaction between hydroxyl groups on AAM surface and PVDF chain is identified.

Chapter 7 presents the conclusions.

Chapter 8 gives the recommendations for future work.

References

[1]   R. Mindlin, "Elasticity, piezoelectricity and crystal lattice dynamics," *Journal of Elasticity,* vol. 2, pp. 217-282, 1972.

[2]   T. O. Ikeda, *Fundamentals of piezoelectricity. Oxford University Press*, 1990.

[3]   C. A. L. Bassett, "Biologic significance of piezoelectricity," *Calcified Tissue International,* vol. 1, pp. 252-272, 1967.

[4]   M. E. Lines and A. M. Glass, *Principles and Applications of Ferroelectrics and Related Materials*: Clarendon Press, 1977.

[5]   G. Bertotti and I. D. Mayergoyz, *The Science of Hysteresis: Mathematical modeling and applications*: Elsevier, 2006.

[6]   F. Cruickshank, "Ferroelectric Materials and their Applications," 1992.

[7]   Z. Suo, C. M. Kuo, D. Barnett, and J. Willis, "Fracture mechanics for piezoelectric ceramics," *Journal of the Mechanics and Physics of Solids,* vol. 40, pp. 739-765, 1992.

[8]   T. Takenaka and H. Nagata, "Current status and prospects of lead-free piezoelectric ceramics," *Journal of the European Ceramic Society,* vol. 25,

pp. 2693-2700, 2005.

[9]   G. H. Haertling, "Ferroelectric ceramics: History and technology," *Journal of the American Ceramic Society,* vol. 82, pp. 797-818, Apr 1999.

[10]   K. Amanuma, T. Mori, T. Hase, T. Sakuma, A. Ochi, and Y. Miyasaka, "Ferroelectric Properties of Sol-Gel Derived Pb (Zr, Ti) O~ 3 Thin Films," *JAPANESE JOURNAL OF APPLIED PHYSICS PART 1 REGULAR PAPERS SHORT NOTES AND REVIEW PAPERS,* vol. 32, pp. 4150-4150, 1993.

[11]   B. H. Park, B. S. Kang, S. D. Bu, T. W. Noh, J. Lee, and W. Jo, "Lanthanum-substituted bismuth titanate for use in non-volatile memories," *Nature,* vol. 401, pp. 682-684, Oct 1999.

[12]   R. Guo, L. E. Cross, S. E. Park, B. Noheda, D. E. Cox, and G. Shirane, "Origin of the high piezoelectric response in PbZr1-xTixO3," *Physical Review Letters,* vol. 84, pp. 5423-5426, Jun 2000.

[13]   B. Ravel, E. A. Stern, R. I. Vedrinskii, and V. Kraizman, "Local structure and the phase transitions of BaTiO3," *Ferroelectrics,* vol. 206, pp. 407-430, 1998.

[14]   A. Vonhippel, "FERROELECTRICITY, DOMAIN STRUCTURE, AND PHASE TRANSITIONS OF BARIUM TITANATE," *Reviews of Modern Physics,* vol. 22, pp. 221-237, 1950.

[15]   B. J. Chu, D. R. Chen, G. R. Li, and Q. R. Yin, "Electrical properties of Na1/2Bi1/2TiO3-BaTiO3 ceramics," *Journal of the European Ceramic Society,* vol. 22, pp. 2115-2121, Dec 2002.

[16] J. R. Gomah-Pettry, E. Said, P. Marchet, and J. P. Mercurio, "Sodium-bismuth titanate based lead-free ferroelectric materials," *Journal of the European Ceramic Society,* vol. 24, pp. 1165-1169, 2004.

[17] J. Kreisel, A. M. Glazer, P. Bouvier, and G. Lucazeau, "High-pressure Raman study of a relaxor ferroelectric: The Na0.5Bi0.5TiO3 perovskite," *Physical Review B,* vol. 63, May 2001.

[18] G. A. Smolenskii, V. A. Isupov, A. I. Agranovskaya, and N. N. Krainik, "NEW FERROELECTRICS OF COMPLEX COMPOSITION .4," *Soviet Physics-Solid State,* vol. 2, pp. 2651-2654, 1961 1961.

[19] J. F. Li, K. Wang, B. P. Zhang, and L. M. Zhang, "Ferroelectric and piezoelectric properties of fine-grained Na0.5K0.5NbO3 lead-free piezoelectric ceramics prepared by spark plasma sintering," *Journal of the American Ceramic Society,* vol. 89, pp. 706-709, Feb 2006.

[20] K. Wang, J.-F. Li, and N. Liu, "Piezoelectric properties of low-temperature sintered Li-modified (Na, K)NbO3 lead-free ceramics," *Applied Physics Letters,* vol. 93, Sep 1 2008.

[21] Y. Zhen and J.-F. Li, "Normal sintering of (K,Na)NbO3-based ceramics: Influence of sintering temperature on densification, microstructure, and electrical properties," *Journal of the American Ceramic Society,* vol. 89, pp. 3669-3675, Dec 2006.

[22] G. Catalan and J. F. Scott, "Physics and Applications of Bismuth Ferrite," *Advanced Materials,* vol. 21, pp. 2463-2485, Jun 26 2009.

[23] R. Safi and H. Shokrollahi, "Physics, chemistry and synthesis methods of nanostructured bismuth ferrite (BiFeO3) as a ferroelectro-magnetic material," *Progress in Solid State Chemistry,* vol. 40, pp. 6-15, Jun 2012.

[24] E. Fukada, "History and recent progress in piezoelectric polymers," *Ultrasonics, Ferroelectrics and Frequency Control, IEEE Transactions on,* vol. 47, pp. 1277-1290, 2000.

[25] E. Fukada, "PIEZOELECTRICITY OF WOOD," *Journal of the Physical Society of Japan,* vol. 10, pp. 149-154, 1955.

[26] E. Fukada and I. Yasuda, "ON THE PIEZOELECTRIC EFFECT OF BONE," *Journal of the Physical Society of Japan,* vol. 12, pp. 1158-1162, 1957.

[27] E. Fukada, "ON THE PIEZOELECTRIC EFFECT OF SILK FIBERS," *Journal of the Physical Society of Japan,* vol. 11, pp. 1301-1301, 1956.

[28] H. Kawai, "PIEZOELECTRICITY OF POLY (VINYLIDENE FLUORIDE)," *Japanese Journal of Applied Physics,* vol. 8, pp. 975-&, 1969.

[29] S. L. Wu, J. I. Scheinbeim, and B. A. Newman, "Ferroelectricity and piezoelectricity of nylon 11 films with different draw ratios," *Journal of Polymer Science Part B-Polymer Physics,* vol. 37, pp. 2737-2746, Oct 1999.

[30] E. Fukada, "New piezoelectric polymers," *Japanese Journal of Applied Physics Part 1-Regular Papers Short Notes & Review Papers,* vol. 37, pp. 2775-2780, May 1998.

[31] E. Fukada, "PYROELECTRICITY AND PIEZOELECTRICITY OF POLYUREA," *Ferroelectric Polymers and Ceramic-Polymer Composites,*

vol. 92-9, pp. 143-159, 1994.

[32]   L. H. Dawson, "Piezoelectricity of crystal quartz," *Physical Review,* vol. 29, pp. 0532-0541, Apr 1927.

[33]   E. Fukada, "History and recent progress in piezoelectric polymers," *Ieee Transactions on Ultrasonics Ferroelectrics and Frequency Control,* vol. 47, pp. 1277-1290, Nov 2000.

[34]   R. G. Kepler and R. A. Anderson, "PIEZOELECTRICITY AND PYROELECTRICITY IN POLYVINYLIDENE FLUORIDE," *Journal of Applied Physics,* vol. 49, pp. 4490-4494, 1978.

[35]   M. G. Broadhurst, G. T. Davis, J. E. McKinney, and R. E. Collins, "PIEZOELECTRICITY AND PYROELECTRICITY IN POLYVINYLIDENE FLUORIDE - MODEL," *Journal of Applied Physics,* vol. 49, pp. 4992-4997, 1978.

[36]   D. C. Bassett, *Developments in crystalline polymers*: Applied Science Publishers, 1982.

[37]   R. Gregorio and M. Cestari, "EFFECT OF CRYSTALLIZATION TEMPERATURE ON THE CRYSTALLINE PHASE CONTENT AND MORPHOLOGY OF POLY(VINYLIDENE FLUORIDE)," *Journal of Polymer Science Part B-Polymer Physics,* vol. 32, pp. 859-870, Apr 15 1994.

[38]   G. T. Davis, J. E. McKinney, M. G. Broadhurst, and S. C. Roth, "ELECTRIC-FIELD-INDUCED PHASE-CHANGES IN POLY(VINYLIDENE FLUORIDE)," *Journal of Applied Physics,* vol. 49, pp.

4998-5002, 1978 1978.

[39]   W. W. Doll and J. B. Lando, "POLYMORPHISM OF POLY(VINYLIDENE FLUORIDE) .3. CRYSTAL STRUCTURE OF PHASE-II," *Journal of Macromolecular Science-Physics,* vol. B 4, pp. 309-&, 1970 1970.

[40]   A. Salimi and A. A. Yousefi, "FTIR studies of beta-phase crystal formation in stretched PVDF films," *Polymer Testing,* vol. 22, pp. 699-704, Sep 2003.

[41]   J. Humphreys, E. L. V. Lewis, I. M. Ward, E. L. Nix, and J. C. McGrath, "A STUDY OF THE MECHANICAL ANISOTROPY OF HIGH-DRAW, LOW-DRAW, AND VOIDED PVDF," *Journal of Polymer Science Part B-Polymer Physics,* vol. 26, pp. 141-158, Jan 1988.

[42]   T. Hattori, M. Kanaoka, and H. Ohigashi, "Improved piezoelectricity in thick lamellar beta-form crystals of poly(vinylidene fluoride) crystallized under high pressure," *Journal of Applied Physics,* vol. 79, pp. 2016-2022, Feb 1996.

[43]   P. Costa, J. Silva, V. Sencadas, C. M. Costa, F. W. J. van Hattum, J. G. Rocha, and S. Lanceros-Mendez, "The effect of fibre concentration on the alpha to beta-phase transformation, degree of crystallinity and electrical properties of vapour grown carbon nanofibre/poly(vinylidene fluoride) composites," *Carbon,* vol. 47, pp. 2590-2599, Sep 2009.

[44]   Y.-L. Liu, Y. Li, J.-T. Xu, and Z.-Q. Fan, "Cooperative Effect of Electrospinning and Nanoclay on Formation of Polar Crystalline Phases in Poly(vinylidene fluoride)," *Acs Applied Materials & Interfaces,* vol. 2, pp.

1759-1768, Jun 2010.

[45]   A. Lund, C. Gustafsson, H. Bertilsson, and R. W. Rychwalski, "Enhancement of beta phase crystals formation with the use of nanofillers in PVDF films and fibres," *Composites Science and Technology,* vol. 71, pp. 222-229, Jan 17 2011.

[46]   R. Gregorio and D. S. Borges, "Effect of crystallization rate on the formation of the polymorphs of solution cast poly(vinylidene fluoride)," *Polymer,* vol. 49, pp. 4009-4016, Aug 2008.

[47]   M. Benz, W. B. Euler, and O. J. Gregory, "The role of solution phase water on the deposition of thin films of poly(vinylidene fluoride)," *Macromolecules,* vol. 35, pp. 2682-2688, Mar 26 2002.

[48]   S. Chen, K. Yao, F. E. H. Tay, and C. L. Liow, "Ferroelectric poly(vinylidene fluoride) thin films on Si substrate with the beta phase promoted by hydrated magnesium nitrate," *Journal of Applied Physics,* vol. 102, Nov 2007.

[49]   X. He and K. Yao, "Crystallization mechanism and piezoelectric properties of solution-derived ferroelectric poly(vinylidene fluoride) thin films," *Applied Physics Letters,* vol. 89, Sep 11 2006.

[50]   H. Ohigashi, K. Omote, H. Abe, and K. Koga, "Chain motions in the paraelectric phase in single crystalline films of vinylidene fluoride and trifluoroethylene copolymer P(VDF/TrFE)," *Journal of the Physical Society of Japan,* vol. 68, pp. 1824-1827, Jun 1999.

[51]   S. B. Lang, "Guide to the literature of piezoelectricity and pyroelectricity.

22," *Ferroelectrics,* vol. 308, pp. 193-304, 2004 2004.

[52]   M. A. Razian and M. G. Pepper, "Design, development, and characteristics of an in-shoe triaxial pressure measurement transducer utilizing a single element of piezoelectric copolymer film," *Ieee Transactions on Neural Systems and Rehabilitation Engineering,* vol. 11, pp. 288-293, Sep 2003.

[53]   G. W. Taylor, J. R. Burns, S. M. Kammann, W. B. Powers, and T. R. Welsh, "The energy harvesting eel: A small subsurface ocean/river power generator," *Ieee Journal of Oceanic Engineering,* vol. 26, pp. 539-547, Oct 2001.

[54]   R. Kohler, N. Neumann, and G. Hofmann, "PYROELECTRIC SINGLE-ELEMENT AND LINEAR-ARRAY SENSORS BASED ON P(VDF TRFE) THIN-FILMS," *Sensors and Actuators a-Physical,* vol. 45, pp. 209-218, Dec 1994.

[55]   F. Bauer, "PVDF shock sensors: Applications to polar materials and high explosives," *Ieee Transactions on Ultrasonics Ferroelectrics and Frequency Control,* vol. 47, pp. 1448-1454, Nov 2000.

[56]   B. Halford, "Chemists of color," *Chemical & Engineering News,* vol. 85, pp. 46-49, Mar 2007.

[57]   Z. L. Wang, "Nanopiezotronics," *Advanced Materials,* vol. 19, pp. 889-892, Mar 2007.

[58]   X. Y. Kong and Z. L. Wang, "Spontaneous polarization-induced nanohelixes, nanosprings, and nanorings of piezoelectric nanobelts," *Nano Lett,* vol. 3, pp. 1625-1631, Dec 2003.

[59]   G. Z. Wang, Y. D. Yu, T. Grande, and M. A. Einarsrud, "Synthesis of KNbO3 Nanorods by Hydrothermal Method," *Journal of Nanoscience and Nanotechnology,* vol. 9, pp. 1465-1469, Feb 2009.

[60]   Y. F. Zhu, L. Zhang, T. Natsuki, Y. Q. Fu, and Q. Q. Ni, "Facile Synthesis of BaTiO3 Nanotubes and Their Microwave Absorption Properties," *Acs Applied Materials & Interfaces,* vol. 4, pp. 2101-2106, Apr 2012.

[61]   C. Y. Li, B. Liu, J. P. Zhao, J. F. Wang, B. B. Hu, and Z. L. Du, "Synthesis and characterization of BiFeO3 nanotube arrays and Y-junction BiFeO3 nanotubes," *Chinese Science Bulletin,* vol. 54, pp. 719-722, Mar 2009.

[62]   D. Zhou, H. S. Gu, Y. M. Hu, H. Y. Tian, Z. Wang, Z. L. Qian, and Y. Wang, "Synthesis, characterization and ferroelectric properties of lead-free K0.5Na0.5NbO3 nanotube arrays," *Journal of Applied Physics,* vol. 109, Jun 2011.

[63]   Z. L. Wang and J. H. Song, "Piezoelectric nanogenerators based on zinc oxide nanowire arrays," *Science,* vol. 312, pp. 242-246, Apr 2006.

[64]   K. F. Wu, H. M. Zhu, Z. Liu, W. Rodriguez-Cordoba, and T. Q. Lian, "Ultrafast Charge Separation and Long-Lived Charge Separated State in Photocatalytic CdS-Pt Nanorod Heterostructures," *Journal of the American Chemical Society,* vol. 134, pp. 10337-10340, Jun 2012.

[65]   R. G. Hobbs, N. Petkov, and J. D. Holmes, "Semiconductor Nanowire Fabrication by Bottom-Up and Top-Down Paradigms," *Chemistry of Materials,* vol. 24, pp. 1975-1991, Jun 2012.

[66] Z. Y. Wang, J. Hu, A. P. Suryavanshi, K. Yum, and M. F. Yu, "Voltage generation from individual BaTiO3 nanowires under periodic tensile mechanical load," *Nano Lett,* vol. 7, pp. 2966-2969, Oct 2007.

[67] R. W. C. Lewis, C. R. Bowen, V. Y. Topolov, and D. W. E. Allsopp, "Role of Single-Crystal Pillars in Forming the Effective Properties and Figures of Merit of Novel 1-3 Piezocomposites," *Integrated Ferroelectrics,* vol. 133, pp. 103-108, 2012.

[68] Z. L. Wang, X. Y. Kong, Y. Ding, P. X. Gao, W. L. Hughes, R. S. Yang, and Y. Zhang, "Semiconducting and piezoelectric oxide nanostructures induced by polar surfaces," *Advanced Functional Materials,* vol. 14, pp. 943-956, Oct 2004.

[69] Z. L. Wang, "Towards Self-Powered Nanosystems: From Nanogenerators to Nanopiezotronics," *Advanced Functional Materials,* vol. 18, pp. 3553-3567, Nov 2008.

[70] Z. L. Wang, "The new field of nanopiezotronics," *Materials Today,* vol. 10, pp. 20-28, May 2007.

[71] C. L. Sun, K. H. Lam, C. Chao, S. T. Lau, H. L. W. Chan, S. S. Guo, and X. Z. Zhao, "Fabrication and characterization of Ni/P(VDF-TrFE) nanoscaled coaxial cables," *Applied Physics Letters,* vol. 90, Jun 2007.

[72] R. K. Zheng, H. L. W. Chan, and C. L. Choy, "A simple template-based hot-press method for the fabrication of metal and polymer nanowires and nanotubes," *Nanotechnology,* vol. 16, pp. 1928-1934, 2005.

[73]   R. K. Zheng, Y. Yang, Y. Wang, J. Wang, H. L. Chan, C. L. Choy, C. G. Jin, and X. G. Li, "A simple and convenient route to prepare poly(vinylidene fluoride trifluoroethylene) copolymer nanowires and nanotubes," *Chem Commun (Camb),* pp. 1447-1449, Mar 21 2005.

[74]   Z. J. Hu, M. W. Tian, B. Nysten, and A. M. Jonas, "Regular arrays of highly ordered ferroelectric polymer nanostructures for non-volatile low-voltage memories," *Nature Materials,* vol. 8, pp. 62-67, Jan 2009.

[75]   S. Cha, S. M. Kim, H. Kim, J. Ku, J. I. Sohn, Y. J. Park, B. G. Song, M. H. Jung, E. K. Lee, B. L. Choi, J. J. Park, Z. L. Wang, J. M. Kim, and K. Kim, "Porous PVDF as effective sonic wave driven nanogenerators," *Nano Lett,* vol. 11, pp. 5142-7, Dec 14 2011.

[76]   M. S. Gudiksen, L. J. Lauhon, J. Wang, D. C. Smith, and C. M. Lieber, "Growth of nanowire superlattice structures for nanoscale photonics and electronics," *Nature,* vol. 415, pp. 617-620, Feb 2002.

[77]   L. Cademartiri and G. A. Ozin, "Ultrathin Nanowires - A Materials Chemistry Perspective," *Advanced Materials,* vol. 21, pp. 1013-1020, Mar 6 2009.

[78]   T. Kasuga, M. Hiramatsu, A. Hoson, T. Sekino, and K. Niihara, "Formation of titanium oxide nanotube," *Langmuir,* vol. 14, pp. 3160-3163, Jun 1998.

[79]   B. L. Cushing, V. L. Kolesnichenko, and C. J. O'Connor, "Recent advances in the liquid-phase syntheses of inorganic nanoparticles," *Chemical Reviews,* vol. 104, pp. 3893-3946, Sep 2004.

[80]   J. C. Hulteen and C. R. Martin, "A general template-based method for the

preparation of nanomaterials," *Journal of Materials Chemistry,* vol. 7, pp. 1075-1087, Jul 1997.

[81]   R. Gasparac, P. Kohli, M. O. Mota, L. Trofin, and C. R. Martin, "Template synthesis of nano test tubes," *Nano Lett,* vol. 4, pp. 513-516, Mar 2004.

[82]   Y. G. Guo, L. J. Wan, C. F. Zhu, D. L. Yang, D. M. Chen, and C. L. Bai, "Ordered Ni-Cu nanowire array with enhanced coercivity," *Chemistry of Materials,* vol. 15, pp. 664-667, Feb 2003.

[83]   J. G. Wang, M. L. Tian, N. Kumar, and T. E. Mallouk, "Controllable template synthesis of superconducting Zn nanowires with different microstructures by electrochemical deposition," *Nano Lett,* vol. 5, pp. 1247-1253, Jul 2005.

[84]   T. D. Lazzara, K. H. A. Lau, A. I. Abou-Kandil, A.-M. Caminade, J.-P. Majoral, and W. Knoll, "Polyelectrolyte Layer-by-Layer Deposition in Cylindrical Nanopores," *Acs Nano,* vol. 4, pp. 3909-3920, Jul 2010.

[85]   E. N. Konyushenko, J. Stejskal, I. Sedenkova, M. Trchova, I. Sapurina, M. Cieslar, and J. Prokes, "Polyaniline nanotubes: conditions of formation," *Polymer International,* vol. 55, pp. 31-39, Jan 2006.

[86]   M. Steinhart, S. Senz, R. B. Wehrspohn, U. Gosele, and J. H. Wendorff, "Curvature-directed crystallization of poly(vinylidene difluoride) in nanotube walls," *Macromolecules,* vol. 36, pp. 3646-3651, May 2003.

[87]   J. Martin, J. Maiz, J. Sacristan, and C. Mijangos, "Tailored polymer-based nanorods and nanotubes by "template synthesis": From preparation to applications," *Polymer,* vol. 53, pp. 1149-1166, Mar 2012.

Chapter 2   Experimental techniques

2.1 Fabrication of PVDF thin films

PVDF thin films on substrate were prepared by spin-coating or Langmuir-Blodgett (LB) deposition. The precursor solutions of PVDF were prepared by dissolving the polymer powder in the mixed solvent of DMF and acetone (50:50 in volume). To study the effect of β-phase PVDF promotion, hydrated or hygroscopic chemicals were added into some of the precursor solutions to promote β-phase crystallization. The solutions were heated at 50 °C in silicone oil bath for 1 hour to completely dissolve the polymer. The PVDF films were deposited by spin coating the solution on aluminum coated silicon substrates and immediately dried on a hotplate at 100 °C for 10 minutes. The samples were then annealed at 135 °C for 12 hours in an oven to improve the crystallinity. Gold electrodes for electrical testing with a thickness of 300 nm were deposited on the films by DC sputtering.

The LB deposition is a long-established method of obtaining uniform molecular monolayers, and has the advantage of controlling film thickness in an ideal accuracy of one molecular layer [1-3]. This method involves the layer-by-layer transfer of monomolecular films, commonly referred to as Langmuir layers, from a liquid subphase to a solid substrate. Langmuir layers consist of amphiphilic molecules that possess both a polar hydrophilic head-group and a non-polar hydrophobic tail-group. The competing hydrophilic and hydrophobic components of the given molecule

result in a monomolecular layer confined to the gas-liquid interface. The LB

monolayer of amphiphilic molecules on the surface of a liquid is formed in a LB

trough by spreading a diluted solution on surface. The monolayer is transferred to

substrate by pressing the substrate on surface, and then the barriers of the trough

compress the surface to recover the monolayer.
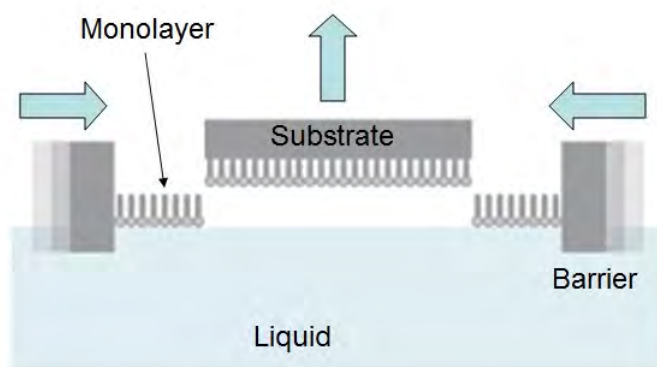
Figure 2.1 Schematic illustration of the LB deposition process

Figure 2.1 shows the process of LB deposition. In this work, the LB deposition

process was performed in a commercial LB trough (Model 622C, Nima Technology).

The LB trough was thoroughly cleaned and filled with ultrapurified (> 18 MΩ cm)

water. The water surface was compressed and suctioned until there was no

measurable pressure change with area, indicating a clean water surface. Langmuir

monolayers of the polymer were prepared by spreading a dilute solution (0.05 wt%)

of the PVDF-based materials. The Langmuir layer was allowed to sit for two hours

to provide sufficient time for the solvent to evaporate. The Langmuir layer was then

compressed by closing the trough barriers slowly until the solid phase surface

pressure of 5 mN/m was achieved and this pressure was maintained throughout the

deposition process. The films were transferred to Au-coated SiO_2/Si substrate one layer at a time using the Schaefer horizontal deposition. During the deposition, the LB films were dried at room temperature for 5 min after each transfer of one monolayer. After transferred for 20 cycles, the final LB films were annealed at 135 ^{o}C for 4 hours in an oven to improve the degree of crystallization.

2.2 Fabrication of AAM template, PVDF and P(VDF-TrFE) nanotubes

Self-ordered porous AAM templates are fabricated by a two-step anodization of high-purity aluminum foil [4, 5]. The aluminum foil is annealed at 450 ^{o}C for 2 hours to remove residual stress and defects present from the manufacturing process. The back surface of the aluminum piece is first coated with a resin to ensure membrane growth only occurs on a single face of the aluminum piece. The aluminum piece is then connected to a DC power source and placed into the electrolyte solution for anodization. The electrolyte is placed in a cooling system and constantly stirred to reduce local temperature build up on the aluminum surface, which could lead to abnormal growth of the AAM. The oxide layer grown during this first anodization process is irregular in nature. To produce highly ordered AAM, the oxide layer formed by the first anodization process is etched away and a second anodization step is carried out. After the oxide layer formed in first anodization is etched off, periodic concave patterns are left on surface, and the patterns will act as

self-assembled template for the second anodization, resulting in highly ordered pore formation. Highly ordered AAM layer was formed during a second anodization step under similar conditions, after which the pores were enlarged by etching in acid.

The anodization voltage controls the resulting pore diameter and inter-pore distance of the template synthesized, both of which increase as the anodization voltage increases. From Fig 2.2 below, it can be seen that there is a linear relationship between the cell diameter and the anodization voltage where an increase in anodization voltage leads to a linear increase in cell diameter. The general equation relating pore diameter to anodization voltage is given by $D_{pore} = 1.29U$, where D_{pore} is the pore diameter and U is the anodization voltage with a proportionality constant of 1.29 nm/V.
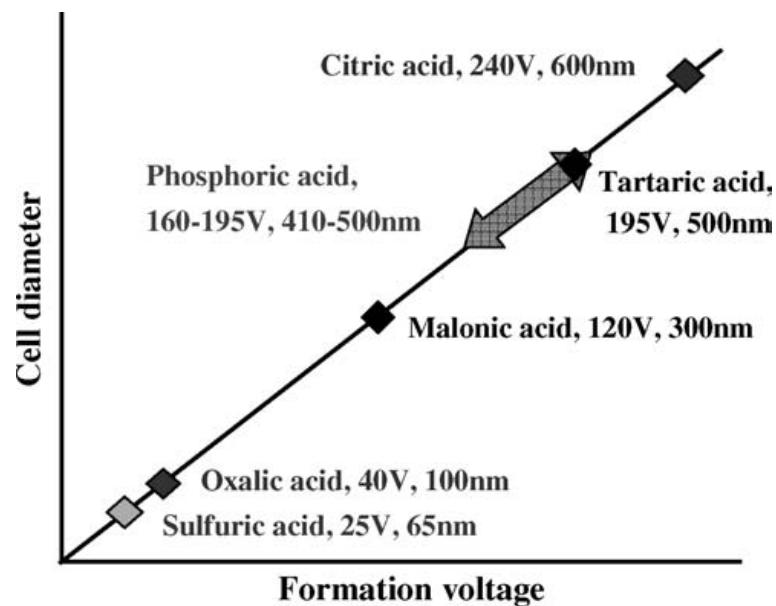
Figure 2.2 Graph of self-ordering voltages and corresponding cell-diameters for various commonly used electrolytes. [6]

The electrolyte solutions commonly used for the anodization of aluminum are usually sulphuric acid, oxalic acid and phosphoric acid. The type of acid used is chosen based on the anodization voltage range used [6]. There is an upper limit to the anodization voltage for a particular electrolyte. Above this limit, a local film thickening occurs as a result of an extremely high current with black spots of thickened film often being seen in the electrolyte solution. This effect is termed "burning" and is undesirable in the fabrication of the AAM templates. If a larger anodization voltage is required, a different electrolyte which can handle the anodization voltage is then chosen [7].

To obtain a highly ordered cell alignment, it would be beneficial to carry out anodization using a high electric field which can be attained by adopting a higher anodization voltage [8, 9]. The rapid oxide growth under the high field condition exerts a compressive force at the barrier layer, resulting in the bottom of the cells pressing against each other so that self-ordering proceeds together with the growth of the porous film.

In this work, high purity Al foil (99.99%, Goodfellow) was anodized in 5 wt% H_3PO_4 (H_2O: Ethanol = 1:1 in volume) under a constant applied voltage of 150 V for 6 h at 4 ^{o}C. The anodized alumina layer formed in the previous step was etched away with a water based acid mixture of 6 wt% H_3PO_4 and 1.8 wt% $HCrO_4$. Highly ordered AAM layer was formed during a second anodization step under similar

conditions, after which the pores were enlarged by etching in 5 wt% H_3PO_4 water based solution for 3 hours. AAM template with a pore size of 250-300 nm, and depth of 2-3 μm was fabricated.

2.3 Structure and morphology characterization methods

2.3.1 Fourier transform infrared analysis (FTIR)

Fourier transform infrared analysis is an important tool to reveal the structures of covalently bonded chemicals by producing an infrared absorption spectrum that is like a molecular "fingerprint." Molecular bonds vibrate at various frequencies depending on the elements and the type of bonds. For any given bond, there are several specific frequencies at which it can vibrate. According to quantum mechanics, these frequencies correspond to the ground state (lowest frequency) and several excited states (higher frequencies). One way to cause the frequency of a molecular vibration to increase is to excite the bond by having it absorb light energy. For any given transition between two states the light energy (determined by the wavelength) must exactly equal the difference in the energy between the two states [usually ground state (E_0) and the first excited state (E_1)]. The energy corresponding to these transitions between molecular vibrational states corresponds to the infrared portion of the electromagnetic spectrum.

The position and intensity of absorption bands of a substance are extremely specific

to that substance. The best-suited bands for the identification are those, which can be classified to the carbon backbone of the molecule. These kinds of absorption bands are frequently found in the easily accessible wavenumber range of about 1500 and 650 cm^{-1}, often called the "fingerprint region".

In this work, FTIR analysis was carried out to identify the crystalline phases of PVDF and P(VDF-TrFE) thin films and nanostructures, and to study the intermolecular bonds in the thin films. The FTIR spectra were collected by Spectrum 2000 (Perkin Elmer).

2.3.2 X-ray diffraction (XRD)

X-ray diffraction (XRD) is a non-destructive analytical technique to examine the long-range order in various crystalline materials. When a monochromatic X-ray beam with wavelength λ is projected onto a crystalline material at an angle θ, the path difference for X-rays reflected from adjacent planes with periodic d spacing is $2d\sin\theta$. As shown in Figure 2.3, according to Bragg's Law, diffraction occurs only when the distance traveled by the rays reflected from successive planes differs by a complete number n of wavelengths. Therefore,

$n\lambda = 2d\sin\theta$. (2.1)

$$n\lambda = 2d \sin\theta$$
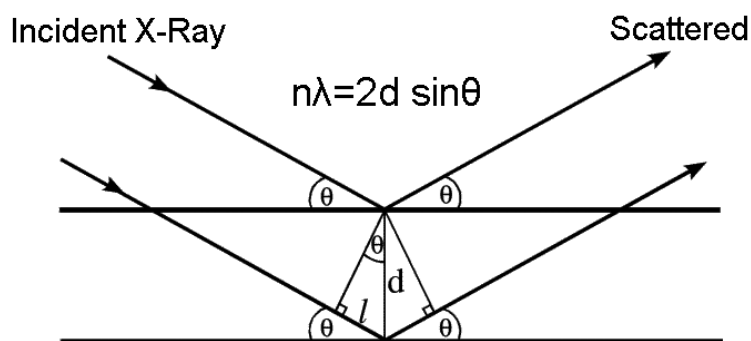
Figure 2.3 Diffraction of X-Rays by a crystal.

In this work, XRD studies were used to identify the crystalline phase and analyze the degree of crystallization of the polymer films. Throughout this study, XRD measurements were performed using an XRD system (D8-ADVANCE, Bruker AXS GmbH, Karlsruhe, Germany) and utilizing a wavelength of λ=1.542 Å (Cu-Kα).

2.3.3 Thermogravimetric Analysis (TGA)

Thermogravimetric Analysis (TGA) measures the amount and rate of change in the weight of a material as a function of temperature or time in a controlled atmosphere. Measurements are used primarily to determine the composition of materials and to predict their thermal stability at temperatures up to 1000°C. The technique can characterize materials that exhibit weight loss or gain due to decomposition, oxidation, or dehydration.

In this study, thermal analysis was performed to investigate the water loss of hydrated salts as well as the polymer films with the hydrated salts. The analysis was conducted

with SDT2960 simultaneous differential scanning calorimetry-thermal gravitational analysis (DSC-TGA, TA Instruments) at a scan rate of 20°C /min in an air atmosphere.

2.3.4 Scanning electron microscopy (SEM)

Scanning electron microscopy (SEM) is a type of electron microscopy techniques that images a sample by scanning it with a beam of electrons in a raster scan pattern. SEM permits observation and characterization of materials on a nanometer to micrometer scale. In SEM, an electron beam is thermionically emitted from an electron gun fitted with a tungsten filament cathode. The sample area to be examined is irradiated with the finely focused electron beam and various electrons and quanta emitted can be recorded be detectors. The types of signals produced from the interaction of the electron beam with the sample include secondary electrons, backscattered electrons, x-rays and other photons of various energies. The electrons interact with the atoms that make up the sample producing signals that contain information about the sample's surface topography, composition, and other properties such as electrical conductivity.

In this study, the surface and cross-section morphology of samples were examined by a field emission scanning electron microscope (JSM-6700F, JEOL).

2.3.5 Transmission electron microscopy (TEM)

Transmission electron microscopy (TEM) is a microscopy technique whereby a beam of electrons is transmitted through an ultra thin specimen, interacting with the specimen as it passes through. The beam energies are typically in the range from 100,000 to 400,000 eV. The interactions that occur during the collision of the electron beam and the sample produce the following: directly transmitted electrons, backscattered electrons, secondary electrons, coherent elastic scattered electrons, incoherent inelastic electrons, incoherent elastic forward scattered electrons, and continuum x-rays. The versatility of electron microscopy and x-ray microanalysis is derived in large measure from this variety of interactions that the beam electrons undergo in the specimen.

In this study, the morphology and structure of polymer nanotubes with silver coating were examined by a high-resolution transmission electron microscope (Philips CM300 FEGTEM)

2.4 Electrical characterization methods

2.4.1 Dielectric characterization

Dielectric characterization is crucial for structure and properties studies of ferroelectric materials. Under external electric field, the dielectric response of ferroelectric materials results from the short-range motion of charge carriers. This

separation of charges is called polarization. The dielectric constant is related to the polarization that can be achieved in the material. In this study, effective parallel capacitance and loss factor (C_p-D) measurement was done using Agilent 4194A impedance analyzer. The dielectric constant ε_r can be estimated from C_p by the relationship $C = (\varepsilon_r \varepsilon_o A)/d$.

2.4.2 Ferroelectric characterization

Ferroelectrics materials possess a spontaneous electric polarization that can be reversed by applying a suitable electric field. This process is known as polarization reversal and is always accompanied by hysteresis. A P-E hysteresis loop for a device is a plot of the charge or polarization (P) developed, against the field applied to that material (E) at a given frequency. For the hysteresis measurement, a ferroelectric thin film sample is put into a sandwich structure (top electrode/ferroelectric film/bottom electrode). If a bipolar, repetitive voltage signal is applied to a ferroelectric material, its hysteresis loop can be traced out and the charge in the circuit can be measured by the Sawyer-Tower circuit [10]. During the hysteresis testing, a voltage waveform is applied to the sample in a series of voltage steps. At each voltage step, the current induced in the sample by the voltage step is integrated and the integral value is captured and converted into polarization. The polarization is plotted against the applied voltage or electric field to get the ferroelectric P-E hysteresis loops.

In this study, the hysteresis characterizations of PVDF-based thin film and nanostructures were conducted with a standard ferroelectric testing unit (Precision Premier II, Radiant Technologies) connected with a high-voltage interface.

2.4.3 Piezoelectric characterization

2.4.3.1 Laser scanning vibrometer (LSV) system

The piezoelectric properties can be characterized either by measuring the induced charge under external mechanical stress through the direct piezoelectric effect, or by measuring the dilatation in response to the applied electric field due to the converse piezoelectric effect. For thin film samples on substrates, the piezoelectric characterizations are commonly conducted by methods using the converse piezoelectric effect, which reduce the errors caused by excess charges from bending effect.

In this study, a laser scanning vibrometer (LSV) system was employed for the piezoelectric characterization of the PVDF-based thin films and nanostructures. Yao et al. for the first time proposed the use of LSV to measure the piezoelectric coefficient [11, 12]. The LSV measurement for piezoelectric coefficient shows high reliability, high efficiency, and comprehensive information.

An LSV system (OFV-3001-SF6, PolyTech GmbH) consisting of mainly a vibrometer scanning head, a vibrometer controller, a junction box and a host computer was used. A function generator (HP33120A) was used to produce the driving signal, which was subsequently amplified by a high speed power amplifier (NF Electronic Instruments 4010). Sine signal of 5 KHz was applied with a peak-to-peak voltage of 1 V. The system was a modified Mach-Zehnder interferometer, and the vibration velocity and displacement were measured based on the Doppler shift and optical interference, which are briefly explained as follows.

When two coherent light beams are coincided, the resulting interference intensity I($\Delta\varphi$) varies with the phase difference between the two beams $\Delta\varphi$ according to:

$$I(\Delta\varphi) = \frac{1}{2} I_{max} (1 + \cos\Delta\varphi) \qquad (2.2)$$

The phase difference $\Delta\varphi$ is a function of the path difference ΔL between the two beams according to:

$$\Delta\varphi = \frac{2\pi\Delta L}{\lambda} \qquad (2.3)$$

in which λ is the wavelength.

If one of the two beams is scattered back from the moving surface of a sample (object beam), the path difference becomes a function of time ΔL(t). The interference fringe pattern moves on the detector, and the displacement of the object can be determined, accordingly.

The object beam is also subjected to a small Doppler frequency shift f_D on scattering from the moving surface, which is determined by the velocity V according to

$$f_D = \frac{2|V|}{\lambda} \qquad (2.4)$$

Thus, the velocity of the vibration of the sample can be measured by detecting and processing the Doppler shift information.

Before the piezoelectric testing, a circular scanning grid was defined, which covered both the top-electrodes and the surrounding films. A helium neon laser beam was pointed on to the surface of the samples with the aid of a microscope, and reflected back through the microscope objective towards the interferometric sensor. By scanning the defined grid points, an average measurement of either the displacement or the velocity of the whole surface could be obtained. By this way, the movement of the piezoelectric films and substrates can be observed simultaneously. In addition, an animation of the movement could be simulated, with the amplitude and the phase information for each of the grid points.

2.4.3.2 Piezoresponse force microscopy (PFM)

Atomic force microscopy (AFM), also known as scanning force microscopy (SFM), is one of a family of scanning probe microscopes which have became an important tools in materials research since their invention. These tools can reveal the details at the atomic and molecular level, thus increase the understanding of the underlying

mechanism of many phenomena and leading to new discoveries in many fields. The properties of a surface, such as topography, electrical properties, are revealed through the interaction between the scanning probe and the surface.

Piezoresponse force microscopy (PFM) is a variant of AFM that allows imaging and manipulation of ferroelectric domains. PFM is based on the converse piezoelectric effect, which is a linear coupling between the electrical and mechanical properties of a material. Since all ferroelectrics exhibit piezoelectricity, an electric field applied to a ferroelectric sample results in changes of its dimensions. In this study, the samples were imaged with a commercial vertical PFM (Model MFP-3D, Asylum Research, USA)

To detect the polarization orientation, an AFM tip is used to scan over the sample surface in Contact Constant Force Mode and apply certain voltage. The domains with polarization in the same direction as the electric field will extend, and the domains with opposite polarization will contract. A shear strain can also be produced in the sample in the case that the polarization is perpendicular to the electric field direction.

The AFM probe tip moving according to the surface displacement causes cantilever normal or torsion (because of friction) deflections. Direction of the deflection depends on the mutual orientations of the electric field and domain polarization.

Correspondingly in the case of the AC electric field, phase lag between the electric field and cantilever deflections will depend on the their mutual orientations. In general case, by analyzing the amplitudes and phases of the normal and torsion cantilever vibrations, one can reconstruct the sample domain structure.

2.4.3.3 Conductive atomic force microscopy (C-AFM)

Conductive atomic force microscopy (C-AFM) is a high precision techniques widely used nowadays to investigate the electrical properties of the samples (mainly focusing on the surface). Typically, a selectable voltage bias is applied between the sample and the conductive AFM tip with the tip being on virtual ground. The current passing through the sample is recorded using a linear amplifier as the tip is scanning the sample in contact mode. Hence, the sample's topography and current image are obtained simultaneously, enabling the direct correlation of a sample location with its electrical properties. In this study, the samples were measured with a commercially available Bruker Dimension Icon Scanning Probe Microscope (SPM).

References

[1]   J. H. Fendler and F. C. Meldrum, "THE COLLOID-CHEMICAL APPROACH TO NANOSTRUCTURED MATERIALS," Advanced Materials, vol. 7, pp. 607-632, Jul 1995.

[2]   G. B. Khomutov, A. Y. Obydenov, S. A. Yakovenko, E. S. Soldatov, A. S. Trifonov, V. V. Khanin, and S. P. Gubin, "Synthesis of nanoparticles in

Langmuir monolayer," Materials Science & Engineering C-Biomimetic and Supramolecular Systems, vol. 8-9, pp. 309-318, Dec 1999.

[3]   H. Kraack, B. M. Ocko, P. S. Pershan, E. Sloutskin, and M. Deutsch, "Structure of a Langmuir film on a liquid metal surface," Science, vol. 298, pp. 1404-1407, Nov 2002.

[4]   H. Masuda and K. Fukuda, "ORDERED METAL NANOHOLE ARRAYS MADE BY A 2-STEP REPLICATION OF HONEYCOMB STRUCTURES OF ANODIC ALUMINA," Science, vol. 268, pp. 1466-1468, Jun 1995.

[5]   K. Nielsch, J. Choi, K. Schwirn, R. B. Wehrspohn, and U. Gosele, "Self-ordering regimes of porous alumina: The 10% porosity rule," Nano Lett, vol. 2, pp. 677-680, Jul 2002.

[6]   A. P. Li, F. Muller, A. Birner, K. Nielsch, and U. Gosele, "Hexagonal pore arrays with a 50-420 nm interpore distance formed by self-organization in anodic alumina," Journal of Applied Physics, vol. 84, pp. 6023-6026, Dec 1998.

[7]   S. Ono, M. Saito, and H. Asoh, "Self-ordering of anodic porous alumina formed in organic acid electrolytes," Electrochimica Acta, vol. 51, pp. 827-833, Nov 2005.

[8]   V. P. Parkhutik and V. I. Shershulsky, "THEORETICAL MODELING OF POROUS OXIDE-GROWTH ON ALUMINUM," Journal of Physics D-Applied Physics, vol. 25, pp. 1258-1263, Aug 1992.

[9]   G. E. Thompson, R. C. Furneaux, G. C. Wood, J. A. Richardson, and J. S.

Goode, "NUCLEATION AND GROWTH OF POROUS ANODIC FILMS ON ALUMINUM," Nature, vol. 272, pp. 433-435, 1978.

[10]   H. Diamant, K. Drenck, and R. Pepinsky, "Bridge for accurate measurement of ferroelectric hysteresis," Review of scientific instruments, vol. 28, pp. 30-33, 1957.

[11]   K. Yao, S. Shannigrahi, and F. E. H. Tay, "Characterisation of piezoelectric thin films by areal laser scanning," Sensors and Actuators a-Physical, vol. 112, pp. 127-133, Apr 2004.

[12]   K. Yao and F. E. H. Tay, "Measurement of longitudinal piezoelectric coefficient of thin films by a laser-scanning vibrometer," Ieee Transactions on Ultrasonics Ferroelectrics and Frequency Control, vol. 50, pp. 113-116, Feb 2003.

Chapter 3   P(VDF-TrFE) ferroelectric nanotube array with double side electroless-plated silver as electrodes

3.1 Introduction

In recent years, there have been growing demands for high density capacitors for effective high-power energy storage applications. In comparison to inorganic materials, ferroelectric polymers have attracted considerable research interests due to their high electric breakdown field, low loss, light weight, flexible and non-toxic properties, making them promising dielectrics for high energy density capacitors [1-3]. The PVDF family, including P(VDF-TrFE) copolymer is one of the most technically important and extensively studied ferroelectric polymers due to its large piezoelectric coefficient, high dielectric constant, and low dielectric loss [4,5]. As a result of their excellent properties, P(VDF-TrFE) thin films have been used in various dielectric and ferroelectric device applications [6,7].

While ferroelectric thin films have been extensively studied in the past decades, one-dimensional nanostructures, such as nanobelts, nanowires and nanotubes based on inorganic [8-10] and organic [11-15] ferroelectrics, have attracted much interest in recent years due to their unique characteristics. Many applications including nanosensors, non-volatile memory and nanogenerators have been demonstrated [16-20]. Such nanostructures may also have great potential for high energy density

storage applications due to the dramatically increased surface areas over thin film

structure.

The large surface of dielectric nanotube structure can contribute to producing high

density dielectric capacitance if electrodes can be deposited on both the inner and

outer surfaces. However, this is a challenging work in consideration of the extremely

small diameter in nanometer level and the high aspect ratio of the nanotubes.

Furthermore, in previous reports on ferroelectric polymer nanotubes [12-15], the

nanotube structure is open at both ends, which is unsuitable for capacitor application

since the inner and outer electrodes may short at the open ends. Hence, there have

been few studies on the capacitance based on the approach of dielectric nanotubes;

Ni/P(VDF-TrFE) nanocables have been reported [15] with Ni nanowire as the inner

electrode that contacts P(VDF-TrFE) nanotube shells, and the nominal specific

capacitance of the nanocable array (10.8 pF/mm^2) was five times larger than the

value of P(VDF-TrFE) films (1.9 pF/mm^2) with similar thickness (50 μm). However,

the much greater potential of nanotubes for dielectric energy storage has not been

exhibited.

Hence, we designed and fabricated P(VDF-TrFE) nanotubes with one end sealed,

and another end open and linked to form a layer of nanotube array, using highly

ordered AAM as template. Electroless-plated Ag layers were deposited on both inner

and outer sides of the nanotubes as electrodes, which greatly enlarged the contact

area between the electrodes and the polymer dielectric. The sealed end prevented shorting between the two electrodes. This nanotube array layer comprising of the hollow nanotubes can be expected to have a much higher capacitance than the films with electrodes only on top and bottom surfaces. According to the theoretical calculation, the nanotube array with a layer thickness of 2 μm and a wall thickness of about 50 nm has 33 times larger surface area and 763 times larger capacitance when compared to a P(VDF-TrFE) film with a thickness of 2 μm. Experimentally, a 95 times larger capacitance was demonstrated.

3.2 Experimental

3.2.1 Fabrication of P(VDF-TrFE) nanotube array with double side silver layers

Figure 3.1 shows the schematic fabrication procedure of the P(VDF-TrFE) nanotube array in AAM template with Ag coatings on both sides as electrodes. One-end sealed AAM template (Figure 3.1(a), pore diameter of 250-300 nm, depth of 2 μm) supported on Al was fabricated using a two-step anodizing method. The AAM template was immersed in silver plating solution and sonicated continuously to form a uniform silver layer (Figure 3.1(b)). P(VDF-TrFE) solution was prepared at concentration of 10 wt% with the mixed solvent of dimethylformamide (DMF)/acetone. The P(VDF-TrFE) solution was deposited on the silver-coated AAM by spin coating followed by immediate heating at 250 °C for 1 minute. The

high surface energy of the Ag surface in the template allows the polymer melt to easily wet the Ag-coated template surface so as to form the desired nanostructure. As the polymer melt well conformed onto the template, one-end sealed P(VDF-TrFE) nanotube array was formed successfully. The deposition was repeated 20 cycles to increase the thickness of the nanotube walls (Figure 3.1(c)). To enhance the wetting and coating effect of silver plating solution inside the P(VDF-TrFE) nanotubes, a surface treatment with silane coupling agent 3-aminopropyl triethoxysilane (APTES) and vacuum condition were introduced. The template with P(VDF-TrFE) nanotube array was immersed in 5 wt% 3-aminopropyl triethoxysilane (APTES) ethanol solution for 1 hour in ultrasonic and dried to improve the hydrophilicity on inner surface of the P(VDF-TrFE) nanotube. The surface-treated nanotube sample was subsequently immersed in the silver plating solution and the container was pumped to vacuum. A silver layer was thus deposited on the inner surface of the nanotubes after the silver plating, as well as on top of the sample surface. (Figure 3.1(d)). The top silver layer was patterned by photolithography to serve as the top or inner electrodes (Figure 3.1(e)). At the edge of the sample, the polymer was removed by acetone to expose the bottom or outer electrode; silver epoxy was applied on the Ag-AAM surface to provide a good contact to the bottom electrode layer for testing (Figure 3.1(f)). To observe and study the nanotube array released from the template, the AAM template was etched off in 4 mol/L NaOH solution.
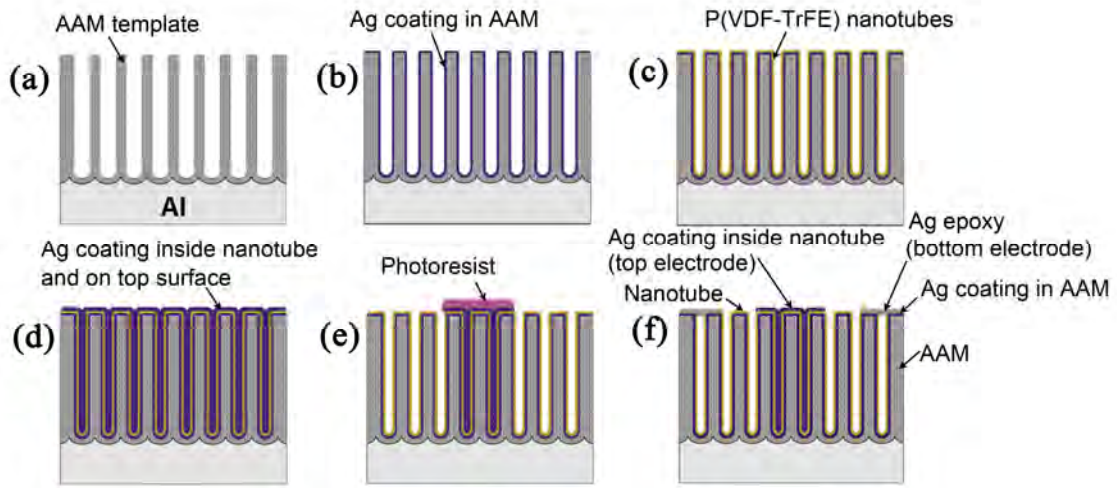
Figure 3.1 Schematic illustration of the fabrication process: (a) empty AAM template; (b) AAM template coated with silver layer; (c) P(VDF-TrFE) nanotube array in silver-coated AAM; (d) P(VDF-TrFE) nanotube array with inner silver coating and silver layer on top; (e) photolithography patterning of top silver layer; (f) P(VDF-TrFE) nanotube array in AAM template with top and bottom electrodes for electrical testing.

3.2.2 Characterization of P(VDF-TrFE) nanotube with double side silver layers

The morphology of AAM template and P(VDF-TrFE) nanostructures was observed with field emission scanning electron microscopy (FESEM, JSM-6700F, JEOL) and high-resolution transmission electron microscope (Philips CM300 FEGTEM). The crystalline structures were examined with x-ray diffraction (XRD) system (D8-ADVANCE, Bruker AXS GmbH, Karlsruhe). The capacitance of the nanotube array was measured with a precision impedance analyzer (Agilent 4294A).

3.3 Results and discussion

3.3.1 Temperature effect on the silver layers deposited on AAM template by electroless plating

In this work, electroless plating method was used to deposit conductive silver layers into the AAM template and the inner surface of the P(VDF-TrFE) nanotubes as the bottom and top electrodes for electrical testing. It was found that temperature is a critical factor determining the silver deposition rate, and also has a significant effect on the morphology of the resulting silver layer. Therefore, the deposition temperature effect on silver electroless plating and wetting behavior of silver plating solution to AAM template and nanotube inner surface were studied by both theoretical and experimental approaches.

The silver electroless plating reaction is expressed as below:

$$RCHO + 2[Ag(NH_3)_2]^+ + 2OH^- \xrightarrow{k} RCOOH + 2Ag\downarrow + 4NH_3 + H_2O \quad (3.1)$$

The temperature effect on the reaction rate can be calculated using Arrhenius equation:

$$k = A\,e^{-Ea/RT} \quad (3.2)$$

where k is the reaction rate, A is a constant depending on the reaction, Ea is the activation energy, R is the gas constant, T is the reaction temperature.

According to Equation 3.2, the effect of temperature on reaction rate k can be calculated using Eq. 3.3 when the temperature is changed from T_1 to T_2.

$$\ln\left(\frac{k_2}{k_1}\right) = \left(\frac{Ea}{R}\right) * \left(\frac{1}{T_1} - \frac{1}{T_2}\right) \quad (3.3)$$

In this equation, R=8.314 J·mol^{-1}·K^{-1}; For the silver electroless plating reaction, Ea=57 kJ·mol^{-1}.

The silver electroless plating process was carried out at three different temperatures: 0 °C, 20 °C, and 50 °C. The change in relative reaction rate was calculated using Eq 5.3 and listed in Table 3.1.

Table 3.1 Relative reaction rate of silver electroless plating process at different temperatures

Temperature (K)	Relative reaction rate
273	k_0
293	$k_1/k_0 = 5.54$
323	$k_2/k_1 = 8.79$

According to the calculation, the reaction rate increases 5.54 times when the temperature increases from 0 °C to 20 °C and another 8.79 times from 20 °C to 50 °C. At a slightly elevated temperature, much more rapid deposition of silver may lead to large particle size and rough surface of the silver layer，which is not desirable as electrodes for the nanotubes. On the other hand, at a low temperature, it will take too much time to deposit a continuous silver layer due to the very low deposition rate.

Figure 3.2 shows the SEM images of silver layer on AAM surface deposited at different temperatures, which confirmed the critical temperature effect on the silver deposition rate and resulting morphology. Figure 3.2(a) shows the AAM template before the silver plating. As shown in Figure 3.2(b), the deposition at 0°C after 25 minutes could not form a continuous silver layer due to the slow deposition rate. At 20°C, a continuous silver layer with a thickness of tens of nanometer was formed on

the surface, as shown in Figure 3.2(c). The surface of silver layer deposited at 50 $^{\circ}$C

was relatively rough due to the further improved deposition rate, as shown in Figure

3.2(d). In this work, the deposition temperature is controlled at 20 $^{\circ}$C for a suitable

deposition rate as well as a relative smooth morphology of the obtained silver layer.
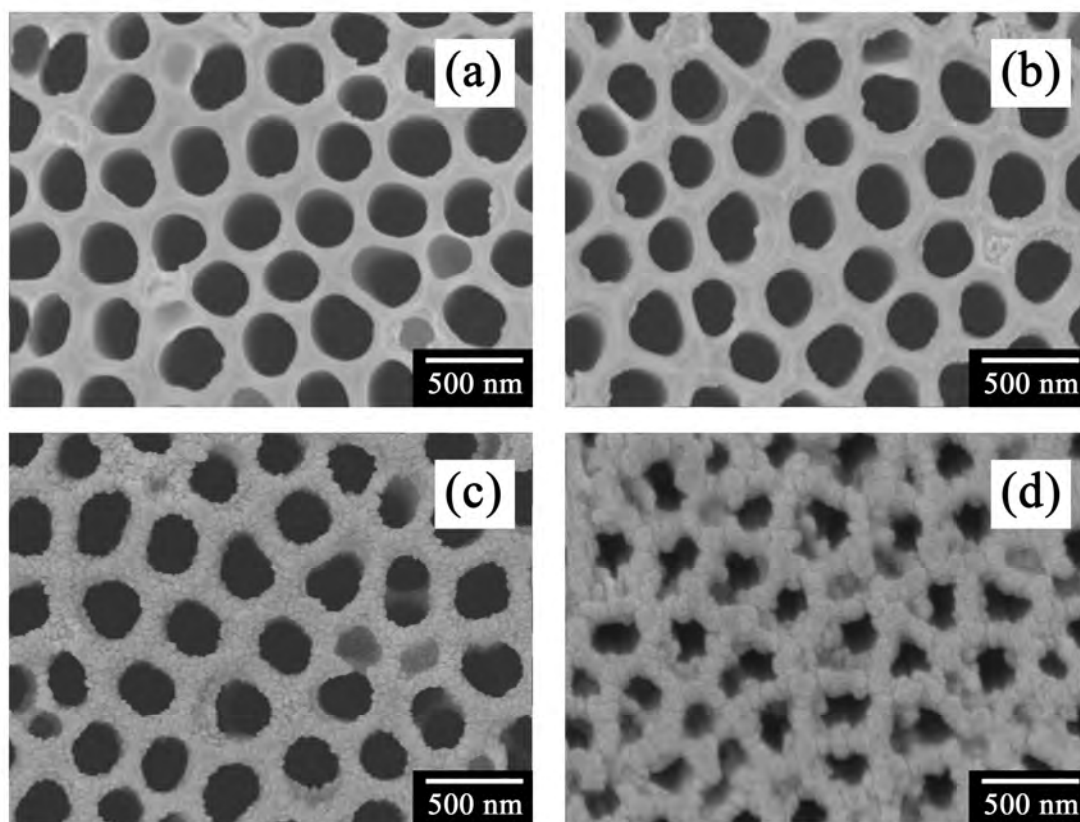
Figure 3.2 SEM images of (a) bare AAM template, and AAM with electroless deposited silver at (b) 0 $^{\circ}$C (c) 20 $^{\circ}$C (d) 50 $^{\circ}$C for 25 minutes.

3.3.2 Fabrication and characterization of P(VDF-TrFE) nanotube in silver-coated AAM template

Figure 3.3 shows the silver-coated AAM template and the P(VDF-TrFE) nanotube

array fabricated using the template. As can be seen in Figure 3.3(a), a continuous Ag

layer of 30-40 nm thickness (estimated from Figure 3.2) has been successfully

deposited in AAM template by the electroless plating method. As discussed in the previous section, the deposition temperature is controlled at $20^{o}C$ for a suitable deposition rate as well as a relative smooth morphology of the obtained silver layer.

Figure 3.3(b) shows the open ends of the nanotubes formed in the template after the deposition of 20 cycles. The thickness of the P(VDF-TrFE) nanotubes reached about 50 nm after 20-cycle coating. Figures 3.3(c) and 3.3(d) show the side view and top view, respectively, of the released nanotubes with the continuous outer silver coating. It can be seen from the SEM images that the nanotubes are sealed at one end and linked in the open end. The silver layers may have enhanced the stiffness of the relatively soft nanotube structure, allowing the nanotubes to be free-standing. As can be seen in the SEM images, after the dedicated control of the surface wetting, flowing behavior of polymer melt, and the experimental condition, the desired polymer nanotube structure was achieved.
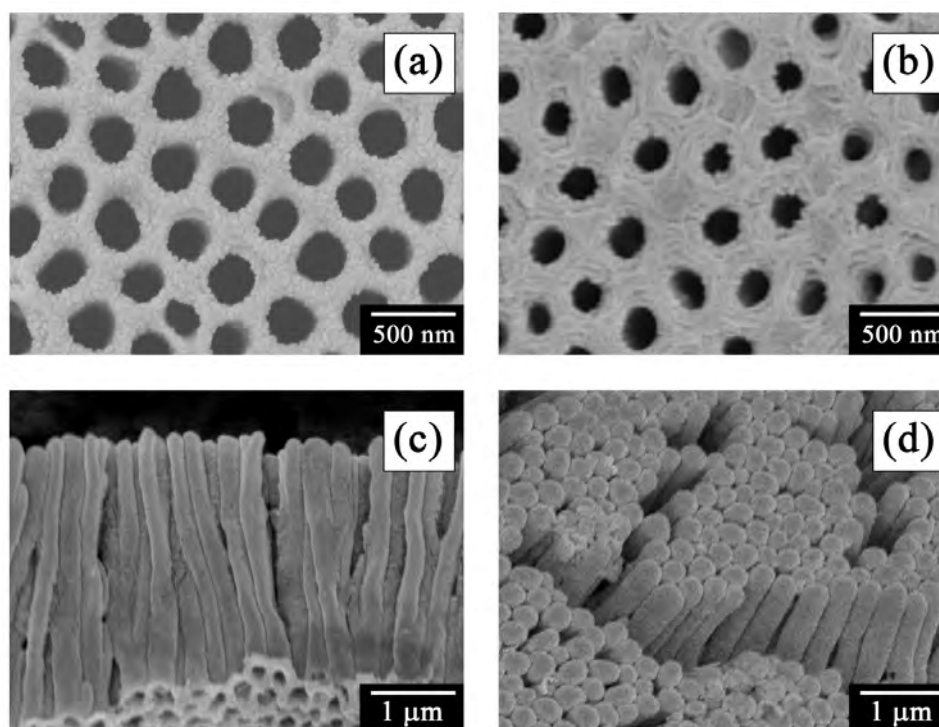
Figure 3.3 SEM images of (a) silver coated AAM; (b) Ag-AAM template with P(VDF-TrFE) layer after 20-cycle spin-coating; (c) released P(VDF-TrFE) nanotube with outer silver layer, side view; (d) released P(VDF-TrFE) nanotube with outer silver layer, top view.

It was observed that when the temperature is slightly above the melting point of the polymer, the melt is relatively viscous, and the cylindrical nanopores, which can be regarded as nanosized capillaries, are gradually filled with polymer melt via capillary force to form nanorods instead nanotubes. As the temperature increases, the polymer melt becomes less viscous with lower surface tension, and the wetting behavior will shift from partial wetting to complete wetting when the temperature has reached a critical point known as the wetting transition temperature (T_w) [22]. In the complete wetting regime, the polymer melt spontaneously spreads on the inner walls of the nanopores in Ag-coated alumina membranes and forms the nanotube structure. Hence, higher temperature is preferred for the fabrication of nanotube structure, but should be lower than the polymer decomposition temperature.

In this work, 250 ºC, which was well above the melting point but below the decomposition of P(VDF-TrFE) polymer, was chosen as the processing temperature. The surface energy of the silver-coated AAM template [23] is about 800×10^{-3} N/m, while the surface energy of P(VDF-TrFE) melt at 250 ºC is 20×10^{-3} N/m. The high surface energy of Ag-AAM ensured that it is in complete wetting regime at 250 ºC. The driving force p is theoretically calculated to predict the wetting behavior of polymer melt in the silver-coated AAM nanopores.

The wetting driving force p can be calculated using Laplace equation:

p= 2γ_{12}cosθ /R   (3.4)

where γ_{12} is the interfacial tension between liquid and solid, θ is the contact angle (θ = 0 representing the complete wetting region), and R is the radius of the capillary. The interfacial tension γ_{12} of P(VDF-TrFE) melt and Ag-AAM surface is calculated using Girifalco-Good equation [24]:

$$\gamma_{12} = \gamma_1 + \gamma_2 - 2\phi\left(\gamma_1\gamma_2\right)^{1/2} \quad (3.5)$$

where γ_1 is the surface tension of liquid (P(VDF-TrFE) melt, 20×10^{-3} N/m) and γ_2 is the surface energy of solid (Ag-AAM template, 800×10^{-3} N/m), and ϕ is the Girifalco-Good's interaction parameter determined by the equation [24]:

$$\phi = \frac{\gamma_1\left(1+\cos\theta\right)}{2\left(\gamma_1\gamma_2\right)^{1/2}} \quad (3.6)$$

For the template with nanopore diameter of about 250 nm, the driving force calculated is about 12.47 MPa. Base on the above calculation, capillary effect is

sufficient to drive P(VDF-TrFE) polymer melt to spontaneously wet the template and form the nanotubes on the surface of Ag.

XRD was used to examine the crystalline phase of the obtained P(VDF-TrFE) nanotubes. Figure 3.4(a) shows the P(VDF-TrFE) β phase peak, which proves that the P(VDF-TrFE) nanotube array is the desired ferroelectric β phase. This result also indicates that the processing temperature of 250 ^{o}C does not adversely affect the crystalline phase of the polymer.
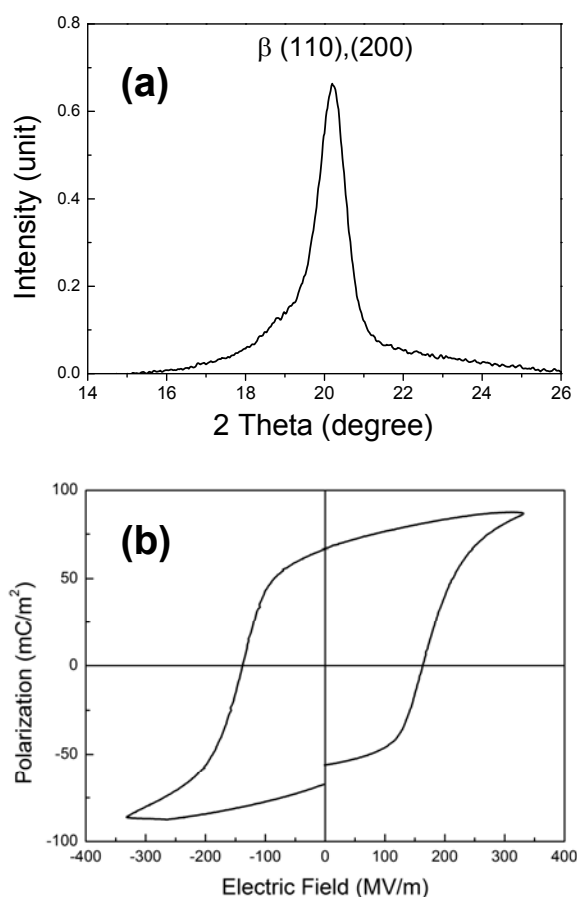
Figure 3.4 (a). XRD spectrum of released P(VDF-TrFE) nanotube array; (b) Polarization – electric field (P-E) hysteresis loop of a P(VDF-TrFE) nanotube sample.

Ferroelectric characterization was performed on a P(VDF-TrFE) nanotube sample with top-bottom electrodes instead of electrodes on the inner and outer nanotube surfaces. In such a configuration, the electric field was applied across the length (~2 μm) of the nanotube. A typical polarization – electric field (P-E) hysteresis loop is shown in Figure 3.4(b). The remnant polarization P_r of 66.3 mC/m^2 is slightly inferior to the previously reported value of 83.5 mC/m^2 for a P(VDF-TrFE) thin film. However, this is to be expected, since the hollow property of the nanotube implies that the actual polymer cross sectional area is smaller than the electrode area used to calculate the P_r. Hence, this result is an indication of the good ferroelectric property of the P(VDF-TrFE) nanotubes. On the other hand, the coercive field E_c is 164 MV/m, which is significantly higher than the thin film value of 68 MV/m. This may be attributed to the unique polymer chain orientation of the nanotubes.

3.3.3 Capacitance of P(VDF-TrFE) nanotube with double sides silver coatings: theoretical calculation and experimental results

As observed by SEM, the wall thickness of the P(VDF-TrFE) nanotube is about 50 nm. The outer diameter of the nanotubes is about 250 nm, and the length is about 2 μm. It can be calculated from the above data that the nanotube array layer has 33 times larger surface area than thin film.

One single P(VDF-TrFE) nanotube with double side silver coating can be treated as a cylindrical capacitor, and the capacitance can be calculated by the equation:

$$C = \frac{2\pi\varepsilon_0\varepsilon_r L}{\ln(r_2 / r_1)} \quad (5.7)$$

where the vacuum dielectric permittivity ε_0= 8.854$\times 10^{-12}$ F/m, the relative dielectric

constant of P(VDF-TrFE) ε_r= 11, the length of nanotube L= 2 μm, the inner radius

of nanotube r_1= 75 nm, and the outer radius r_2= 125 nm. The capacitance of one

single P(VDF-TrFE) nanotube is calculated to be 2.39×10^{-3} pF. The nominal

specific capacitance (defined as capacitance divided by top electrode area) is then

calculated, after considering that a top electrode covered about 1.37×10^7 nanotubes

per square millimeter. Hence, the theoretically calculated nominal specific

capacitance of the nanotube sample is about 3.38×10^4 pF/mm^2, while the

capacitance of a 2-μm thick P(VDF-TrFE) film is 44.3 pF/mm^2. Hence the

capacitance of P(VDF-TrFE) nanotube array with double side silver coating is 763

times larger compared with 2-μm thick P(VDF-TrFE) film due to the enlarged

surface area and nanoscaled wall thickness.

Inner electrode need be deposited in P(VDF-TrFE) nanotubes for capacitance

measurement. When it was deposited under the same conditions as the outer

electrode deposition, the measured capacitance was 250-300 pF/mm^2, which was

only 1 % of the calculated result. This is due to the incomplete deposition of the

inner electrode, which is caused by the incomplete wetting of silver plating solution

inside P(VDF-TrFE) nanotubes. The silver plating on AAM is relatively easy

because the silver plating solution can spontaneously wet AAM template and form a

continuous layer due to the high surface energy of AAM (450×10^{-3} N/m). However,

the surface energy of P(VDF-TrFE) is much lower (36.5×10^{-3} N/m), making it

difficult for the silver plating solution to wet the inner surface of nanotube. In this work, water/ethanol (1:9 in volume) -based silver plating solution was used to lower the surface tension, but the deposition of inner silver layer was still incomplete according to TEM graphs (Figure 3.5(a)). Vacuum was introduced to remove the air trapped inside the nanotubes so as to enhance the wetting behavior of silver plating solution. The capacitance was slightly improved to about 1.12×10^3 pF/mm^2, which was only 3 % of the calculated value.

To further improve the wetting of silver plating solution inside the P(VDF-TrFE) nanotubes, the inner surface of the P(VDF-TrFE) nanotubes was treated with 5 wt% 3-aminopropyl triethoxysilane (APTES) ethanol solution, in which the amino groups can bond with the fluorine atoms in P(VDF-TrFE) polymer chain to improve the surface hydrophilicity [25]. After the surface treatment, the P(VDF-TrFE) nanotube array was immersed in silver plating solution under vacuum condition.

In contrast to the incomplete silver layer inside the nanotubes without APTES surface modification or vacuum condition (Figure 3.5(a)), Figure 3.5(b) shows the complete inner silver coating in nanotube after those treatments. Only silver layers are visible in black in Figure 3.5(b), and the polymer is almost invisible. Figure 3.5(c) shows an SEM image for the cross section of the nanotubes along the axial direction with inner silver coating. Figure 3.5(d) presents a radial cross-sectional TEM image of the P(VDF-TrFE) nanotubes with only outer silver layer, in which the silver

layers appear as silver rings as expected. A radial cross-sectional TEM image for the P(VDF-TrFE) nanotubes with the double side silver layers are shown in Figure 3.5(e), in which silver particles inside the nanotubes can be observed, and one set of double outer and inner silver rings spaced by the nanotubes is indicated. Although the inner surface of the nanotubes was covered by silver particles, the coating inside P(VDF-TrFE) nanotubes was relatively rough, as the silver particles had a tendency to aggregate inside the nanotubes.
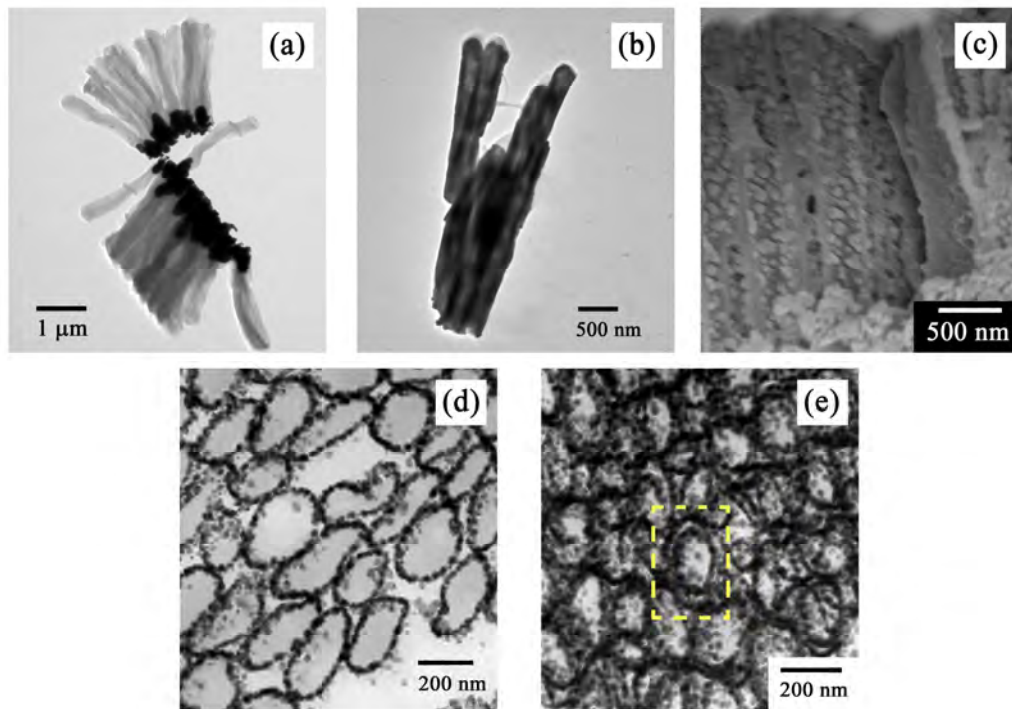
Figure 3.5 (a) TEM image of P(VDF-TrFE) nanotubes with incomplete inner silver layers; (b) TEM image of nanotubes with complete inner silver layers after introducing APTES treatment and vacuum condition; (c) SEM image of P(VDF-TrFE) nanotube with inner silver layer, axial cross-section view; (d) TEM radial cross-section image of P(VDF-TrFE) nanotubes with only outer silver layer; (e) TEM radial cross-section image of P(VDF-TrFE) nanotubes with both inner and outer silver layers.

Table 3.2 shows the theoretically calculated and measured nominal specific capacitance of P(VDF-TrFE) nanotube array layer with double side silver coating achieved by introducing surface treatment with APTES and vacuum condition. The

nominal specific capacitance of P(VDF-TrFE) film is also given for comparison. The

measured capacitance, 4.23×10^3 pF/mm^2, was improved to 12.5% of the

theoretically calculated value, indicating that the APTES treatment has enhanced the

coverage of the inner silver electrode. Our result here is a significant improvement

over previously reported values Ni/P(VDF-TrFE) nanocables (10.9 pF/mm^2).

Nevertheless, the measured capacitance is still only a fraction of the theoretically

calculated result of 3.38×10^4 pF/mm^2. The smaller value of the experimentally

obtained capacitance could be due to the aggregation of silver inside the nanotubes

and thus the smaller conductive electrode coverage over the inner surface of the

polymer nanotubes. Nevertheless, the capacitance of P(VDF-TrFE) nanotube array

was still 95 times higher than the 2-μm-thick film, and can be further increased by

improving the quality of the inner Ag electrode coating.

Table 3.2 Theoretically calculated and experimentally measured specific capacitance of P(VDF-TrFE) nanotube array layer, in comparison with P(VDF-TrFE) film

Configuration	Dimension	Nominal specific capacitance (pF/mm^2)
Film (calculated)	2-μm thick	44.3
Nanotube array layer (calculated)	2-μm thick 50 nm-thick wall	3.38×10^4
Nanotube array layer (measured)	2-μm thick 50 nm-thick wall	4.23×10^3 (100 Hz)

3.4 Conclusions

In summary, P(VDF-TrFE) ferroelectric nanotubes sealed at one end and linked at the open end were fabricated using anodized alumina membrane (AAM) as template, and silver layers were deposited on both inner and outer sides of the nanotubes by electroless plating method. The P(VDF-TrFE) nanotubes were about 250 nm in outer diameter, 50 nm in wall thickness with about 40 nm thick silver layer on both sides. Surface treatment with coupling agent APTES and vacuum condition were introduced to enhance the wetting behavior of silver plating solution inside P(VDF-TrFE) nanotube to form inner silver layer. Compared with P(VDF-TrFE) film with similar overall thickness of 2 μm, the layer of the nanotube array has 33 times larger surface area and 763 times larger capacitance according to the theoretical calculations, and experimentally a 95 times larger capacitance has been demonstrated with the obtained nanotube arrays. The results have shown that the ferroelectric polymer nanotubes with the double side electrode coatings are promising for realizing high density capacitance and high power dielectric energy storage.

References

[1]   M. Rahimabady, S. T. Chen, K. Yao, F. E. H. Tay, and L. Lu, "High electric breakdown strength and energy density in vinylidene fluoride oligomer/poly(vinylidene fluoride) blend thin films," *Applied Physics Letters,* vol. 99, Oct 2011.

[2]   K. Yao, S. T. Chen, M. Rahimabady, M. S. Mirshekarloo, S. H. Yu, F. E. H. Tay, T. Sritharan, and L. Lu, "Nonlinear Dielectric Thin Films for High-Power Electric Storage With Energy Density Comparable With Electrochemical Supercapacitors," *Ieee Transactions on Ultrasonics Ferroelectrics and Frequency Control,* vol. 58, pp. 1968-1974, Sep 2011.

[3]   M. Rahimabady, K. Yao, S. Arabnejad, L. Lu, V. P. W. Shim, and D. C. W. Chet, "Intermolecular interactions and high dielectric energy storage density in poly(vinylidene fluoride-hexafluoropropylene)/poly(vinylidene fluoride) blend thin films," *Applied Physics Letters,* vol. 100, Jun 18 2012.

[4]   J. F. Legrand, "STRUCTURE AND FERROELECTRIC PROPERTIES OF P(VDF-TRFE) COPOLYMERS," *Ferroelectrics,* vol. 91, pp. 303-317, 1989.

[5]   H. Ohigashi, K. Koga, M. Suzuki, T. Nakanishi, K. Kimura, and N. Hashimoto, "PIEZOELECTRIC AND FERROELECTRIC PROPERTIES OF P (VDF-TrFE) COPOLYMERS AND THEIR APPLICATION TO ULTRASONIC TRANSDUCERS," *Ferroelectrics,* vol. 60, pp. 263-276, 1984.

[6]   S. Ducharme, T. J. Reece, C. M. Othon, and R. K. Rannow, "Ferroelectric polymer Langmuir-Blodgett films for nonvolatile memory applications," *Ieee Transactions on Device and Materials Reliability,* vol. 5, pp. 720-735, Dec 2005.

[7]   C. Y. Li, P. M. Wu, S. Lee, A. Gorton, M. J. Schulz, and C. H. Ahn, "Flexible dome and bump shape piezoelectric tactile sensors using PVDF-TrFE

copolymer," *Journal of Microelectromechanical Systems,* vol. 17, pp. 334-341, Apr 2008.

[8]   X. Y. Kong and Z. L. Wang, "Spontaneous polarization-induced nanohelixes, nanosprings, and nanorings of piezoelectric nanobelts," *Nano Lett,* vol. 3, pp. 1625-1631, Dec 2003.

[9]   Y. K. Tseng, C. J. Huang, H. M. Cheng, I. N. Lin, K. S. Liu, and I. C. Chen, "Characterization and field-emission properties of needle-like zinc oxide nanowires grown vertically on conductive zinc oxide films," *Advanced Functional Materials,* vol. 13, pp. 811-814, Oct 2003.

[10]   H. J. Fan, P. Werner, and M. Zacharias, "Semiconductor nanowires: from self-organization to patterned growth," *Small,* vol. 2, pp. 700-717, Jun 2006.

[11]   M. C. Garcia-Gutierrez, A. Linares, J. J. Hernandez, D. R. Rueda, T. A. Ezquerra, P. Poza, and R. J. Davies, "Confinement-Induced One-Dimensional Ferroelectric Polymer Arrays," *Nano Lett,* vol. 10, pp. 1472-1476, Apr 2010.

[12]   S. T. Lau, R. K. Zheng, H. L. W. Chan, and C. L. Choy, "Preparation and characterization of poly(vinylidene fluoride–trifluoroethylene) copolymer nanowires and nanotubes," *Materials Letters,* vol. 60, pp. 2357-2361, 2006.

[13]   R. K. Zheng, Y. Yang, Y. Wang, J. Wang, H. L. Chan, C. L. Choy, C. G. Jin, and X. G. Li, "A simple and convenient route to prepare poly(vinylidene fluoride trifluoroethylene) copolymer nanowires and nanotubes," *Chem Commun (Camb),* pp. 1447-1449, Mar 21 2005.

[14]   J. Huang and T. Kunitake, "Nanotubings of titania/polymer composite:

template synthesis and nanoparticle inclusion," *Journal of Materials Chemistry,* vol. 16, p. 4257, 2006.

[15]   C.-L. Sun, K. H. Lam, C. Chao, S. T. Lau, H. L. W. Chan, S. Guo, and X. Zhao, "Fabrication and characterization of Ni / P(VDF-TrFE) nanoscaled coaxial cables," *Applied Physics Letters,* vol. 90, p. 253107, 2007.

[16]   X. D. Wang, J. H. Song, J. Liu, and Z. L. Wang, "Direct-current nanogenerator driven by ultrasonic waves," *Science,* vol. 316, pp. 102-105, Apr 2007.

[17]   Z. L. Wang, "Piezoelectric nanostructures: From growth phenomena to electric nanogenerators," *Mrs Bulletin,* vol. 32, pp. 109-116, Feb 2007.

[18]   Z. J. Hu, M. W. Tian, B. Nysten, and A. M. Jonas, "Regular arrays of highly ordered ferroelectric polymer nanostructures for non-volatile low-voltage memories," *Nature Materials,* vol. 8, pp. 62-67, Jan 2009.

[19]   S. Cha, S. M. Kim, H. Kim, J. Ku, J. I. Sohn, Y. J. Park, B. G. Song, M. H. Jung, E. K. Lee, B. L. Choi, J. J. Park, Z. L. Wang, J. M. Kim, and K. Kim, "Porous PVDF as effective sonic wave driven nanogenerators," *Nano Lett,* vol. 11, pp. 5142-7, Dec 14 2011.

[20]   B. J. Hansen, Y. Liu, R. S. Yang, and Z. L. Wang, "Hybrid Nanogenerator for Concurrently Harvesting Biomechanical and Biochemical Energy," *Acs Nano,* vol. 4, pp. 3647-3652, Jul 2010.

[21]   Y. Li, M. Zheng, L. Ma, and W. Shen, "Fabrication of highly ordered nanoporous alumina films by stable high-field anodization," *Nanotechnology,*

vol. 17, pp. 5101-5105, Oct 28 2006.

[22]   M. F. Zhang, P. Dobriyal, J. T. Chen, T. P. Russell, J. Olmo, and A. Merry, "Wetting transition in cylindrical alumina nanopores with polymer melts," *Nano Lett,* vol. 6, pp. 1075-1079, May 2006.

[23]   S. F. Chernov, Y. V. Fedorov, and V. N. Zakharov, "SURFACE-TENSION OF SILVER IN DIFFERENT MEDIA," *Journal of Physics and Chemistry of Solids,* vol. 54, pp. 963-966, Aug 1993.

[24]   L. A. Girifalco and R. J. Good, "A THEORY FOR THE ESTIMATION OF SURFACE AND INTERFACIAL ENERGIES .1. DERIVATION AND APPLICATION TO INTERFACIAL TENSION," *Journal of Physical Chemistry,* vol. 61, pp. 904-909, 1957.

[25]   Z. M. Dang, H. Y. Wang, and H. P. Xu, "Influence of silane coupling agent on morphology and dielectric property in BaTiO3/polyvinylidene fluoride composites," *Applied Physics Letters,* vol. 89, Sep 2006.

Chapter 4 Piezoelectric polymer nanotube array for mechanical energy harvesting

4.1 Introduction

The use of piezoelectric materials to harvest mechanical energy from the environment has been studied for many years [1,2]. A major application of such energy harvesters is to provide a source of autonomous power for wireless sensors in remote locations where continuous battery replacement is impractical [1]; another possible application is for outdoor charging of portable and wearable electronics [2]. Recently, with the advent of nanotechnology and the emergence of nanoscale wireless devices, there is a corresponding need for energy harvesters to shrink to similar nanoscale dimensions. This is the motivation for the pioneering work by Wang and co-workers to investigate zinc oxide (ZnO) nanowire arrays as piezoelectric nanogenerators [3].

In their initial study, Wang *et al.* used a conducting atomic force microscope (AFM) tip to probe the piezoelectric response of ZnO nanowires under mechanical deformation by the AFM tip [3]. This was quickly followed by several demonstrations of packaged ZnO-based nanogenerator devices [4-8], with output voltages as high as 58 volts [8]. Other piezoelectric materials that have been demonstrated as nanowire- or nanorod- based generators include the wurtzites CdS [9] and GaN [10], as well as the perovskites $BaTiO_3$ [11], $Pb(Zr_{(1-x)}Ti_x)O_3$ (PZT) [12],

and PMN-PT [13]. Besides the obvious advantage of nanoscale miniaturization, nanowires can more effectively confine strain in the axial direction, hence they are desirable structures for piezoelectric generator applications.

Mechanical energy harvesting based on nano-porous [14] and electrospun [15] ferroelectric PVDF and P(VDF-TrFE) composite [16] have also been demonstrated. Ferroelectric polymers have many properties that make them attractive for energy harvesting applications. One advantage is their ease of preparation, since they can be processed from solution at low temperature and hence deposited at low cost. They also exhibit excellent piezoelectric properties; PVDF has a piezoelectric voltage constant g_{33} of 0.33 Vm/N [1], which is significantly superior to the values for ZnO (0.01 Vm/N) [17] and even PZT (0.02-0.03 Vm/N) [1]. Another important consideration is that the organic polymers are much more flexible and deformable than the inorganic ceramics; PVDF for instance has a Young's modulus of only 2.2 GPa [18], in contrast to 140 GPa for ZnO [19] and 54-63 GPa for PZT [20]. Hence, the polymers will be substantially more suited for applications whereby large mechanical deformations are expected, desired, or required. Mechanical properties also determine the resonant frequency, since for two materials of similar dimensions the resonant frequency ω is proportional to the square root of the Young's modulus Y (ie. $\omega^2 \propto Y$) [21]. Hence, polymer nanowires can be expected to have lower resonance frequencies compared to inorganic ceramic nanowires of similar sizes, which better matches the low frequency vibrations in most energy harvesting

applications.

In this chapter, we analyse and demonstrate for the first time mechanical energy harvesting from P(VDF-TrFE) nanotube array. Intuitively, it may be expected that the hollow nanotube structure is more deformable and hence more attractive than the solid nanorod for energy harvesting applications. In fact, the theoretical simulations show that under a constant applied force, nanotubes have higher energy harvesting capacity compared to nanorods of similar dimensions. The nanotube arrays in this work are fabricated by a template approach using anodized alumina membrane (AAM), and their current generation under mechanical deformation is characterized with a conducting AFM tip. A systematic study is undertaken to investigate how poling influences the current output. Non-polar α-phase PVDF nanotubes are also fabricated as control.

4.2 Experimental

4.2.1 Fabrication of PVDF/P(VDF-TrFE) nanotube array in AAM template

AAM template with a pore size of 250-300 nm, and depth of 2-3 μm was fabricated using a two-step anodizing method. P(VDF-TrFE) (72/28) was deposited from solution, which was prepared at concentration of 10 wt% with the solvent mixture of dimethylformamide (DMF)/acetone (1:1 by volume). Nanotubes were fabricated by a hot-press method described as follows. The P(VDF-TrFE) solution was drop-casted on the AAM template surface and dried at 80 ºC. The AAM with the

polymer layer was then heated to 250 ºC, which is above the polymer melting point, and pressure was applied to drive the polymer into the template pores. This causes the polymer to melt and wet the AAM surface, thus duplicating the template morphology and forming the desired nanotube structure. Control samples of PVDF nanotubes were also fabricated by the similar hot-press method as described above. The AAM template was then etched away in 4 mol/L NaOH solution to release the nanotubes. The bottom side of the released nanotube array was attached on gold-coated Si substrate with conducting silver epoxy for support, while 200-μm-diameter circular gold electrodes were sputtered and patterned on the top side. Figure 4.1 shows the schematic fabrication procedure of the P(VDF-TrFE) nanotube array with top and bottom Au electrodes.
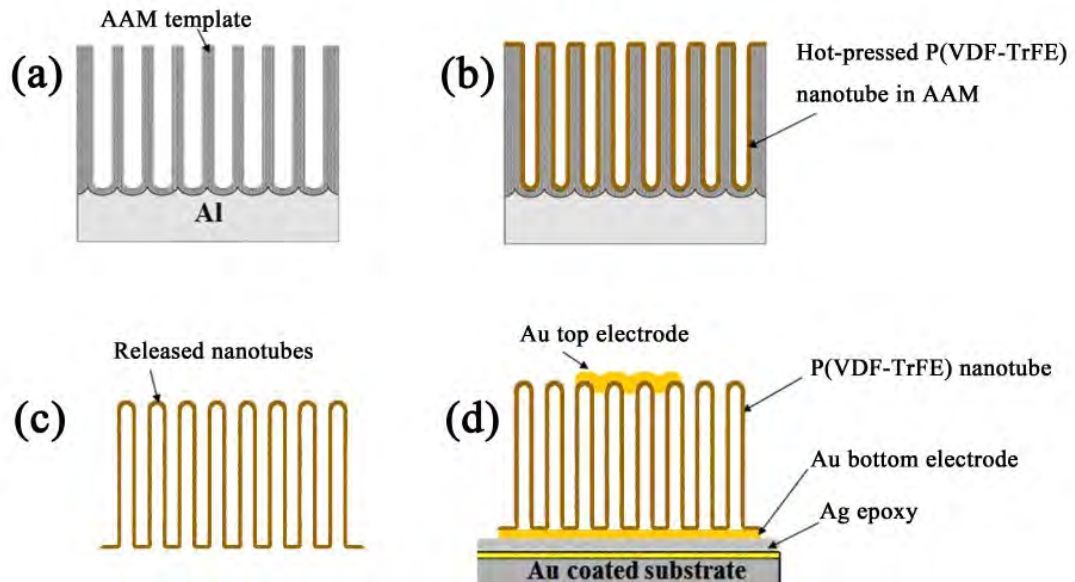
Figure 4.1 Schematic illustration of the fabrication process: (a) empty AAM template; (b) Hot-pressed P(VDF-TrFE) nanotube array in AAM; (c) Released P(VDF-TrFE) nanotube array; (d) P(VDF-TrFE) nanotube array with top and bottom electrodes.

4.2.2 Characterization of polymer nanotube array

The morphology of the AAM template and the polymer nanotube array was observed with field emission scanning electron microscopy (FESEM, JSM-6700F, JEOL). The released nanotubes were also examined with high-resolution transmission electron microscopy (Philips CM300 FEGTEM). The crystalline structures of the polymer nanotubes were examined with X-ray diffraction (XRD) (D8-ADVANCE, Bruker AXS GmbH, Karlsruhe). The polarization and electric field (P−E) hysteresis loops were measured with a standard ferroelectric testing unit (Precision Premier II, Radiant Technologies) connected to a high-voltage interface, which also provided the voltage pulses for poling purpose.

In order to characterize the mechanical energy harvesting performance of the nanotube arrays, a setup was used as shown schematically in Figure 4.2, which is a slight modification of the commercially available Bruker Dimension Icon Scanning Probe Microscope (SPM). The sample is mounted onto the sample chuck and secured with conducting tape to ensure the electrical contact between the bottom electrode and the chuck. A conducting AFM tip (Veeco SCM-PIC with a force constant of 0.2 N/m and a 20-nm PtIr/ 3-nm Cr coating) was used to probe the sample. It was mounted onto the conducting-AFM holder, which has an attached wire that allows the electrical connection to the tip. The system was operated in the continuous Z-ramping mode with a ramp size of 3 μm and Z scan rate of 0.1 Hz, in order to provide periodic mechanical deformation to the sample. The tip deflection

was measured by the standard deflection feedback system of the SPM, and thus the

force curves were obtained. The currents generated were measured using a Keithley

6514 electrometer that was electrically connected with one terminal to the AFM tip,

while the other terminal was connected to the sample chuck. The electrometer was

computer controlled by a LabVIEW program which was set to take and record data

every 100 ms.
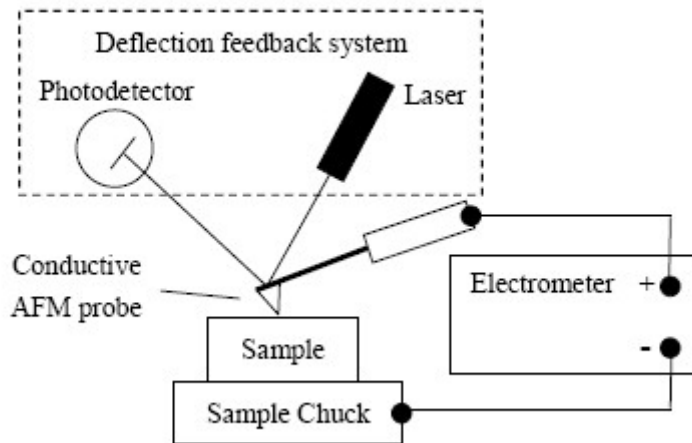
Figure 4.2 Modified C-AFM setup to characterize mechanical energy harvesting performance.

4.2.3 Theoretical simulations

Commercially available ANSYS software was used to simulate the mechanical

deformation and energy harvesting capacity of the P(VDF-TrFE) nanotubes. The

P(VDF-TrFE) nantube was modeled with 3D element SOLID226. The electrodes

were represented by coupling the voltage degree-of-freedom on nodes in electrode

areas of solid model. The energy harvesting capacity was defined as the electric

energy generated in the nanotube under open circuit condition, i.e., the electric energy stored in a capacitor. It can be calculated as $E=Q^2/C$ where Q is the electric charge generated by piezoelectric effect and C is the capacitance of the nanotube. For the current calculation, a piezoelectric circuit element CIRCU94 was connected to the two electrodes of the nanotube model, which was used to model the external electrical resistor. The electric current was calculated by examining the current across this piezoelectric circuit element during the mechanical deformation of the nanotube. Top and bottom electrodes were incorporated, and the external load resistance R was set to be 1 kΩ (consistent with actual setup). The P(VDF-TrFE) nanotubes were assumed to be vertically polarized. In order to compare the performance of nanorod and nanotube, the outer radius was fixed at 150 nm while the inner radius was varied from 0 nm to 120 nm. The length was fixed at 2 μm. Both the nanotube length and outer radius were typical of the actual values that had been obtained experimentally. A typical tip force of 80 nN was applied in the vertical and horizontal directions, and energy harvesting capacity was computed under a static deformation condition.

4.3 Results and discussion

4.3.1 Simulation results of energy harvesting capacity in single P(VDF-TrFE) nanotube

Figures 4.3(a) and 4.3(b) show illustrative simulated deformation profiles of a 30-nm-thick (120-nm inner radius) P(VDF-TrFE) nanotube under an applied 80 nN

force in the vertical and horizontal directions. The simulated energy harvesting capacity and nanotube deformation are plotted as a function of nanotube inner radius in Figures 4.3(c) and 4.3(d), for 80 nN applied force in the vertical and horizontal directions respectively. It can be seen that under the same force, a 30 nm thick nanotube can deform about twice as much as a nanorod, and its energy harvesting capacity is almost one order of magnitude larger, which convincingly indicates that the nanotube structure is superior to nanorod for energy harvesting.
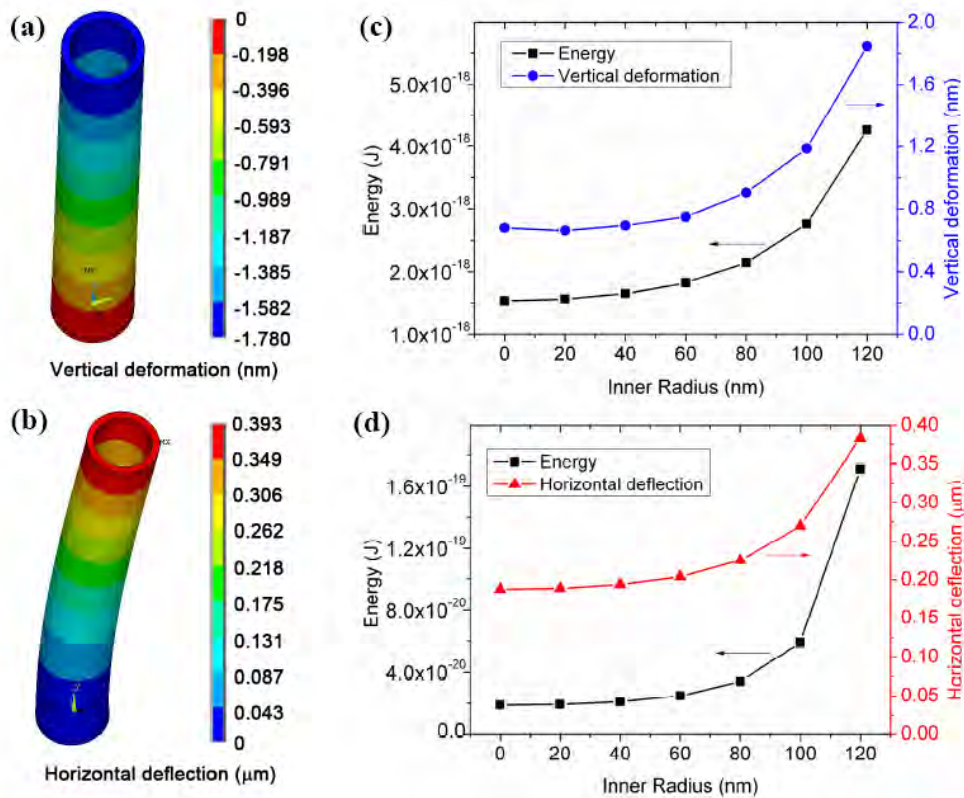
Figure 4.3 Simulated values of: (a) Nanotube deformation profile (in nm) due to 80 nN vertical force; (b) Nanotube bending profile (in μm) due to 80 nN horizontal force; (c) Energy harvesting capacity and deformation under constant applied 80 nN vertical force for different tube inner radius; (d) Energy and deformation for force applied in horizontal direction

4.3.2 Morphology, crystalline phase and ferroelectric characterization of P(VDF-TrFE) nanotubes

Figure 4.4(a) shows a typical SEM image of the top view of the AAM template, indicating pore sizes of around 250-300 nm in diameter. An SEM image of the released P(VDF-TrFE) nanotube array fabricated by hot-press is shown in Figure 4.4(b). It can be seen that the nanotubes are not oriented perfectly vertical; instead they have a tendency to bunch up together into clusters with gaps in between. Figure 4.4(c) is a representative TEM image of a P(VDF-TrFE) nanotube. This image confirms the hollow structure of the nanotube, and indicates a thickness of approximately 30 nm.
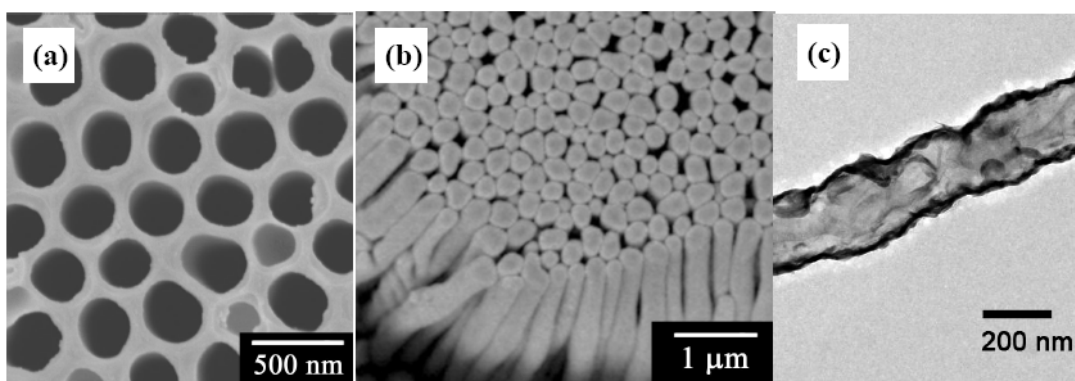
Figure 4.4 (a) SEM image of AAM template, top view; (b) SEM image of released P(VDF-TrFE) nanotubes fabricated by hot-press; (c) TEM image of a P(VDF-TrFE) nanotube.

X-ray diffraction (XRD) data for P(VDF-TrFE) nanotubes are shown in Figure 4.5(a). It indicatesthat the P(VDF-TrFE) nanotubes are ferroelectric β phase dominated [22]. This is not surprising, since the incorporation of TrFE into PVDF is known to promote the formation of the polar β phase all-trans configuration due to sterical hindrance effect of the additional fluorine atoms [23]. Representative

ferroelectric hysteresis loops are plotted in Figure 4.5(b) for different values of maximum applied voltage, V_{MAX}. The P(VDF-TrFE) nanotubes exhibit a remnant polarization P_r of 57 mC/m^2, which is comparable to what have been reported previously for P(VDF-TrFE) thin films [24], thus confirming the good ferroelectric property of the nanotubes. However, the nanotube samples show very large coercive fields E_C of around 570 MV/m, while the value reported for P(VDF-TrFE) thin film is 68 MV/m [24]. This may be due to the unique configuration of the polymer chains in the low dimensional nanotubes.
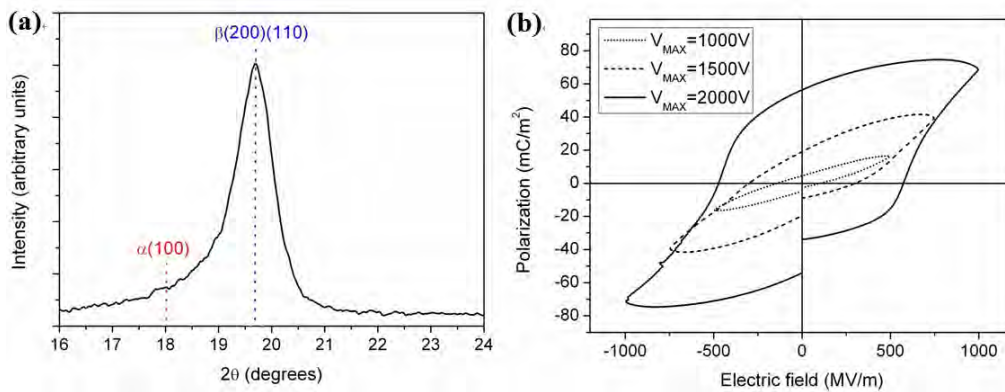
Figure 4.5 (a) X-ray diffraction (XRD) data of P(VDF-TrFE) nanotubes, with the assignment of α and β peaks according to literature values; (b) Ferroelectric hysteresis loops of P(VDF-TrFE) nanotubes for different values of maximum applied voltage, V_{MAX}.

4.3.3   Current generation in P(VDF-TrFE) nanotube array measured by Conductive AFM

To evaluate the mechanical energy harvesting, the nanotubes are subjected to deformation by a conducting AFM tip operated in the continuous Z-ramping mode. The setup is a slight modification of a commercial AFM system (Figure 4.2). In order to provide an understanding of the tip behavior as it approaches the sample, a

typical force curve was obtained and plotted in Figure 4.6. It shows the tip deflection

as a function of scanner Z height. It can be seen that at the beginning of each ramp

cycle (Z = 0 μm), the tip was initially not in contact with the sample. At

approximately Z = 1.4 μm (a larger Z value indicates a lower tip position), the tip

first comes into contact, and the maximum tip deflection (and hence sample

deformation) occurs at Z = 3 μm (corresponding to the ramp size). The maximum tip

deflection is about 400 nm, which corresponds to a tip force of 80 nN since the tip

force constant is given by the manufacturer to be 0.2 N/m. This 80 nN force is the

value that is used in the numerical simulations. At the point where the tip is leaving

the sample surface, there is a small negative deflection as a result of a sticking force

between the tip and the sample, thus bending the tip in the opposite direction. One

cycle was completed in 10 s (hence 0.1 Hz), and the next cycle followed

immediately after the previous one.
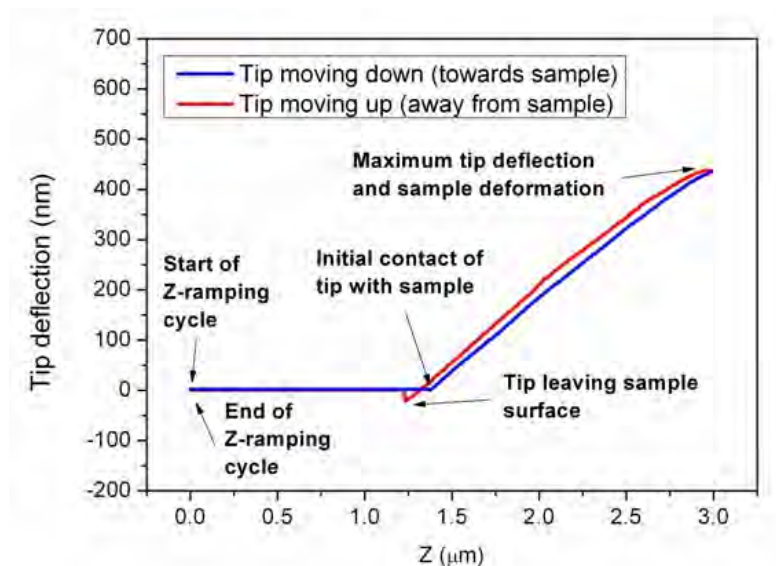
Figure 4.6 Typical AFM force-curve showing the tip deflection as a function of the scanner Z height.

The mechanically generated currents from a P(VDF-TrFE) nanotube array sample are plotted as a function of time as shown in Figure 4.7. For the as-fabricated sample without any poling, the generated current is on the order of 50 pA. The current pulses have a well-defined 10 s period, which is consistent with the ramping frequency. From the force curve shown in Figure 4.6, we know that there is a part of the cycle whereby the AFM tip is not in contact with the sample; this corresponds to the zero-current portions of the graph. In order to be sure that this current is generated by the nanotubes and is not a result of artifacts in the system, mechanically generated currents from a control, a PVDF homopolymer nanotube array sample are also measured and found to be on the order of 1 pA. It is well known that for PVDF the non-polar α phase is thermodynamically favored, XRD data confirmed that the PVDF nanotubes are α phase. Hence, the PVDF nanotubes are not expected to generate any current, and the 1 pA signal is an indication of the level of noise in the system. Since the generated currents from the P(VDF-TrFE) nanotube sample (~50 pA) are much higher than the noise level, it should be a real indication of energy harvesting from the P(VDF-TrFE) nanotubes.

In order to investigate the effect of polarization on energy harvesting, the P(VDF-TrFE) nanotube sample was subjected to poling by voltage pulses of 20 ms duration applied to the top electrode and then characterized for current generation. Figure 4.7 illustrates the effect of applying +/- 300 V pulses to pole this sample. The positive voltage pulse boosted the generated currents from 50 pA to 150 pA, while

the negative pulse reduced it to 25 pA. This result indicates that poling electric field plays an important role, and that the observed currents are largely due to the polarization-dependant piezoelectric effect. Although the negative pulse was able to reduce the current, it was not able to completely switch the current direction. We observed that the current direction was not completely changed despite application of voltage pulses as high as -1200 V; higher voltages were not attempted due to a high chance of destroying the sample. The inability to switch the current (and hence polarization) direction may be attributed to the extremely high coercive field of the nanotube sample (see Figure 4.5(b)). For comparison, the mechanical energy harvesting of β phase PVDF film and nanotubes were measured under same experimental condition of P(VDF-TrFE) nanotubes. The current generated by film (-5 pA) was significantly lower than the current generated by poled P(VDF-TrFE) nanotube sample (150 pA). Hence the nanotube structure had better performance than films in mechanical energy harvesting. The current generated by β phase PVDF nanotube (30-40 pA) was comparable to the current generated by as-fabricated P(VDF-TrFE) nanotube sample (50 pA). This result also indicated that the PVDF and P(VDF-TrFE) nanotubes might be self-polarized.
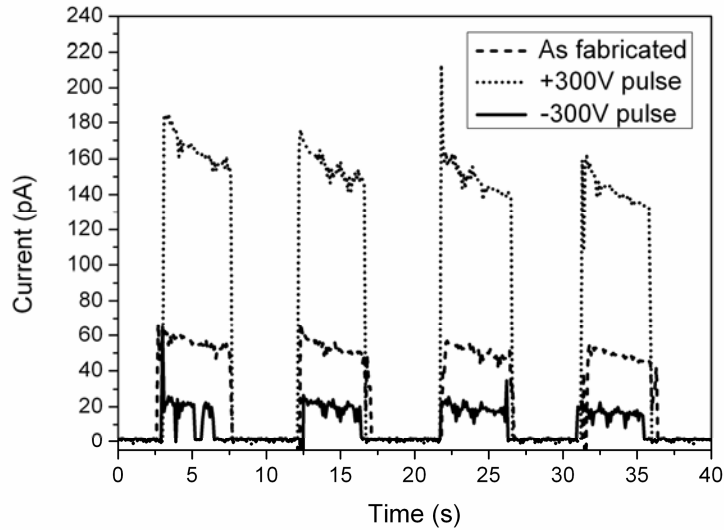
Figure 4.7 Mechanically generated current from a hot-pressed P(VDF-TrFE) nanotube sample. Data is plotted for the as-fabricated sample without any poling, as well as for the sample subjected +/- 300 volt pulses.

In order to gain further understanding of the experimental results, theoretical simulations are performed to calculate the current generated from one single P(VDF-TrFE) nanotube. Simulation conditions are designed to match as closely as possible to the experiment, whereby a 80 nN force was applied and then released. It was determined that a single vertically polarized nanotube will generate a current of 22.1 pA with force applied in vertical direction, and a very small current of 0.001 pA with force applied in horizontal direction. These theoretical results together with the experimental values are summarized in Table 4.1.

Table 4.1 Summary of current generation from nanotubes due to applied 80 nN force.

	Sample	Force direction	Generated current (pA)
Experimentally measured	P(VDF-TrFE) nanotube array, poled vertically	Vertical	150
	PVDF nanotube array (control)	Vertical	1
Theoretically calculated	Single P(VDF-TrFE) nanotube, vertically polarized	Vertical	22.1
	Single P(VDF-TrFE) nanotube, vertically polarized	Horizontal	0.001

From Table 4.1, it can be calculated that in order to obtain the measured current of ~150 pA, several nanotubes are required if the nanotubes are vertically polarized and deformed vertically. As multiple P(VDF-TrFE) nanotubes are covered and linked with one circular gold electrode, it is likely that the AFM tip is able to mechanically deform multiple nanotubes although the AFM tip radius (typically 10-100 nm) is comparable with one individual nanotube. Based on the results presented in Table 4.1, it is plausible that the current is mostly generated from a few vertically deformed nanotubes that are near the AFM tip contact point; nanotubes far from the contact point may have a tendency to deform horizontally rather than vertically, hence their contribution to the measured current are minor.

4.4 Conclusion

In summary, solid nanorod structure can be treated as a special case of the hollow nanotube, and the numerical simulations indicate that under constant force condition,

the flexible piezoelectric polymer nanotube structure is superior to the nanorod in terms of electrical energy generation by harvesting mechanical energy. Mechanical energy harvesting has been experimentally demonstrated for the first time with piezoelectric P(VDF-TrFE) nanotube array, using a conducting AFM tip to provide periodic mechanical deformation and also to measure the generated current. The current generation in the polymer nanotubes is correlated to the existence of polar phase in the polymer and the electrical poling conditions, which shows that polarization and piezoelectric effect play the dominant roles in the mechanical to electrical energy conversion. The theoretical analyses and experimental demonstration show that the flexible ferroelectric polymer nanotube array is a very promising candidate for mechanical energy harvesting applications.

References

[1]   S. P. Beeby, M. J. Tudor, and N. M. White, "Energy harvesting vibration sources for microsystems applications," *Measurement Science & Technology,* vol. 17, pp. R175-R195, Dec 2006.

[2]   S. R. Anton and H. A. Sodano, "A review of power harvesting using piezoelectric materials (2003-2006)," *Smart Materials & Structures,* vol. 16, pp. R1-R21, Jun 2007.

[3]   Z. L. Wang and J. H. Song, "Piezoelectric nanogenerators based on zinc oxide nanowire arrays," *Science,* vol. 312, pp. 242-246, Apr 2006.

[4]   X. D. Wang, J. H. Song, J. Liu, and Z. L. Wang, "Direct-current nanogenerator driven by ultrasonic waves," *Science,* vol. 316, pp. 102-105, Apr 2007.

[5]   G. A. Zhu, R. S. Yang, S. H. Wang, and Z. L. Wang, "Flexible High-Output Nanogenerator Based on Lateral ZnO Nanowire Array," *Nano Lett,* vol. 10, pp. 3151-3155, Aug 2010.

[6]   S. N. Cha, J. S. Seo, S. M. Kim, H. J. Kim, Y. J. Park, S. W. Kim, and J. M. Kim, "Sound-Driven Piezoelectric Nanowire-Based Nanogenerators," *Advanced Materials,* vol. 22, pp. 4726-+, Nov 2010.

[7]   H. K. Yu, J. M. Baik, and J.-L. Lee, "Self-Connected and Habitually Tilted Piezoelectric Nanorod Array," *Acs Nano,* vol. 5, pp. 8828-8833, Nov 2011.

[8]   G. Zhu, A. C. Wang, Y. Liu, Y. Zhou, and Z. L. Wang, "Functional Electrical Stimulation by Nanogenerator with 58 V Output Voltage," *Nano Lett,* vol. 12, pp. 3086-3090, Jun 2012.

[9]   Y.-F. Lin, J. Song, Y. Ding, S.-Y. Lu, and Z. L. Wang, "Piezoelectric nanogenerator using CdS nanowires," *Applied Physics Letters,* vol. 92, Jan 14 2008.

[10]   W. S. Su, Y. F. Chen, C. L. Hsiao, and L. W. Tu, "Generation of electricity in GaN nanorods induced by piezoelectric effect," *Applied Physics Letters,* vol. 90, Feb 5 2007.

[11]   Z. Wang, J. Hu, A. P. Suryavanshi, K. Yum, and M.-F. Yu, "Voltage generation from individual BaTiO3 nanowires under periodic tensile

mechanical load," *Nano Lett,* vol. 7, pp. 2966-2969, Oct 2007.

[12]   X. Chen, S. Xu, N. Yao, and Y. Shi, "1.6 V Nanogenerator for Mechanical Energy Harvesting Using PZT Nanofibers," *Nano Lett,* vol. 10, pp. 2133-2137, Jun 2010.

[13]   S. Xu, G. Poirier, and N. Yao, "PMN-PT Nanowires with a Very High Piezoelectric Constant," *Nano Lett,* vol. 12, pp. 2238-2242, May 2012.

[14]   S. Cha, S. M. Kim, H. Kim, J. Ku, J. I. Sohn, Y. J. Park, B. G. Song, M. H. Jung, E. K. Lee, B. L. Choi, J. J. Park, Z. L. Wang, J. M. Kim, and K. Kim, "Porous PVDF as effective sonic wave driven nanogenerators," *Nano Lett,* vol. 11, pp. 5142-7, Dec 14 2011.

[15]   J. Fang, X. Wang, and T. Lin, "Electrical power generator from randomly oriented electrospun poly(vinylidene fluoride) nanofibre membranes," *Journal of Materials Chemistry,* vol. 21, pp. 11088-11091, 2011 2011.

[16]   K. Laxminarayana and N. Jalili, "Functional nanotube-based textiles: Pathway to next generation fabrics with enhanced sensing capabilities," *Textile Research Journal,* vol. 75, pp. 670-680, Sep 2005.

[17]   M. H. Zhao, Z. L. Wang, and S. X. Mao, "Piezoelectric characterization of individual zinc oxide nanobelt probed by piezoresponse force microscope," *Nano Lett,* vol. 4, pp. 587-590, Apr 2004.

[18]   T. Yamada, T. Ueda, and T. Kitayama, "PIEZOELECTRICITY OF A HIGH-CONTENT LEAD ZIRCONATE TITANATE POLYMER COMPOSITE," *Journal of Applied Physics,* vol. 53, pp. 4328-4332, 1982

1982.

[19] C. Q. Chen, Y. Shi, Y. S. Zhang, J. Zhu, and Y. J. Yan, "Size dependence of Young's modulus in ZnO nanowires," *Physical Review Letters,* vol. 96, Feb 24 2006.

[20] T. Fett, S. Muller, D. Munz, and G. Thun, "Nonsymmetry in the deformation behaviour of PZT," *Journal of Materials Science Letters,* vol. 17, pp. 261-265, Feb 15 1998.

[21] M. F. Daqaq and D. Bode, "Exploring the parametric amplification phenomenon for energy harvesting," *Proceedings of the Institution of Mechanical Engineers Part I-Journal of Systems and Control Engineering,* vol. 225, pp. 456-466, Jun 2011.

[22] R. Gregorio and M. Cestari, "EFFECT OF CRYSTALLIZATION TEMPERATURE ON THE CRYSTALLINE PHASE CONTENT AND MORPHOLOGY OF POLY(VINYLIDENE FLUORIDE)," *Journal of Polymer Science Part B-Polymer Physics,* vol. 32, pp. 859-870, Apr 15 1994.

[23] X. Li, S. Chen, K. Yao, and F. E. H. Tay, "Ferroelectric Poly(vinylidene fluoride) PVDF Films Derived from the Solutions with Retainable Water and Controlled Water Loss," *Journal of Polymer Science Part B-Polymer Physics,* vol. 47, pp. 2410-2418, Dec 1 2009.

[24] S. T. Chen, K. Yao, F. E. H. Tay, and L. L. S. Chew, "Comparative Investigation of the Structure and Properties of Ferroelectric Poly(vinylidene fluoride) and Poly(vinylidene fluoride-trifluoroethylene) Thin Films

Crystallized on Substrates," *Journal of Applied Polymer Science,* vol. 116, pp.

3331-3337, Jun 2010.

Chapter 5 Solution-derived ferroelectric β-phase PVDF thin films

5.1 Introduction

As introduced in Chapter 1, PVDF homopolymer and its copolymers have attracted intensive research interests due to their useful dielectric, ferroelectric and piezoelectric properties. Compared to the copolymer P(VDF/TrFE), PVDF homopolymer has many advantages, such as larger intrinsic polarization, higher Curie temperature, higher breakdown strength, significantly lower cost and ready availability.

As a semi-crystalline polymer, the non-polar α phase (TGTG') of PVDF homopolymer is thermodynamically most stable among its α, β, γ and δ four crystalline phases [1]. Increasing the β-phase content in PVDF is always critical and attractive in the research field, since β-phase PVDF exhibits the most superior ferroelectric and piezoelectric properties due to its all-trans planar zigzag structure.

One effective approach to obtain the β-phase PVDF in industry manufacture is through mechanical stretching [2], but it is not applicable for thin film samples on a substrate. The other reported physical methods including introducing high electric field [3] and high pressure [4] treatments are not as effective and scalable. Therefore,

the applications of ferroelectric PVDF homopolymer on a substrate have not been realized.

It should be noted that β phase could be achieved in PVDF films derived from polar solvents [5], but the films were too porous for electrical applications. Benz *et al* reported that β phase could be promoted in PVDF with the presence of water [6], but the obtained PVDF samples were also very porous without showing any useful ferroelectric or piezoelectric properties. Here we explored two novel approaches to promote the β phase formation in PVDF homopolymer thin films, namely incorporation of hydrated and hydroscopic chemicals, and layer by layer Langmuir-Blodgett deposition. Both approaches rely on the hydrogen bond interaction between water and PVDF polymer chain to promote β phase.

Recently, our group succeeded in obtaining dense β-phase dominant PVDF films on silicon substrate by introducing magnesium nitrate hexahydrate ($Mg(NO_3)_2 \cdot 6H_2O$) in the PVDF precursor solution and demonstrated useful ferroelectric and piezoelectric properties [7, 8]. Our previous study showed that the water molecules in $Mg(NO_3)_2 \cdot 6H_2O$ could form hydrogen bonds with PVDF during the crystallization process and the hydrogen bonds promoted the β phase with all-trans conformation [8].

However, thermogravimetric analysis showed that the water in $Mg(NO_3)_2 \cdot 6H_2O$ could not be completely removed after the annealing treatment and thus remained in the films. The remaining water in PVDF films caused large leakage current and dielectric loss, especially in films with high concentrations of $Mg(NO_3)_2 \cdot 6H_2O$. In addition, the previously obtained PVDF films as reported also exhibited extremely high surface roughness, possibly because of the remnant hydrated salt. Our experimental efforts also showed that directly adding water into PVDF precursor solution does not have any substantial effects of promoting the β phase in PVDF, possibly due to the evaporation of the water in the thin film samples before crystallization. Therefore, how to appropriately manipulate the water retaining and control its loss in the PVDF precursor solutions and the resulting thin films are critical to achieving useful β-phase PVDF films on a substrate for ferroelectric and piezoelectric device applications.

In this work, several hydrated and hygroscopic chemicals are introduced in the PVDF precursor solution and their effects on the structure and properties of the resulting PVDF are further investigated. The retaining and loss of water in PVDF film introduced by hydrated salts are manipulated to fully make use of water to promote the β phase during the film crystallization, but also completely remove water in the finally obtained film without deteriorating the electrical properties.

Furthermore, PVDF homopolymer ultra-thin films are prepared on silicon substrates by the LB deposition method, in which it was discovered that the LB deposition process directly led to the ferroelectric β-phase crystal with the molecular chains parallel to the substrates and the dipoles aligned perpendicular to the substrates. The underlying mechanism of forming β phase and molecule/dipole orientation was explained with the hydrogen bonding interaction between PVDF molecules and water in the LB deposition.

5.2 Experimental

5.2.1 Fabrication of PVDF thin films with hydrated and hygroscopic chemicals

PVDF powder (M_w=534,000) and all the hydrated and hygroscopic chemicals are purchased from Aldrich. To select appropriate chemicals to retain water in the PVDF films, characteristics of different hydrated and hygroscopic chemicals were examined, particularly in terms of the contained water amount, dehydration and decomposition temperatures. In this paper, four hydrated and hygroscopic chemicals, aluminum nitrate nonahydrate ($Al(NO_3)_3 \cdot 9H_2O$), aluminum chloride hexahydrate ($AlCl_3 \cdot 6H_2O$), chromium nitrate nonahydrate ($Cr(NO_3)_3 \cdot 9H_2O$), tetra-n-butylammonium chloride (TBAC), and one hygroscopic but nonhydrated chemical, ammonium acetate (NH_4OAc) are reported.

The hydrated and hygroscopic chemicals were first dissolved in a mixed solvent of dimethylformamide (DMF) and acetone (1:1 in volume). The PVDF powder was

then added into the solution and heated at 50 °C to obtain a 5 wt% PVDF precursor solution. It should be noted that all the concentration values for the added hydrated and hygroscopic chemicals as cited in the following sections refer to the weight concentrations of the chemicals in the solid PVDF. The PVDF films were deposited by spin coating the solution on aluminum-coated silicon substrates followed by immediate drying and crystallization on a hotplate at 100 °C for 10 minutes. The samples were subsequently annealed at 135 °C for 12 hours in an oven. Gold top electrodes with a thickness of 300 nm were deposited on the top of the films by sputtering for the electrical testing. Before piezoelectric measurement, the films were poled at 100 $^{\circ}$C for 3 minutes under an electric field of 200 MV/m.

5.2.2 Fabrication of PVDF LB films

The PVDF solution was prepared at concentration of 0.05 wt% with the solvent of DMF/Acetone (1:1 in volume). The LB films were deposited by an automated LB trough (NIMA 622C) filled with purified water (18 MΩ cm). The solutions were dispersed on the surface of the water (stabilized at 25 °C) and slowly compressed to the target pressure of 5 mN/m, which was kept constant during the film transfer. The films were transferred to Au-coated SiO_2/Si substrate one layer at a time in ideal cases using the Schaefer horizontal deposition. The LB films were dried at room temperature for 5 minutes after the transfer of each monolayer. After transferred for 20 cycles, the obtained LB films were annealed at 135 $^{\circ}$C in an oven to improve the degree of crystallization.

5.2.3 Characterization of PVDF films

Thermogravimetric analyses (TGA) were conducted for examining the water loss with a thermal gravimetric analyzer (TGA Q500, TA Instruments) at a scan rate of 20 °C/min in air. The thicknesses of the PVDF films were measured using a profiler (Tensor P-10), which were within the range of 0.9-1.1 μm. The crystalline structures were examined with Fourier transform infrared (FTIR) spectroscopy (Spectrum 2000, Perkin Elmer) and x-ray diffraction (XRD) system (D8-ADVANCE, Bruker AXS GmbH, Karlsruhe). The surface morphology of the PVDF films was observed with field emission scanning electron microscopy (FESEM, JSM-6700F, JEOL). The polarization and electric field (P−E) hysteresis loops were measured using a standard ferroelectric testing system (RT66A, Radiant Technologies) connected with a high-voltage interface. The effective piezoelectric constant d_{33} for the PVDF films on the silicon substrates was measured with a laser scanning vibrometer method (OFV-3001-SF6, PolyTech GmbH) [9].

5.3 Results and discussion

5.3.1 PVDF films with hydrated and hygroscopic chemicals

5.3.1.1 PVDF films with hydrated and hygroscopic chemicals

Thermal analyses of hydrated and hygroscopic chemicals

Figure 5.1(a) presents the TGA results of the hydrated and hygroscopic chemicals at a heating rate of 20 °C/min in the temperature range of 25-500 °C. At around 100°C, corresponding to the temperature in which the PVDF films were dried and crystallized, NH_4OAc decomposed rapidly; $Cr(NO_3)_3 \cdot 9H_2O$ lost about 33 % of water (estimated from the observed weight loss); the other three hydrated salts: $Al(NO_3)_3 \cdot 9H_2O$, $AlCl_3 \cdot 6H_2O$ and TBAC lost less than 20 % of water. With the temperature increased, the hygroscopic chemical NH_4OAc decomposed completely at 114°C; At 135°C, which was the annealing temperature of the PVDF films, $Cr(NO_3)_3 \cdot 9H_2O$ lost about 75 % of water, $Al(NO_3)_3 \cdot 9H_2O$ lost about 50 % of water, $AlCl_3 \cdot 6H_2O$ and TBAC lost less than 50 % of water, in the TGA curves in Figure 5.1(a). However, water loss was much more complete for $Cr(NO_3)_3 \cdot 9H_2O$, $Al(NO_3)_3 \cdot 9H_2O$ and $AlCl_3 \cdot 6H_2O$ if temperature was held at 135°C for a longer time.
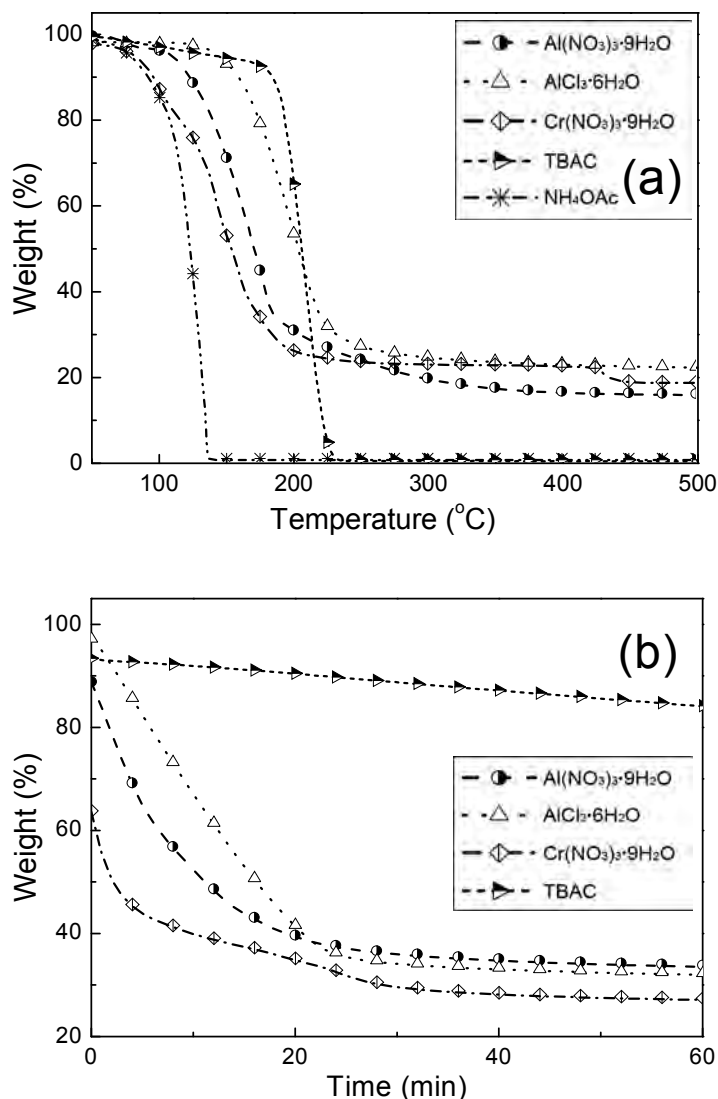
Figure 5.1 Thermogravimetric analysis (TGA) of the hydrated and hygroscopic chemicals: (a) heated to 500°C at 20°C/min; (b) isothermal curves at 135°C for 60 minutes.

To further examine the dehydration and decomposition processes of these hydrated and hygroscopic chemicals at the annealing temperature for the PVDF films, the chemicals were heated to 135 °C and held at this temperature for 60 minutes. Figure 5.1(b) presents the weight loss of these chemicals in the isothermal process. After the isothermal process, $Al(NO_3)_3 \cdot 9H_2O$, $AlCl_3 \cdot 6H_2O$ and $Cr(NO_3)_3 \cdot 9H_2O$ completely dehydrated and started to decompose; TBAC lost only 28% of water. NH_4OAc

completely decomposed before temperature reaching 135°C (not shown in Figure 5.1(b)). According to the TGA results, NH_4OAc could retain little water in the drying and crystallization temperature of PVDF film (100°C) and completely decomposed before the annealing process, while all the other hydrated chemicals could retain certain amount of water at 100°C. During the annealing treatment at 135 °C, $Al(NO_3)_3 \cdot 9H_2O$, $AlCl_3 \cdot 6H_2O$ and $Cr(NO_3)_3 \cdot 9H_2O$ could completely dehydrate and decompose, but not for the TBAC. The weight losses at 100 °C in the TGA scan curves and after 60-min isothermal process at 135 °C for these chemicals are summarized in Table 5.1.

Table 5.1 Weight loss of the hydrated and hygroscopic chemicals at different thermal conditions and crystalline phase of the resulting PVDF films from the precursor solutions with the chemicals

Chemical	Weight percentage of water (%)	Weight loss at 100°C (%)	Weight loss after isothermal at 135°C (%)	Crystalline phase of PVDF film
$Al(NO_3)_3 \cdot 9H_2O$	43.2	3.6	66.5	β phase dominant
$AlCl_3 \cdot 6H_2O$	44.8	1.9	66.6	Mixture of α and β phases
$Cr(NO_3)_3 \cdot 9H_2O$	40.5	13.3	72.8	Mixture of α and β phases
TBAC	≈66.1	2.8	19	β phase dominant
NH_4OAc	Hygroscopic	14.7	100	α phase dominant

Structures of PVDF films

To clearly show the relationship between water retaining and crystalline phase of the corresponding PVDF films, Table 5.1 also lists the crystalline phases of the PVDF films determined by FTIR and XRD. Figure 5.2 presents the FTIR spectra of the PVDF films with different hydrated and hygroscopic chemicals. The characteristic absorption bands of α-phase PVDF are at 764 and 975 cm^{-1}, while β phase has characteristic absorption bands at 840 and 1276 cm^{-1}, which are marked in Figure 5.2. The band at 764 cm^{-1} is assigned to CF_2 in-plane rocking mode; and the band at 975 cm^{-1} is assigned to CH_2 twisting in α phase. The band at 840 cm^{-1} is assigned to a mixture of CH_2 rocking and CF_2 asymmetric stretching; and the band at 1276 cm^{-1} is assigned to a mixture of CC stretching and CF_2 asymmetric stretching in β phase. [10]

The FTIR spectrum of the PVDF film with NH_4OAc showed the α-phase peak with very little β-phase peak. The PVDF films with $Al(NO_3)_3 \cdot 9H_2O$ and TBAC were β phase dominant, while the PVDF film with $AlCl_3 \cdot 6H_2O$ and $Cr(NO_3)_3 \cdot 9H_2O$ had mixed α and β phases.
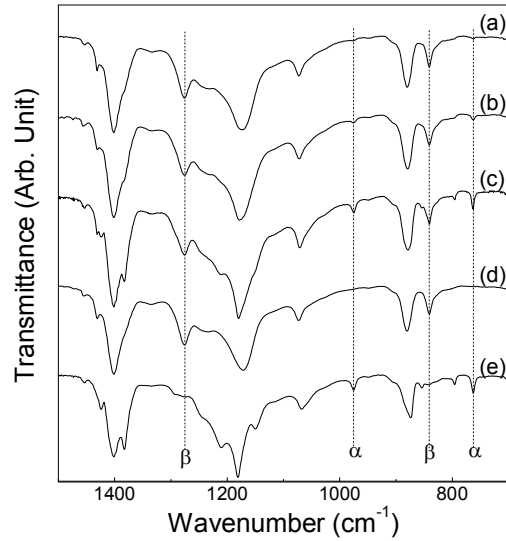
Figure 5.2 FTIR spectra of PVDF films with (a) Al(NO$_3$)$_3$·9H$_2$O; (b) AlCl$_3$·6H$_2$O; (c) Cr(NO$_3$)$_3$·9H$_2$O; (d) TBAC; and (e) NH$_4$OAc. The unmarked peaks are common to both α and β phases. The concentration of the hydrated and hygroscopic chemicals in PVDF is 4 wt%

The XRD patterns as shown in Figure 5.3 further confirmed the crystalline structures of the films as concluded from FTIR analyses. The XRD peaks at 18.4° and 20.1° are attributed to the (100) and (110) crystal planes of the α phase, and the peak at 20.8° to the (110)(200) plane of β phase. The films with Cr(NO$_3$)$_3$·9H$_2$O and NH$_4$OAc exhibited strong α-phase peaks, while the films with Al(NO$_3$)$_3$·9H$_2$O and TBAC exhibited strong and sharp β-phase peak with little α-phase peaks.
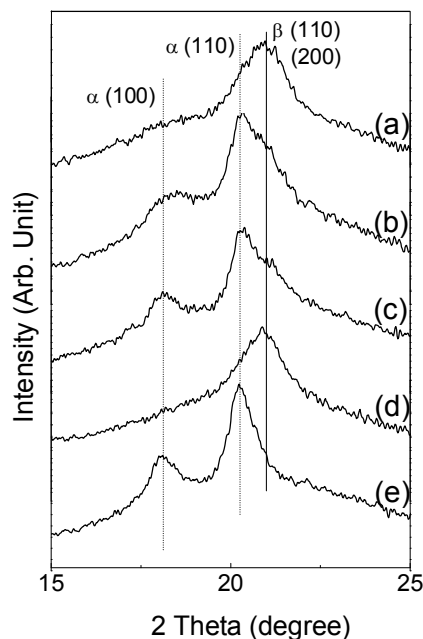
Figure 5.3 XRD patterns of the PVDF films with (a) Al(NO$_3$)$_3$·9H$_2$O; (b) AlCl$_3$·6H$_2$O; (c) Cr(NO$_3$)$_3$·9H$_2$O; (d) TBAC; and (e) NH4OAc. The concentration of the hydrated and hygroscopic chemicals in PVDF is 4 wt%.

From Table 5.1, it can be seen that all the hydrated chemicals promoted the β-phase formation in the PVDF films. To promote the β phase, sufficient amount of water should be retained during the crystallization process of the PVDF films at 100°C. Among the hydrated and hygroscopic chemicals, Al(NO$_3$)$_3$·9H$_2$O, AlCl$_3$·6H$_2$O, and TBAC had much smaller weight loss at 100°C than NH$_4$OAc and Cr(NO$_3$)$_3$·9H$_2$O, and thus could retain much more significant amount of water during the drying and crystallization process of the PVDF films. The hygroscopic chemical NH$_4$OAc exhibited much weaker β-phase promotion ability than the hydrated salts, mainly due to the instability of water in NH$_4$OAc and substantial water loss at 100°C. The water molecules in the hygroscopic NH$_4$OAc are only weakly bonded physically, in contrast to the strong chemical bonding between the hydrated water and metal ions

in the hydrated salts. This also explained the previous observation that the direct addition of water to the precursor solution could not effectively promote the β phase because water evaporated quickly even before the PVDF crystallization process. Among the hydrated salts here, the β-phase promotion ability of $Cr(NO_3)_3 \cdot 9H_2O$ was relatively weaker with large amount of α phase due to its significant water loss at 100°C. The PVDF film with TBAC exhibited most β phase among all the films because TBAC contained most water in the crystallization process.

For the two hydrated aluminium salts $Al(NO_3)_3 \cdot 9H_2O$ and $AlCl_3 \cdot 6H_2O$, the weight percentage of water and weight loss in crystallization temperature were similar. However, the PVDF film with $AlCl_3 \cdot 6H_2O$ contained more substantial amount of α phase. The difference in β-phase promotion ability could be due to the different crystal structure of these two salts. All of the six water molecules in $AlCl_3 \cdot 6H_2O$ coordinate with Al^{3+} ion to form $Al(6H_2O)^{3+}$ octahedron. In the case of $Al(NO_3)_3 \cdot 9H_2O$, 6 water molecules coordinate with Al^{3+} ion, form the $Al(6H_2O)^{3+}$ octahedron, while the other 3 water molecules do not participate the octahedron [11]. The 3 water molecules may have more mobility to interact with PVDF polymer chain through the hydrogen bonds than the ones in $Al(6H_2O)^{3+}$ octahedron, hence the β-phase promotion ability of $Al(NO_3)_3 \cdot 9H_2O$ was slightly stronger than $AlCl_3 \cdot 6H_2O$. Therefore, molecular structure also affects the interaction of the water (hydrogen bond) with the PVDF and the effect of promoting the β phase, in addition to the water amount.

Electrical properties of PVDF films

Among all the chemicals, TBAC retained the most water at the crystallization temperature, so that it exhibited the strongest β-phase promotion effect. However, unlike $Al(NO_3)_3 \cdot 9H_2O$, TBAC could not completely dehydrate even after the film annealing at 135°C and thus large amount of water was retained in the annealed PVDF films, which seriously deteriorated the electrical properties of the resulting PVDF films.
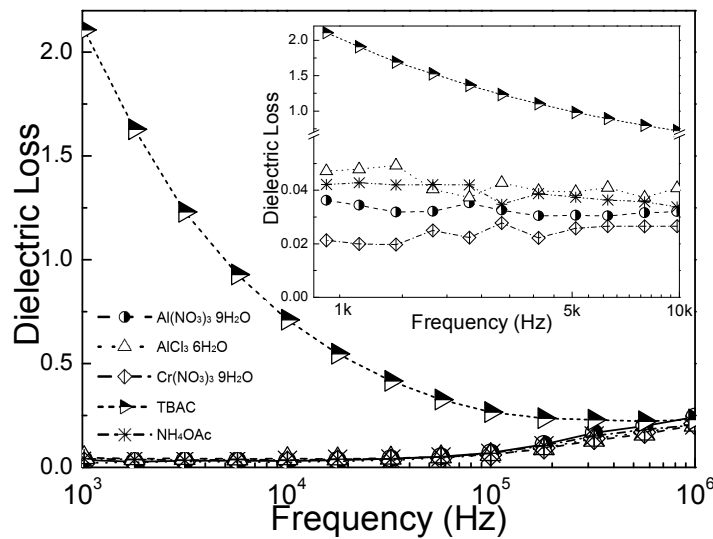
Figure 5.4 Dielectric loss of the PVDF films derived from solutions with different hydrated and hygroscopic chemicals: (a) $Al(NO_3)_3 \cdot 9H_2O$; (b) $AlCl_3 \cdot 6H_2O$; (c) $Cr(NO_3)_3 \cdot 9H_2O$; (d) TBAC; and (e) NH_4OAc. The concentration of the chemicals in PVDF is 4 wt%.

Figure 5.4 presents the dielectric loss of the PVDF films derived from solutions with different hydrated and hygroscopic chemicals. The film with TBAC showed extremely high loss while the loss of other films was quite low in the range of 0.02 to 0.05 at 1 kHz as shown in the inset graph. The low frequency loss of the film with

TBAC should be due to the remnant water. TBAC contained about 30 water

molecules per ammonium ion [12] most of which could not be removed from the

films according to the TGA analysis.

Figure 5.5 presents the P-E hysteresis loops of the PVDF films with the different

hydrated and hygroscopic chemicals. The hysteresis loop of the film with TBAC is

not shown here due to its large leakage current. Comparing Figure 5.5 with Figures

5.2 and 5.3, it could be found that the remnant polarization (P_r) of these PVDF films

increased with the promoted β phase. The β-phase dominant film derived from the

solution with $Al(NO_3)_3 \cdot 9H_2O$ possessed the largest P_r.
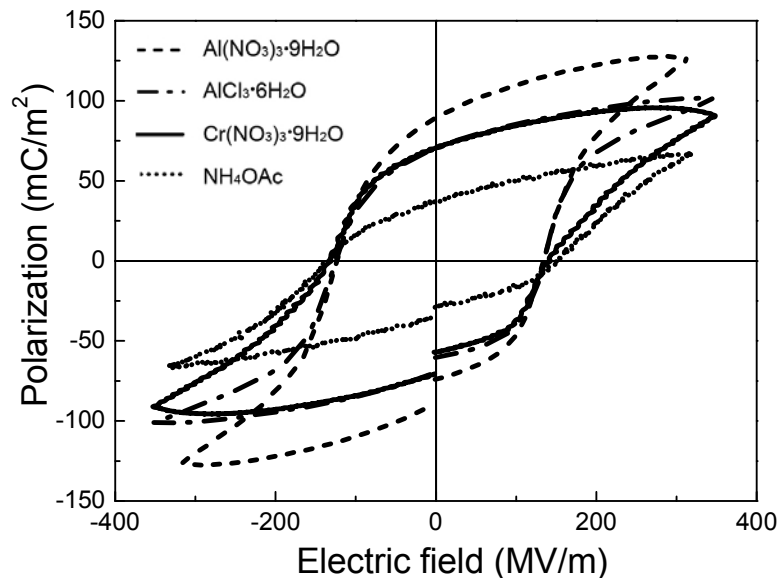
Figure 5.5   P-E hysteresis loops of PVDF films with (a) $Al(NO_3)_3 \cdot 9H_2O$; (b) $AlCl_3 \cdot 6H_2O$;
(c) $Cr(NO_3)_3 \cdot 9H_2O$; and (d) NH_4OAc. The concentration of chemical in PVDF is 4 wt%.

Although TBAC exhibited the strongest β-phase promotion ability here, it was not an

appropriate additive for producing the PVDF films for ferroelectric and piezoelectric

applications because of the remnant water in the films and the resulting large leakage current and dielectric loss. Instead, $Al(NO_3)_3 \cdot 9H_2O$ may be one of the ideal candidates because it can retain enough water at the crystallization temperature of PVDF to induce the formation of β phase, and also the water can be completely removed from the film during the subsequent annealing treatment at a further elevated temperature without leading to large leakage current and dielectric loss. We thus further investigated the effects of introducing $Al(NO_3)_3 \cdot 9H_2O$ of different amounts in the precursor solution on the structure and properties of the resulting PVDF films.

5.3.1.2 PVDF films with $Al(NO_3)_3 \cdot 9H_2O$

Structure of PVDF films with $Al(NO_3)_3 \cdot 9H_2O$

Figure 5.6 presents the FTIR spectra of the PVDF films with different concentrations of $Al(NO_3)_3 \cdot 9H_2O$. The film with only 1 wt% $Al(NO_3)_3 \cdot 9H_2O$ had a mixed crystalline structure of α and β phases, and the α phase was suppressed with further increasing the concentration of $Al(NO_3)_3 \cdot 9H_2O$ to 2 wt% and 4 wt%. The PVDF films with 8 wt% and 16 wt% $Al(NO_3)_3 \cdot 9H_2O$ exhibited almost complete β-phase crystalline structure, as shown in Figure 5.6. The XRD results in Figure 5.7 are consistent with the FTIR, in which the strong β(110)(200) peak at 20.8° indicated the β-phase crystalline structure of the PVDF films and the α phase was suppressed with increasing the concentration of $Al(NO_3)_3 \cdot 9H_2O$ from 1 wt% to 16 wt%.
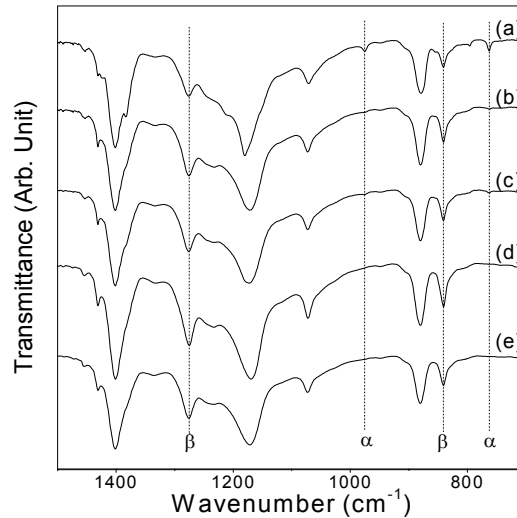
Figure 5.6 FTIR spectra of the PVDF films with Al(NO₃)₃·9H₂O of different concentrations introduced in the precursor solutions: (a) 1 wt%; (b) 2 wt%; (c) 4 wt%; (d) 8 wt%; and (e) 16 wt%. The unmarked peaks are common to both α and β phases.
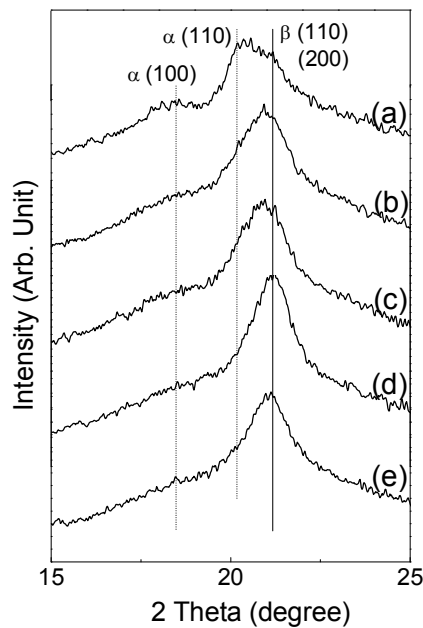
Figure 5.7 XRD patterns of the PVDF films with Al(NO₃)₃·9H₂O of different concentrations introduced in the precursor solutions: (a) 1 wt%; (b) 2 wt%; (c) 4 wt%; (d) 8 wt%; and (e) 16 wt%.

Surface morphology of PVDF films with Al(NO₃)₃·9H₂O

The surface morphology of the obtained PVDF films with Al(NO₃)₃·9H₂O was

shown in Figure 5.8 in comparison with the previously reported PVDF films with

$Mg(NO_3)_2 \cdot 6H_2O$. The PVDF films with $Mg(NO_3)_2 \cdot 6H_2O$ as reported before had extremely rough surface with lots of protruded irregular particles, which contained partially dehydrated $Mg(NO_3)_2 \cdot xH_2O$ as it could not dehydrate during the film annealing, as shown in Figure 5.8(a) and 5.8(b). Although there were spots observed on the surface, the PVDF films with $Al(NO_3)_3 \cdot 9H_2O$ were much smoother. According to the thermal analysis results, $Al(NO_3)_3 \cdot 9H_2O$ completely dehydrated and decomposed in the annealing treatment. The observed flat spots might be attributed to the residuals from the decomposed $Al(NO_3)_3 \cdot 9H_2O$. The decomposition of $Al(NO_3)_3 \cdot 9H_2O$ have prevented water absorption with time and thus stable electrical properties were obtained. In contrast, $Mg(NO_3)_2 \cdot 6H_2O$ was just partially dehydrated and $Mg(NO_3)_2$ was not decomposed, and so water was retained in the PVDF film and more water was absorbed with time. Thus, the electrical properties of the films with $Mg(NO_3)_2 \cdot 6H_2O$ were deteriorated.
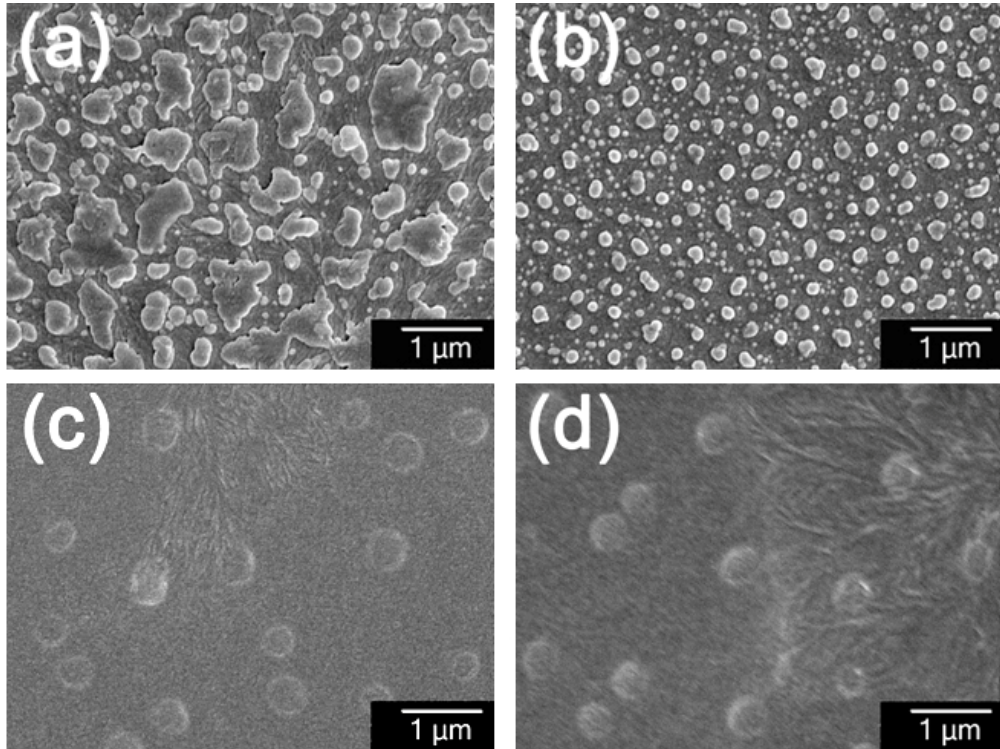
**Figure 5.8 FESEM images of the surfaces of the PVDF films: (a) with 4 wt%
$Mg(NO_3)_2 \cdot 6H_2O$, before annealing; (b) with 4 wt% $Mg(NO_3)_2 \cdot 6H_2O$, after annealed at
135°C;[13] (c) with 4 wt% $Al(NO_3)_3 \cdot 9H_2O$, before annealing; and (d) with 4 wt%
$Al(NO_3)_3 \cdot 9H_2O$, after annealed at 135°C.**

Electrical properties of PVDF films with $Al(NO_3)_3 \cdot 9H_2O$

Dielectric measurement showed that the PVDF film with as high as 16 wt%
$Al(NO_3)_3 \cdot 9H_2O$ introduced in the solution still exhibited very low dielectric loss
(0.0268, 1 kHz, not shown), which indicated the advantage from the complete
dehydration of $Al(NO_3)_3 \cdot 9H_2O$. Figure 5.9 presents the P-E hysteresis loops of
PVDF films with different concentrations of $Al(NO_3)_3 \cdot 9H_2O$. The remnant
polarization P_r increased with the concentration of $Al(NO_3)_3 \cdot 9H_2O$ from 1 to 4 wt%,
as shown in Figure 5.9. A high P_r of 89.1 mC/m^2 was obtained with the PVDF film
with 4 wt% $Al(NO_3)_3 \cdot 9H_2O$, which is even larger than the reported values for most

of the stretched samples. However, no substantial increase in P_r was observed with $Al(NO_3)_3 \cdot 9H_2O$ further increased to 8 and 16 wt%.

The piezoelectric coefficient d_{33} of the PVDF films with different concentrations of $Al(NO_3)_3 \cdot 9H_2O$ were measured under a unipolar ac signal of 10 V at 10 kHz. The PVDF film with 8 wt% $Al(NO_3)_3 \cdot 9H_2O$ exhibited the highest effective piezoelectric coefficient d_{33} value, -14.5pm/V. It should be noted that the d_{33} value was calculated without taking into account the clamping effect of the substrate. From numerical simulation after taking into account the elastic constraint of the substrate to the much softer PVDF film, the actual d_{33} value was -30.8 pm/V, which is similar to that of the uniaxially stretched bulk PVDF. Figure 5.10 presents a three-dimensional drawing of the instantaneous vibration data when the displacement magnitude of the PVDF film with 8 wt% $Al(NO_3)_3 \cdot 9H_2O$ reaches the maximum under the sine wave electrical driving at 10 kHz.
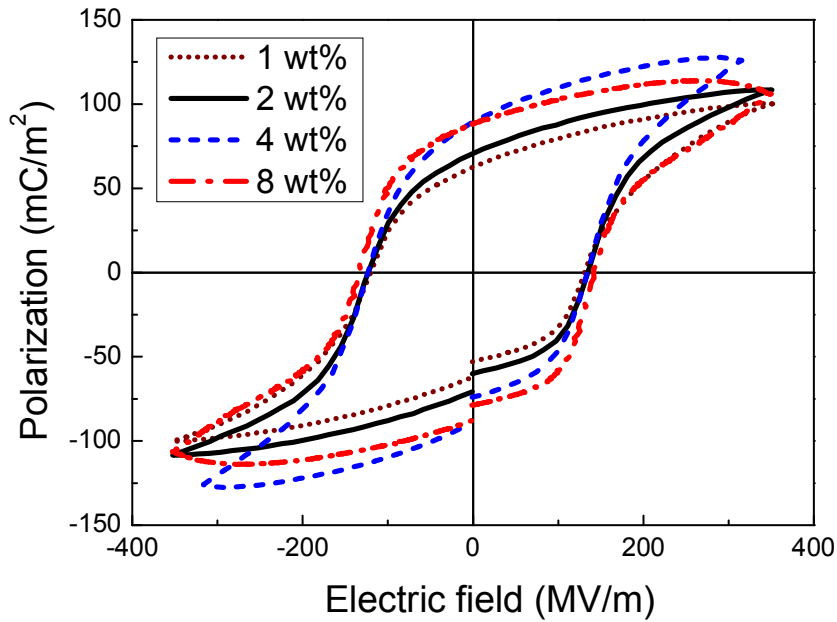
Figure 5.9 P-E hysteresis loops of the PVDF films with different concentrations of Al(NO₃)₃·9H₂O.
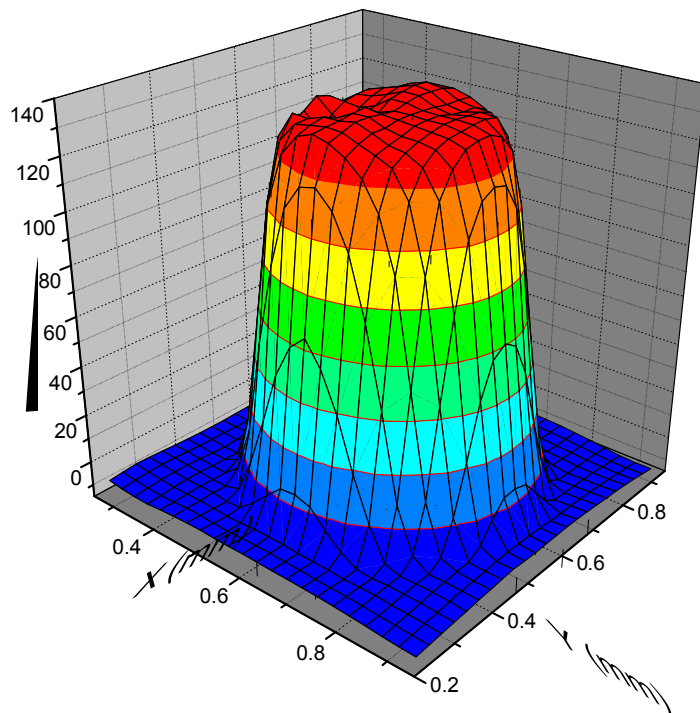
Figure 5.10 The 3-dimensional graph of the vibration data when the displacement of the PVDF film with 8 wt% Al(NO₃)₃·9H₂O reaches the maximum magnitude under the sine wave electrical driving at 10 kHz. The central protruding area is the electrically excited area under the Au electrode, whereas the flat surrounding area is the PVDF film without the top electrode cover.

5.3.2 PVDF ultrathin film by LB deposition

The FTIR spectra of the PVDF homopolymer films prepared by LB deposition and spin-coating are presented in comparison in Figure 5.11. It is evident that the PVDF LB film crystallized into the β phase, with characteristic absorption bands at 844 and 1286 cm^{-1} in the FTIR spectrum while the film prepared by spin-coating process was in α phase with characteristic absorption band at 976 cm^{-1}. The PVDF LB film exhibits a dense and homogenous surface morphology and appears to be polar β phase. Hence, LB deposition demonstrated a simple and convenient way for obtaining high-quality ferroelectric β-phase PVDF homopolymer thin films.
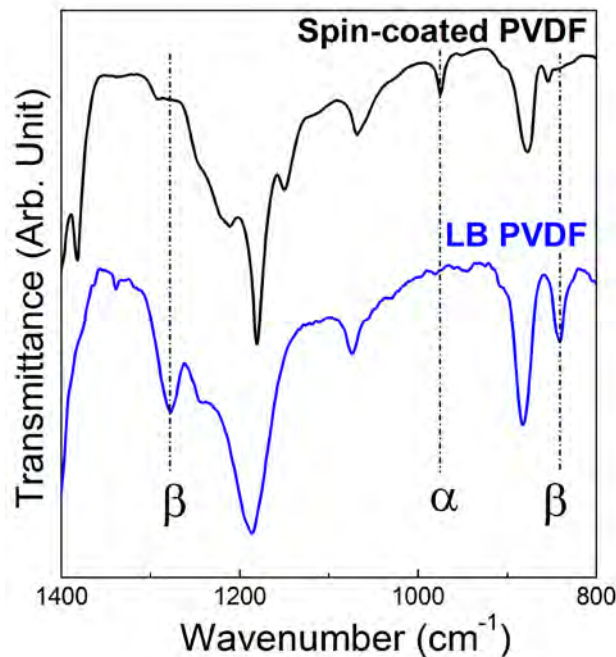
Figure 5.11 FTIR spectra of the PVDF thin films prepared by LB deposition and spin-coating process. The unmarked peaks are common for both α and β phases.

Mechanism of β-phase promotion by LB deposition

According to the above characterizations, the PVDF ultrathin film fabricated by LB deposition is β phase. It is hypothesized that during the LB deposition, the water subphase (on which the PVDF molecules are dispersed) could promote the β-phase crystals by the effect of hydrogen bonds due to the unique film transfer process from the water surface to the substrate.

In conventional LB deposition, the interaction of water with molecules to be deposited is commonly utilized to achieve films with ordered molecular structure. Normally, the substances to be deposited are amphiphilic and thus the molecular layer at the air-water interface is oriented with the hydrophobic groups upwards to air and the hydrophilic groups downwards to the aqueous phase because of the strong interaction between the spread substance and water. During the LB deposition in this work, one or a few PVDF molecule layers were first formed on water by spreading the solution onto the water surface. According to the analyses, the O-H groups of water molecules could form hydrogen bonds with C-F groups of PVDF, as observed when hydrated salts introduced to spin-coated PVDF films. As a result of forming the hydrogen bonds for the LB films, the PVDF molecules on water surface should be oriented with C-F groups downwards to water, as schematically illustrated in Figure 5.12(a), which is similar to the all-trans molecular conformation in the β-phase PVDF.
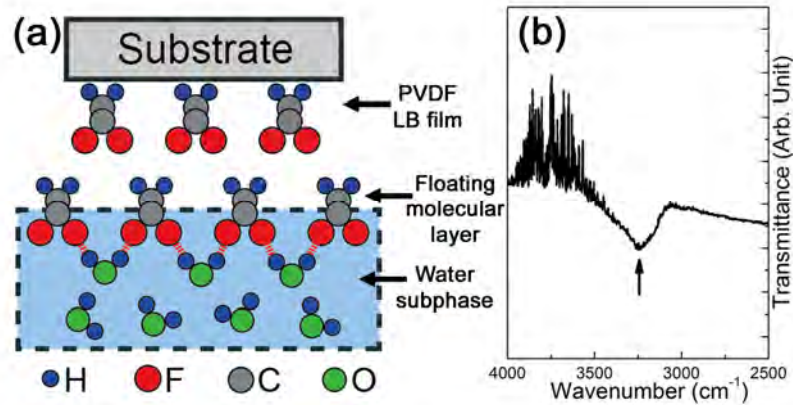
Figure 5.12 (a) Schematic illustration of the orientation of the PVDF molecules on water surface and the subsequent transfer to a substrate to form the LB film. The PVDF molecules are drawn with the chain perpendicular to the paper. (b) The FTIR spectrum of the PVDF LB film. The arrowed peak denotes the absorption band of O-H groups interacted with PVDF molecules through hydrogen bonds.

Figure 5.12(b) shows the FTIR spectrum of the PVDF LB film in the wavenumber range of 2500-4000 cm^{-1}, which clearly shows an absorption band at wavenumber of 3235 cm^{-1}. The IR absorption bands at similar range were also observed in our previous study on spin-coated PVDF with hydrated salts as discussed. It was found that the broad absorption bands in the range of about 3180 to 3310 cm^{-1} is attributed to the stretching of O-H groups of water bonded with PVDF molecules. Such an absorption band slightly shifted toward a lower frequency compared to normal O-H groups as a result of the hydrogen-bond induced bond elongation. In this study, the absorption band at 3235 cm^{-1} in the FTIR spectrum of the PVDF LB film supports the existence of the hydrogen bonds between water and PVDF molecules. With the hydrogen bond formation, when the polymer chains were transferred from the water surface to the substrate during the LB deposition, the PVDF molecules could maintain the orientation and subsequently crystallize into the polar β-phase structure.

Dipole orientation in the LB film

The mechanism for promoting the β phase as proposed above suggests that there may be specific preference of the dipole orientation in the resulting PVDF LB films. To understand the dipole orientation and confirm the proposed mechanism, we examined the PVDF LB films with PFM, in which the phase of the piezoresponse reflects the correlation of the polarization orientation and the direction of the applied electric field. The LB film was poled by the PFM tip at different voltages (+10 V and -10 V) over an area of 6×6 μm^2, followed by PFM scans covering the poled and surrounding un-poled areas. When the LB film was poled by a negative field, the phase angle difference between the central poled area and the surrounding un-poled area was significant, as shown in Figures 5.13(b) and (c), indicating that the dipoles were re-oriented by the poling electric field. In contrast, when the films were poled by positive voltage, there was no observable phase angle difference between the poled and the un-poled areas, as shown in Figures 5.13(a) and (c), suggesting that there was no substantial dipole reorientation induced by the poling electric field. The piezoresponse phase results clearly showed that the dipoles in the PVDF LB film were aligned with strong preference in which the C-F groups were aligned towards the surface of the PVDF film, as illustrated in Figure 5.13(d). Thus the PVDF LB film was self-polarized and almost no dipole re-orientation occurred during the poling process with the positive voltage applied. The polarization orientation as determined with PFM is consistent with the expectation on the basis of the proposed β-phase promotion mechanism by the water subphase during the LB deposition, as

illustrated in Figure 5.12(a).
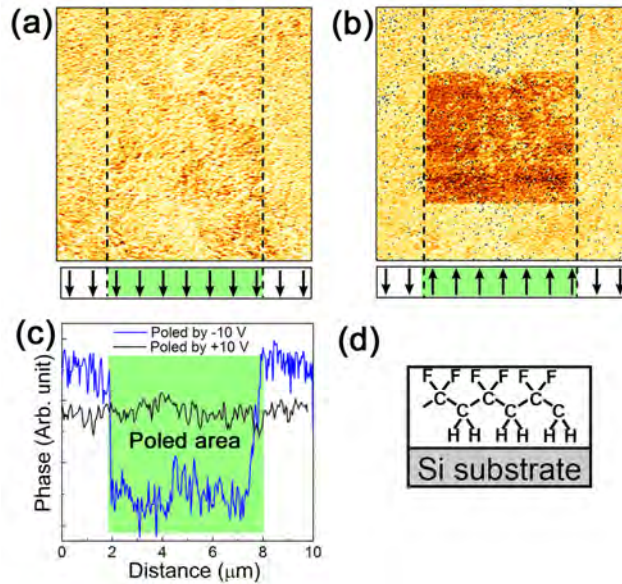
Figure 5.13   (a) and (b): piezoresponse phase images of PVDF LB films with central area poled at +10V and -10V, respectively. The arrows below the PFM images show the dipole orientation in the poled (shaded) and the surrounding un-poled areas. The total scanned area is 10×10 μm², and the central poled area is 6×6 μm². (c) Comparison of the piezoresponse phase profiles across the poled and un-poled areas of the LB film, with the different poling voltages. (d) Schematic illustration of the orientation of a PVDF molecule in the LB film.

5.4 Conclusions

Two approaches were investigated to promote the β phase formation in PVDF homopolymer thin films, namely incorporation of hydrated and hydroscopic chemicals, and layer by layer Langmuir-Blodgett deposition. Both approaches rely on the hydrogen bond interaction between water and PVDF polymer chain to promote β phase.

The introduction of several hydrated and hygroscopic chemicals in the precursor solutions for preparing PVDF thin films was shown to result in retention of a substantial amount of water in the film during the crystallization process. This effectively promoted the ferroelectric β phase while suppressing the non-polar α phase. An important prerequisite is that the hydrated salt must have a dehydration temperature higher than the crystallization temperature of the PVDF films but completely dehydrated in the following annealing process to avoid larger leakage current and dielectric loss caused by water. One of the hydrated chemicals as examined in this work, $Al(NO_3)_3 \cdot 9H_2O$, well met the above requirements. With $Al(NO_3)_3 \cdot 9H_2O$ of appropriate amount introduced to the precursor solution, the resulting β-phase dominant ferroelectric PVDF thin films exhibited smooth morphology, low dielectric loss, high remnant polarization of 89.1 mC/m^2, and large effective piezoelectric coefficient d_{33} of -14.5 pm/V (under the clamping of the substrate).

The mechanism of β phase formation by hydrogen bonds is further studied in PVDF ultra thin films fabricated using LB deposition method. It was found that LB deposition process led to the direct formation of ferroelectric β phase in PVDF homopolymer ultra-thin films, in which the molecular chains were parallel to the substrates and the dipoles were aligned perpendicular to the substrates. Theoretical analysis and experimental results showed that the mechanism of forming the β phase

and the dipole orientation were attributed to the hydrogen bonds between the PVDF molecules and water formed through the unique LB deposition process.

References

[1]   E. Fukada, "History and recent progress in piezoelectric polymers," Ieee Transactions on Ultrasonics Ferroelectrics and Frequency Control, vol. 47, pp. 1277-1290, Nov 2000.

[2]   V. Sencadas, R. Gregorio, and S. Lanceros-Mendez, "alpha to beta Phase Transformation and Microstructural Changes of PVDF Films Induced by Uniaxial Stretch," Journal of Macromolecular Science Part B-Physics, vol. 48, pp. 514-525, 2009.

[3]   J. Humphreys, E. L. V. Lewis, I. M. Ward, E. L. Nix, and J. C. McGrath, "A STUDY OF THE MECHANICAL ANISOTROPY OF HIGH-DRAW, LOW-DRAW, AND VOIDED PVDF," Journal of Polymer Science Part B-Polymer Physics, vol. 26, pp. 141-158, Jan 1988.

[4]   T. Hattori, M. Kanaoka, and H. Ohigashi, "Improved piezoelectricity in thick lamellar beta-form crystals of poly(vinylidene fluoride) crystallized under high pressure," Journal of Applied Physics, vol. 79, pp. 2016-2022, Feb 1996.

[5]   R. Gregorio and M. Cestari, "EFFECT OF CRYSTALLIZATION TEMPERATURE ON THE CRYSTALLINE PHASE CONTENT AND MORPHOLOGY OF POLY(VINYLIDENE FLUORIDE)," Journal of

Polymer Science Part B-Polymer Physics, vol. 32, pp. 859-870, Apr 15 1994.

[6]   M. Benz, W. B. Euler, and O. J. Gregory, "The role of solution phase water on the deposition of thin films of poly(vinylidene fluoride)," Macromolecules, vol. 35, pp. 2682-2688, Mar 26 2002.

[7]   X. J. He and K. Yao, "Crystallization mechanism and piezoelectric properties of solution-derived ferroelectric poly(vinylidene fluoride) thin films," Applied Physics Letters, vol. 89, Sep 2006.

[8]   S. Chen, K. Yao, F. E. H. Tay, and C. L. Liow, "Ferroelectric poly(vinylidene fluoride) thin films on Si substrate with the beta phase promoted by hydrated magnesium nitrate," Journal of Applied Physics, vol. 102, Nov 15 2007.

[9]   K. Yao and F. E. H. Tay, "Measurement of longitudinal piezoelectric coefficient of thin films by a laser-scanning vibrometer," Ieee Transactions on Ultrasonics Ferroelectrics and Frequency Control, vol. 50, pp. 113-116, Feb 2003.

[10] P. Nallasamy and S. Mohan, "Vibrational spectroscopic characterization of form II poly(vinylidene fluoride)," Indian Journal of Pure & Applied Physics, vol. 43, pp. 821-827, Nov 2005.

[11] K. Hermansson, "A NEUTRON-DIFFRACTION DETERMINATION OF THE STRUCTURE OF DEUTERATED ALUMINUM NITRATE NONAHYDRATE, $AL(NO_3)_3.9D_2O$," Acta Crystallographica Section C-Crystal Structure Communications, vol. 39, pp. 925-930, 1983.

[12] H. Nakayama, "SOLID-LIQUID AND LIQUID-LIQUID

PHASE-EQUILIBRIA IN THE SYMMETRICAL TETRAALKYLAMMONIUM HALIDE-WATER SYSTEMS," Bulletin of the Chemical Society of Japan, vol. 54, pp. 3717-3722, 1981.

Chapter 6   Solution-derived ferroelectric PVDF homopolymer nanotube array in AAM template

6.1 Introduction

In the past decade, while the fabrication and device applications of one-dimensional nanostructures based on inorganic ferroelectric and piezoelectric materials [1-6] have been extensively studied, nanostructures based on ferroelectric polymers have also attracted considerable research interests due to their light-weight, flexible and non-toxic properties [7-10]. As discussed in the previous chapters, we have prepared polymeric nanotube array with much enhanced capacitance based on P(VDF-TrFE); furthermore, mechanical energy harvesting from piezoelectric P(VDF-TrFE) nanotube array have been theoretically analyzed and experimentally demonstrated. The analyses and experimental results indicate that the flexible ferroelectric P(VDF-TrFE) nanotube array has great potential in many applications including non-volatile memories, high density capacitors, piezoelectric sensors and energy harvesting devices.

Compared to the copolymer P(VDF/TrFE), PVDF homopolymer has many advantages, such as larger intrinsic polarization, higher Curie temperature, higher breakdown strength, significantly lower cost and ready availability. However, the non-polar α phase of PVDF homopolymer is thermodynamically most stable. In Chapter 4, PVDF nanotube array has been fabricated in AAM template by hot-press

method and shown to be α phase. In contrast to P(VDF-TrFE) nanotube array, the non-polar α-phase dominated PVDF nanotube array has no substantial piezoelectric response.

Among the four phases of PVDF, β phase exhibits the most superior ferroelectric and piezoelectric properties. Hence, it is attractive to fabricate nanostructures based on β-phase PVDF homopolymer, which may obtain comparable ferroelectric and piezoelectric properties compared to P(VDF-TrFE) but much significantly lower cost. Some effective methods to achieve the β-phase PVDF homopolymer include mechanical stretching,[11] use of polar solvents,[12,13] introducing high pressure treatment,[14] rapid thermal treatment[15] and melt quenching.[16] However, while PVDF nanotubes and nanorods of non-polar α phase [17] and minor polar γ phase [18] had been fabricated by template wetting process, direct fabrication of β-phase PVDF nanotube in template has not been reported yet.

In this work, solution derived ferroelectric β-phase PVDF homopolymer nanotube with highly ordered AAM as template has been fabricated. The mechanism of β phase formation by the hydrogen bonding interaction between hydroxyl groups on AAM surface and PVDF chain was identified, similar to the β phase formation mechanism in PVDF homopolymer films [19-22] that was discussed in Chapter 5. Significantly improved piezoelectric performance properties were demonstrated over macroscopic area with a laser scanning vibrometer. The fabricated β-phase PVDF

nanotube array showed a high remnant polarization of 82.4 mC/m^2, and large effective piezoelectric coefficient d_{33} of -19.2 pm/V. The unique properties and scalable solution fabrication process of β-phase PVDF nanotube array indicated that the nanotube array might have great potential in low cost, large area device applications.

6.2 Experimental

6.2.1 Fabrication of solution-derived PVDF nanotubes in AAM template

As discussed in previous chapters, AAM template with a pore size of 250-300 nm, and depth of 2-3 μm (Figure 6.1(a)) was fabricated using a two-step anodizing method. The PVDF solution was prepared at concentration of 10 wt% with the solvent of dimethylformamide (DMF)/acetone (1:1 in volume). Figure 6.1 shows the template-based fabrication of solution-derived PVDF nanotube. The PVDF solution was prepared at concentration of 10 wt% with the solvent of dimethylformamide (DMF)/acetone (1:1 in volume). The AAM template was immersed in the PVDF solution, and then pumped to vacuum to remove the air trapped inside the template. The template with PVDF solution was dried at 80 °C. PVDF nanotube array formed inside the AAM template, and the solution left on AAM surface formed a residual PVDF film (Figure 6.1(b)). The AAM template was then etched off in 4 mol/L NaOH solution to release the nanotubes (Figure 6.1(c)). Gold electrodes were deposited on both top and bottom sides of the released nanotube array by sputtering for electrical testing. The released nanotube array was attached on gold-coated

substrate with silver epoxy for support (Figure 6.1(d)). For comparison purpose, PVDF spin-coated films were formed by depositing the same PVDF solution on aluminum-coated silicon substrates followed by immediate drying on a hotplate at 80 °C for 10 minutes. Hot-pressed PVDF nanotubes were fabricated as follows: the PVDF solution was dipped on the AAM template surface and dried at 80 ºC to form a layer of polymer. The AAM with polymer was then heated to 250 ºC, which was above the melting point of PVDF, and a pressure of 5 MPa was applied. PVDF nanotube array was formed as the polymer melt wet the inner surface of AAM template.
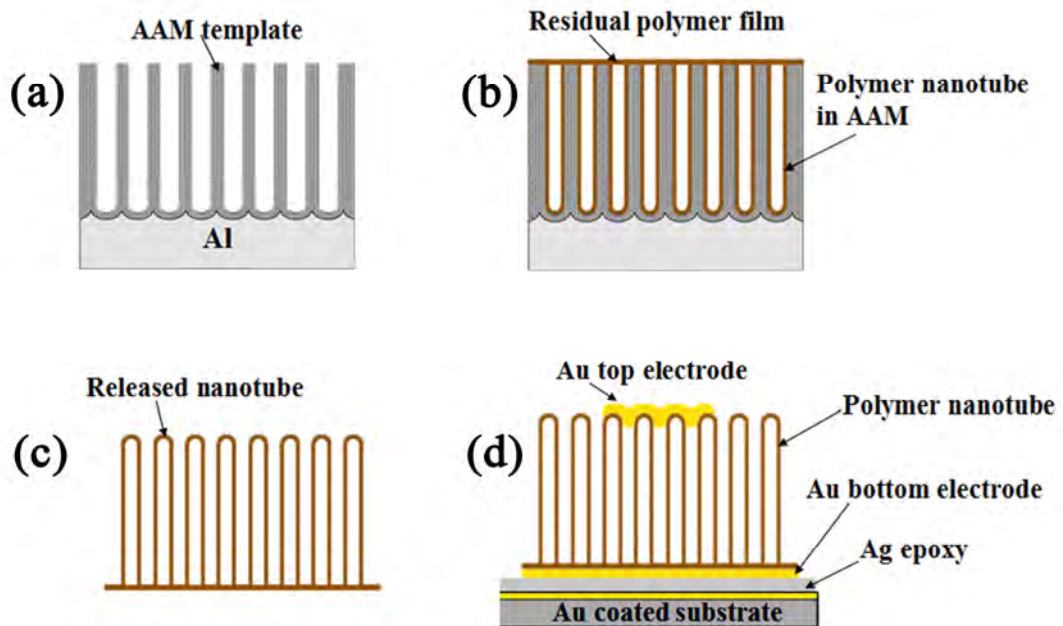
Figure 6.1 Schematic illustration of: (a) bare AAM template; (b) PVDF nanotube in AAM template with a residual PVDF film on top; (c) released PVDF nanotube array; (d) released PVDF nanotube array with electrodes for electrical testing

6.2.2 Characterization of PVDF nanotubes

The morphology of AAM template and PVDF nanotube array was observed with

field emission scanning electron microscopy (FESEM, JSM-6700F, JEOL). The released nanotube was also examined with high-resolution transmission electron microscope (Philips CM300 FEGTEM). The crystalline structures of PVDF nanotubes were examined with x-ray diffraction (XRD) system (D8-ADVANCE, Bruker AXS GmbH, Karlsruhe) and Fourier transform infrared spectroscopy (FTIR) (Spectrum 2000, Perkin Elmer, Norwalk, CT, US) in the reflection mode. The polarization and electric field (P−E) hysteresis loops were measured with a standard ferroelectric testing unit (Precision Premier II, Radiant Technologies) connected to a high-voltage interface. The effective piezoelectric constant d_{33} for the PVDF nanotubes was measured with a laser scanning vibrometer (OFV-3001-SF6, PolyTech GmbH).

6.3 Results and discussion

6.3.1 Morphology and crystal structure of PVDF nanotubes

Figure 6.2 shows the morphology of the AAM template and the PVDF nanotubes observed by SEM and TEM. Figure 6.2(a) shows the top surface of the self-prepared AAM template with pore size of about 250-300 nm. PVDF solution spontaneously wet the inner surface of AAM template because of its relative high surface energy. The solvent was evaporated and PVDF nanotubes were formed in AAM template with a residual PVDF film on top. Figure 6.2(b) shows the top view of the released PVDF nanotube array when the template was etched off. The nanotubes duplicated

the one-end sealed shape of AAM nanochannels, and were linked at the other end by the residual PVDF film. The released PVDF nanotubes were free-standing but tended to form bundles because PVDF is relatively soft. After the residual PVDF film was removed, the PVDF nanotubes were dispersed in water for TEM characterization. The hollow structure of PVDF nanotube is shown in Figure 6.2(c), which indicates the thickness of nanotube wall is about 15 nm.
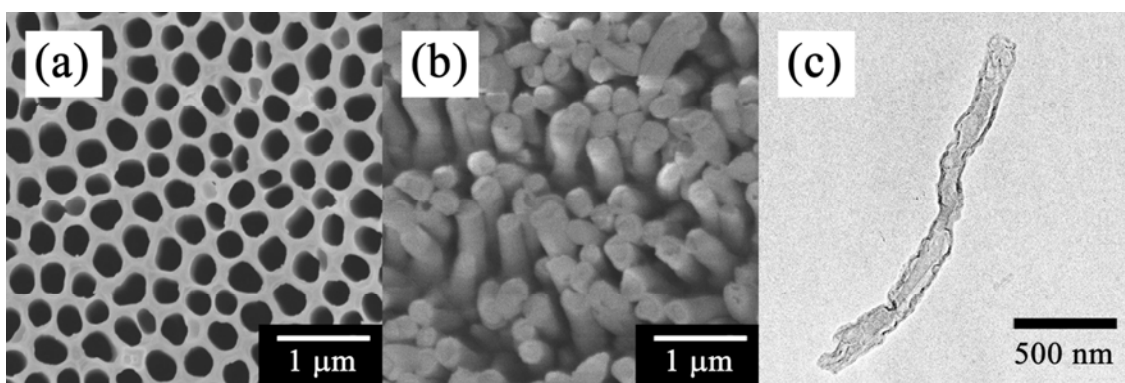
Figure 6.2 (a) SEM image of AAM template, top view; (b) SEM image of released PVDF nanotubes; (c) TEM image of single nanotube.

The crystalline phase of the solution-derived PVDF nanotubes was characterized with XRD and FTIR. In comparison, the crystalline phases of the spin-coated PVDF homopolymer film and hot-pressed PVDF nanotubes were also observed. Figure 6.3(a) shows the FTIR spectra of the nanotube and film samples. The solution-derived PVDF nanotubes were β-phase dominant with characteristic absorption bands at 842 and 1274 cm^{-1}, while the spin-coated film and hot-pressed nanotubes were α phase with characteristic absorption bands at 764, 795, 975, 1150 and 1210 cm^{-1}. The crystalline phase of PVDF film and nanotubes was further confirmed by XRD. As shown in Figure 6.3(b), the solution-derived PVDF

nanotubes had strong β phase peak at 20.4° corresponding to the diffraction planes (110)(200), while the spin-coated PVDF film and hot-pressed nanotubes had diffraction peaks at 18.1° and 19.7° corresponding to the (100) and (110) crystal planes of the α phase, respectively. It should be noted that, as shown in Figure 6.3(b), the solution-derived PVDF nanotube sample also had minor α phase signal, probably from the α phase in the residual film of the sample.
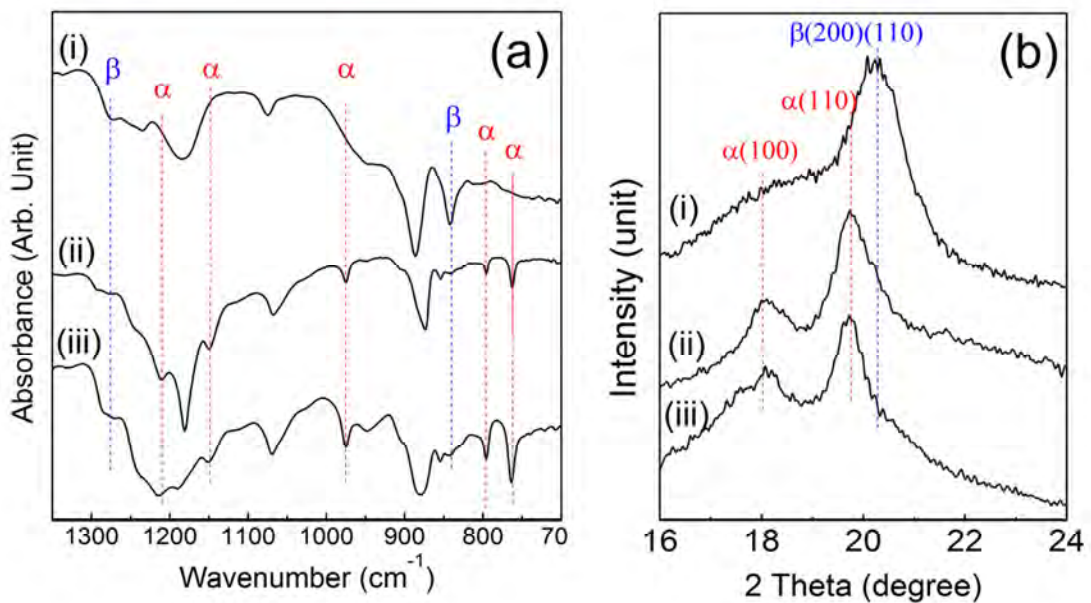
Figure 6.3 (a). FTIR spectra of: (i) solution-derived PVDF nanotubes, (ii) spin-coated PVDF film and (iii) hot-pressed PVDF nanotubes. The unmarked peaks are common for both α and β phases; (b). XRD spectra of: (i) solution derived PVDF nanotubes, (ii) spin-coated PVDF film and (iii) hot-pressed PVDF nanotubes.

6.3.2 Mechanism of PVDF β-phase promotion in AAM template

According to the above characterizations, the PVDF nanotubes fabricated by solution wetting in AAM template were β-phase, while the PVDF nanotubes fabricated by hot-pressing and the spin-coating PVDF films were α-phase. The

possible mechanism of β phase formation in the solution-derived PVDF nanotubes

will be discussed.

It has been proven that PVDF molecules could form intermolecular bonds with a

variety of molecules with high polar groups, which induced the formation of β phase

during crystallization. The polar groups may come from high polar solvents or

additives. β-phase PVDF has been achieved from DMF solution because of the

molecular interactions between PVDF and DMF. It has also been reported that

blending with carbon nanotubes enhanced the formation of β phase in PVDF, due to

the interaction of PVDF molecule and the surface functional groups of the carbon

nanotubes[9]. In our previous studies, hydrated salt was added in PVDF precursor

solution and the PVDF molecular chain would form hydrogen bonds with the

hydrated water introduced, inducing the formation of β phase [19-21]. β-phase

PVDF ultra-thin film was also fabricated by LB deposition. The C-F groups of

PVDF form hydrogen bonds with the O-H groups of water molecules in the LB

deposition.

The surface of AAM template usually has a large amount of hydroxyl groups [23,

24], which could become functional groups in the fabrication of nanostructures in

AAM template. Figure 6.4(a) shows the FTIR spectra of the bare AAM template and

PVDF nanotubes formed in template. The broad IR absorption band in the range of

about 3120 to 3660 cm^{-1} of bare AAM template sample (Figure 6.4(a),(i)) is due to

the stretching of surface O-H groups. In contrast, this absorption band is absent in the hot-pressed PVDF nanotube sample. In the hot-press process, the polar solvent was evaporated and the AAM surface hydroxyl group would disappear in the relative high temperature (250 ^{o}C) (Figure 6.4(a),(ii)), thus α phase PVDF nanotubes were fabricated from PVDF melt. As solution-derived PVDF nanotubes were formed in AAM template, the absorption band slightly shifted to lower frequencies, suggesting that hydrogen bonds were formed between PVDF polymer chain and AAM surface hydroxyl groups. With the hydrogen bonds formed, the O-H bonds were elongated and thus shifted to lower vibrational frequencies (Figure 6.4(a),(iii)).

As schematically illustrated in Figure 6.4(b), the hydrogen bonds formed would restrict the fluorine atoms in PVDF polymer chain to a certain extent, thus leading to the formation of all-trans β phase in the PVDF nanotube fabricated in AAM template. It may be expected that the β phase induction effect also applies to the spin-coated PVDF film on aluminum substrate, since there is always a layer of alumina on aluminum surface. However, the effect weakens rapidly as the thickness of PVDF layer increased since the interaction mechanism mainly exists at the interface of PVDF solution and the solid surface with polar groups. Hence, the PVDF nanotube with thickness of 50 nm was β-phase dominant while the 1-μm-thick spin-coated PVDF film on aluminum substrate was α-phase dominant.
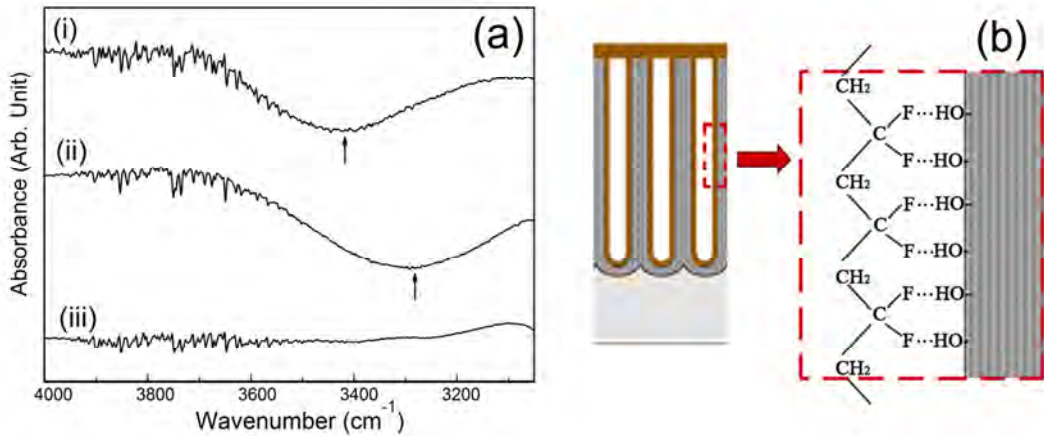
Figure 6.4 (a) The FTIR spectra of (i) bare AAM template, (ii) solution-derived PVDF nanotubes in AAM template and (iii) hot-pressed PVDF naotubes in AAM template; the arrows show the absorption band of O-H groups on AAM surface in (i) and O-H groups interacted with PVDF molecules through hydrogen bonds in (ii); (b) Schematic illustration of the interaction between AAM surface hydroxyl groups and PVDF molecule that induces the formation of all-trans β phase in solution-derived PVDF nanotube.
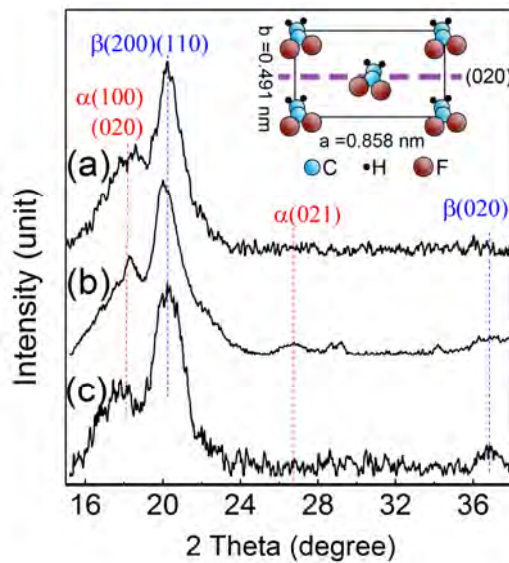
Figure 6.5 XRD patterns of: (a) 10 wt% solution-derived PVDF nanotubes; (b) 30 wt% solution-derived PVDF nanotubes; (c) spin-coated PVDF thin film with incorporated hydrate salt Al(NO3)3•9H2O for β phase promotion. Inset shows a schematic of the PVDF β phase crystal structure with the (020) plane indicated for clarity.

In order to further investigate this hypothesis, a PVDF nanotube array with more concentrated PVDF solution (30 wt% as compared to 10 wt% for the original sample) has been fabricated to achieve larger wall thickness. In this control sample, the

surface effect is reduced; hence it may be expected to see a greater proportion of α phase. Figure 6.5 shows a comparison between the XRD patterns of the original PVDF nanotubes (10 wt% PVDF solution, Figure 6.5(a)) and the control sample with thicker walls (30 wt% PVDF solution, Figure 6.5(b)). It is clear that the α phase peaks are much sharper and more pronounced in the control sample, thus providing further evidence for the above mentioned hypothesis.

To obtain more information on the polymer chain orientation in the nanotube array, the XRD range of 2θ angles has been expanded to 38° in order to observe the β phase (020) peak at 36.6° (JCPDS no. 42-1649). If the polymer chains are oriented as shown schematically in Figure 6.4(b), the (020) planes will be parallel to the nanotube longitudinal direction and perpendicular to the plane of the substrate, and will only be diffracted by X-rays close to grazing incidence (ψ around 0° or 180°). Hence, they can hardly be detected by the XRD detector with a limited field of view in the ψ direction (~45° to 135°, with 90° being perpendicular to the plane of the substrate). Indeed, the XRD pattern in Figure 6.5(a) shows the absence of such a peak for the solution-derived PVDF nanotube array. For comparison, a spin-coated PVDF thin film was fabricated with incorporated hydrate salt $Al(NO_3)_3 \cdot 9H_2O$ for β phase promotion. The XRD pattern for the spin-coated thin film (Figure 6.5(c)) clearly shows the (020) peak, which should be expected for such a sample with unoriented polymer chains. This provides further evidence for the proposed β phase formation mechanism.

6.3.3 Ferroelectric and piezoelectric properties of β-phase PVDF nanotube array

Figure 6.6(a) shows the P-E hysteresis loop of the PVDF nanotube array. The nanotube sample showed a high remnant polarization P_r 82.4 mC/m^2, which was comparable to β-phase PVDF films. The result confirmed that the PVDF nanotube array was β-phase dominant and exhibited ferroelectricity. However, the coercive field E_c of PVDF nanotube was much higher (796 MV/m) compared with 1-μm-thick PVDF films (115 MV/m) [20,21], indicated that the dipoles in PVDF nanotube were much more difficult to switch.

The effective piezoelectric coefficient d_{33} of the released solution-derived PVDF nanotube array was measured by a laser scanning vibrometer [25] under a unipolar ac signal of 10 V at 5 kHz. Figure 6.6(b) presents a three-dimensional drawing of the instantaneous vibration data when the displacement magnitude of the PVDF nanotube sample reaches the maximum under the sine driving wave. The effective piezoelectric coefficient d_{33} of the PVDF nanotube array was found to be as high as -19.2 pm/V, which is 32% higher than the previous results on 1-μm-thick β-phase PVDF thin films on substrate (-14.5 pm/V). It suggests that, for the case of nanotube, the clamping effect of substrate is not as strong as the films, thus the nanotube samples exhibits larger effective piezoelectric coefficient d_{33} than the film samples.
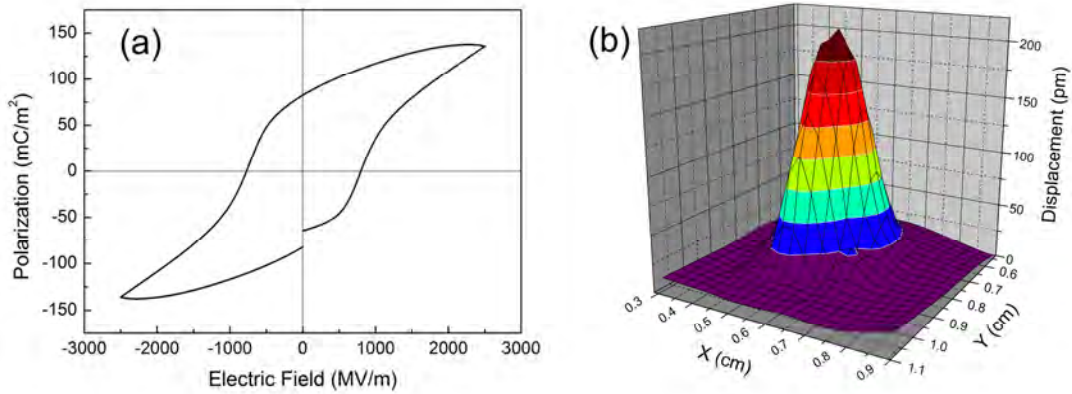
Figure 6.6 (a) P-E hysteresis loop of the released PVDF nanotube array; (b) the 3-dimensional drawing of the instantaneous vibration data when the displacement magnitude of the PVDF nanotube sample reaches the maximum under the sine driving wave at 5 kHz; the central protruding area is the electrically excited area under the Au electrode, whereas the flat surrounding area is the PVDF film without the top electrode cover.

6.4 Conclusions

In summary, solution-derived PVDF homopolymer nanotube array has been fabricated in AAM template and shown to be β phase dominant. Theoretical analysis and experimental results indicated that the hydrogen bonds between hydroxyl groups at AAM surface and PVDF molecules at the interface of PVDF solution and AAM surface induced the formation of β phase. The β-phase PVDF nanotube array showed a high remnant polarization of 82.4 mC/m^2, and large effective piezoelectric coefficient d_{33} of -19.2 pm/V (under the clamping of the substrate), which was substantially larger than 1-μm-thick PVDF film on substrate with β phase. As PVDF has a significantly lower cost than P(VDF-TrFE), the results in this chapter show that low cost piezoelectric polymer nanotubes can be produced by the scalable

solution process using AAM templates and thus they can be applied for large area device application at low cost.

Reference

[1]   Z. L. Wang, "Piezoelectric nanostructures: From growth phenomena to electric nanogenerators," *Mrs Bulletin,* vol. 32, pp. 109-116, Feb 2007.

[2]   P. M. Rorvik, T. Grande, and M. A. Einarsrud, "One-Dimensional Nanostructures of Ferroelectric Perovskites," *Advanced Materials,* vol. 23, pp. 4007-4034, Sep 2011.

[3]   M. Alexe, D. Hesse, V. Schmidt, S. Senz, H. J. Fan, M. Zacharias, and U. Gosele, "Ferroelectric nanotubes fabricated using nanowires as positive templates," *Applied Physics Letters,* vol. 89, Oct 2006.

[4]   X. D. Wang, J. H. Song, J. Liu, and Z. L. Wang, "Direct-current nanogenerator driven by ultrasonic waves," *Science,* vol. 316, pp. 102-105, Apr 2007.

[5]   M. Willander, O. Nur, Q. X. Zhao, L. L. Yang, M. Lorenz, B. Q. Cao, J. Z. Perez, C. Czekalla, G. Zimmermann, M. Grundmann, A. Bakin, A. Behrends, M. Al-Suleiman, A. El-Shaer, A. C. Mofor, B. Postels, A. Waag, N. Boukos, A. Travlos, H. S. Kwack, J. Guinard, and D. L. Dang, "Zinc oxide nanorod based photonic devices: recent progress in growth, light emitting diodes and lasers," *Nanotechnology,* vol. 20, Aug 2009.

[6]   J. Kim, S. A. Yang, Y. C. Choi, J. K. Han, K. O. Jeong, Y. J. Yun, D. J. Kim, S.

M. Yang, D. Yoon, H. Cheong, K. S. Chang, T. W. Noh, and S. D. Bu, "Ferroelectricity in highly ordered arrays of ultra-thin-walled Pb(Zr,Ti)O-3 nanotubes composed of nanometer-sized perovskite crystallites," *Nano Lett,* vol. 8, pp. 1813-1818, Jul 2008.

[7]   M. Rahimabady, S. T. Chen, K. Yao, F. E. H. Tay, and L. Lu, "High electric breakdown strength and energy density in vinylidene fluoride oligomer/poly(vinylidene fluoride) blend thin films," *Applied Physics Letters,* vol. 99, Oct 2011.

[8]   Z. J. Hu, M. W. Tian, B. Nysten, and A. M. Jonas, "Regular arrays of highly ordered ferroelectric polymer nanostructures for non-volatile low-voltage memories," *Nature Materials,* vol. 8, pp. 62-67, Jan 2009.

[9]   C. C. Hong, S. Y. Huang, J. Shieh, and S. H. Chen, "Enhanced Piezoelectricity of Nanoimprinted Sub-20 nm Poly(vinylidene fluoride-trifluoroethylene) Copolymer Nanograss," *Macromolecules,* vol. 45, pp. 1580-1586, Feb 2012.

[10]   S. Cha, S. M. Kim, H. Kim, J. Ku, J. I. Sohn, Y. J. Park, B. G. Song, M. H. Jung, E. K. Lee, B. L. Choi, J. J. Park, Z. L. Wang, J. M. Kim, and K. Kim, "Porous PVDF as effective sonic wave driven nanogenerators," *Nano Lett,* vol. 11, pp. 5142-7, Dec 14 2011.

[11]   V. Sencadas, R. Gregorio, and S. Lanceros-Mendez, "alpha to beta Phase Transformation and Microstructural Changes of PVDF Films Induced by Uniaxial Stretch," *Journal of Macromolecular Science Part B-Physics,* vol.

48, pp. 514-525, 2009.

[12]   R. Gregorio and M. Cestari, "EFFECT OF CRYSTALLIZATION TEMPERATURE ON THE CRYSTALLINE PHASE CONTENT AND MORPHOLOGY OF POLY(VINYLIDENE FLUORIDE)," *Journal of Polymer Science Part B-Polymer Physics,* vol. 32, pp. 859-870, Apr 15 1994.

[13]   R. Hasegawa, Takahash.Y, H. Tadokoro, and Y. Chatani, "CRYSTAL-STRUCTURES OF 3 CRYSTALLINE FORMS OF POLY(VINYLIDENE FLUORIDE)," Polymer Journal, vol. 3, pp. 600-&, 1972.

[14]   T. Hattori, M. Kanaoka, and H. Ohigashi, "Improved piezoelectricity in thick lamellar beta-form crystals of poly(vinylidene fluoride) crystallized under high pressure," *Journal of Applied Physics,* vol. 79, pp. 2016-2022, Feb 1996.

[15]   S. J. Kang, Y. J. Park, J. Sung, P. S. Jo, C. Park, K. J. Kim, and B. O. Cho, "Spin cast ferroelectric beta poly(vinylidene fluoride) thin films via rapid thermal annealing," Applied Physics Letters, vol. 92, Jan 2008.

[16]   S. J. Kang, Y. J. Park, I. Bae, K. J. Kim, H. C. Kim, S. Bauer, E. L. Thomas, and C. Park, "Printable Ferroelectric PVDF/PMMA Blend Films with Ultralow Roughness for Low Voltage Non-Volatile Polymer Memory," Advanced Functional Materials, vol. 19, pp. 2812-2818, Sep 2009.

[17]   Y. B. Li, M. J. Zheng, and L. Ma, "High-speed growth and photoluminescence of porous anodic alumina films with controllable

interpore distances over a large range," *Applied Physics Letters,* vol. 91, Aug 13 2007.

[18]   M. Steinhart, S. Senz, R. B. Wehrspohn, U. Gosele, and J. H. Wendorff, "Curvature-directed crystallization of poly(vinylidene difluoride) in nanotube walls," *Macromolecules,* vol. 36, pp. 3646-3651, May 2003.

[19]   X. J. He and K. Yao, "Crystallization mechanism and piezoelectric properties of solution-derived ferroelectric poly(vinylidene fluoride) thin films," *Applied Physics Letters,* vol. 89, Sep 2006.

[20]   S. Chen, K. Yao, F. E. H. Tay, and C. L. Liow, "Ferroelectric poly(vinylidene fluoride) thin films on Si substrate with the beta phase promoted by hydrated magnesium nitrate," *Journal of Applied Physics,* vol. 102, Nov 15 2007.

[21]   X. Li, S. Chen, K. Yao, and F. E. H. Tay, "Ferroelectric Poly(vinylidene fluoride) PVDF Films Derived from the Solutions with Retainable Water and Controlled Water Loss," *Journal of Polymer Science Part B-Polymer Physics,* vol. 47, pp. 2410-2418, Dec 1 2009.

[22]   C. Burda, X. B. Chen, R. Narayanan, and M. A. El-Sayed, "Chemistry and properties of nanocrystals of different shapes," *Chemical Reviews,* vol. 105, pp. 1025-1102, Apr 2005.

[23]   G. Xiong, J. W. Elam, H. Feng, C. Y. Han, H. H. Wang, L. E. Iton, L. A. Curtiss, M. J. Pellin, M. Kung, H. Kung, and P. C. Stair, "Effect of atomic layer deposition coatings on the surface structure of anodic aluminum oxide membranes," *Journal of Physical Chemistry B,* vol. 109, pp. 14059-14063,

Jul 2005.

[24] L. Liu, S. H. Yoo, S. A. Lee, and S. Park, "Wet-Chemical Synthesis of Palladium Nanosprings," *Nano Lett,* vol. 11, pp. 3979-3982, Sep 2011.

[25] K. Yao and F. E. H. Tay, "Measurement of longitudinal piezoelectric coefficient of thin films by a laser-scanning vibrometer," *Ieee Transactions on Ultrasonics Ferroelectrics and Frequency Control,* vol. 50, pp. 113-116, Feb 2003.

Chapter 7   Conclusions

The main objectives of this work are to develop the scalable methods for producing ferroelectric PVDF-based thin films and nanostructures at low cost, and study their potential applications in energy storage and energy harvesting. This chapter presents a summary of the results and discussions in this thesis.

In the first part of this work, a novel one-end sealed, open end linked P(VDF-TrFE) nanotube array with double side silver coatings was designed and fabricated through solution approach using AAM template. The P(VDF-TrFE) nanotubes were about 250 nm in outer diameter, 50 nm in wall thickness with about 40 nm-thick silver layers on both sides. Compared with P(VDF-TrFE) film with similar overall thickness of 2 μm, the layer of the nanotube array has 33 times larger surface area and 763 times larger capacitance according to the theoretical calculations, and experimentally a 95 times larger capacitance has been demonstrated. Furthermore, the piezoelectric response of P(VDF-TrFE) nanotube array with the top-bottom electrode configuration was investigated. Theoretical simulations show that under a constant applied force, the flexible hollow nanotubes have higher energy harvesting capacity compared to nanorods of similar dimensions. Experimentally, a C-AFM tip is used to provide periodic mechanical deformation and also to measure the generated current. A systematic study is undertaken to investigate how poling influences the current output. Piezoelectric current as large as about 150 pA has been

experimentally demonstrated in vertically poled P(VDF-TrFE) nanotube array. These results indicate that the polymer nanotube array with the double side electrode coatings may have great potential in realizing high energy density capacitor and high power dielectric energy storage, and the flexible hollow nanotube array with the top-bottom electrode configuration is a very promising candidate for mechanical energy harvesting applications.

Compared to the copolymer P(VDF/TrFE), PVDF homopolymer possesses many advantages including larger intrinsic polarization, higher Curie temperature, higher breakdown strength, significantly lower cost and ready availability. However, it is challenging to obtain the highly polar β phase since the non-polar α phase is thermodynamically favored. In this study, we have achieved ferroelectric β-phase in PVDF homopolymer thin films and nanostructures using various approaches. β-phase PVDF homopolymer thin films have been obtained by introduction of dedicatedly selected hydrated salt as well as LB deposition process, and β-phase PVDF homopolymer nanotube array has also been fabricated in AAM template by solution deposition. The mechanism of β phase formation was shown to be due to hydrogen bonds between the polar hydroxyl groups and PVDF polymer chain.

To avoid larger leakage current and dielectric loss caused by water in the PVDF homopolymer film with β phase promoted by the added hydrated salt during crystallization, an important prerequisite is that the hydrated salt must have a

dehydration temperature higher than the crystallization temperature of the PVDF films but decompose in the following annealing process. The hydrated salt $Al(NO_3)_3 \cdot 9H_2O$ well meets the above requirements. With $Al(NO_3)_3 \cdot 9H_2O$ of appropriate amount introduced to the precursor solution, the resulting β-phase dominant ferroelectric PVDF thin films exhibited smooth morphology, low dielectric loss, high remnant polarization of 89.1 mC/m^2, and large effective piezoelectric coefficient d_{33} of -14.5 pm/V (under the clamping of the substrate). In the LB deposited PVDF ultra-thin films, the hydrogen bonds formed between the PVDF molecules and water led to direct formation of ferroelectric β phase in PVDF homopolymer ultra-thin films. PFM measurements confirmed that the PVDF molecular chains were parallel to the substrates and the dipoles were aligned perpendicular to the substrates, which is consistent with the analyzed interaction mechanism through hydrogen bond. For the solution-derived PVDF nanotube array fabricated in AAM template, the hydrogen bonds between hydroxyl groups at AAM surface and PVDF molecules at the interface of PVDF solution and AAM surface induced the formation of β phase. The PVDF nanotube array showed a high remnant polarization of 82.4 mC/m^2, and large effective piezoelectric coefficient d_{33} of -19.2 pm/V (under the clamping of the substrate), which was substantially larger than 1-μm-thick β-phase PVDF film on substrate.

In consideration of the very low cost and readily commercial availability of PVDF homopolymer and AAM template, the above mentioned chemical solution

deposition of β-phase PVDF thin films and template-based fabrication of ferroelectric PVDF nanotubes are realistic approaches to produce scalable, large area ferroelectric and piezoelectric polymeric devices.

Chapter 8   Recommendations for future work

As discussed in the previous chapters, P(VDF-TrFE) nanotube array has been successfully fabricated. Electroless-plated Ag layers were deposited on both inner and outer sides of the nanotubes as electrodes, which greatly enlarged the contact area between the electrodes and the polymer dielectric to achieve the enhanced capacitance. However, the experimentally obtained capacitance is much smaller than the theoretically calculated value, probably due to the aggregation of silver inside the nanotubes and thus imperfect conductive electrode coverage over the inner surface of the polymer nanotubes. Hence, modification on the deposition of inner silver layer might significantly improve the capacitance of the P(VDF-TrFE) nanotube structure.

Piezoelectric current has been experimentally demonstrated in P(VDF-TrFE) nanotube array with a conducting AFM tip; however the tip can deform only a very small area of the array. Hence, future work could also be directed to the fabrication and characterizations of large area energy harvesting devices based on piezoelectric PVDF and P(VDF-TrFE) nanotube arrays, and demonstrating their operation and potential value in practical device applications.

Appendix

List of Publications

Journal Papers

- **Li, X.;** Chen, S.T; Yao, K.; Tay, F. E. H. Ferroelectric Poly(vinylidene fluoride) PVDF Films Derived from the Solutions with Retainable Water and Controlled Water Loss. J. Polym. Sci. Pt. B-Polym. Phys. 2009, 47, (23), 2410-2418.

- Chen, S. T.; **Li, X**.; Yao, K.; Tay, F. E. H.; Kumar, A.; Zeng, K. Y. Self-polarized ferroelectric PVDF homopolymer ultra-thin films derived from Langmuir-Blodgett deposition. Polymer 2012, 53, (6), 1404-1408.

- **Li, X.;** Lim, Y.F; Yao, K.; Tay, F. E. H; Seah, K. H. Fabrication and characterization of P(VDF-TrFE) nanotube array with double side electroless plated silver layers. Phys. Chem. Chem. Phys., 2013, 15, 515

- **Li, X.;** Lim, Y.F; Yao, K.; Tay, F. E. H; Seah, K. H. Solution derived ferroelectric PVDF homopolymer nanotubes in anodic alumina membrane (AAM) template. Chem. Mater, 2013, 25 (4), 524–529

Conference Presentations

- Tay, F. E. H., Chen, S., **Li, X.**, Yao, K., Polymeric Piezoelectric Materials and Devices Applications, *CANEUS Workshops.* March 2009. California, USA. [Oral presentation].

- **Li, X.;** Chen, S.T; Yao, K.; Tay, F. E. H. Preparation of ferroelectric poly(vinylidene fluoride) homopolymer films by manipulating water loss. *Joint meeting of 12th International Meeting on Ferroelectricity and 18th IEEE International Symposium on Applications (IMF-IASF 2009).* August, 2009. Xi'an China. [Poster presentation].

- **Li, X.;** Chen, S.T; Yao, K.; Tay, F. E. H. Ferroelectric poly(vinylidene fluoride) PVDF thin films derived from the solutions with retainable water and controlled water loss. *Annual International Conference on Materials Science, Metal & Manufacturing (M3 2011).* Jan, 2011. Singapore [Poster presentation].